Jagiellonian University in Kraków
Faculty of Physics, Astronomy and Applied Computer Science
Marian Smoluchowski Institute of Physics

PHD IN THE FIELD OF SCIENCE OF PHYSICS

DOCTORAL DISSERTATION

Open charm measurements at the NA61/SHINE experiment at CERN SPS with the new Vertex Detector

Anastasia Merzlaya

Supervisor:
dr hab. Paweł Piotr Staszel, prof. UJ
Department of Hot Matter Physics, FAIS UJ

Kraków, 25.02.2021

Wydział Fizyki, Astronomii i Informatyki Stosowanej,
Uniwersytet Jagielloński

Oświadczenie

Ja niżej podpisana Anastasia Merzlaya (numer albumu: 1137941), doktorantka Wydziału Fizyki, Astronomii i Informatyki Stosowanej Uniwersytetu Jagiellońskiego oświadczam, że przedłożona przeze mnie rozprawa doktorska pt. *Open charm measurements at the NA61/SHINE experiment at CERN SPS with the new Vertex Detector* jest oryginalna i przedstawia wyniki badań wykonanych przeze mnie osobiście, pod kierunkiem dr. hab. Pawła Piotra Staszla. Pracę napisałam samodzielnie. Oświadczam, że moja rozprawa doktorska została opracowana zgodnie z Ustawą o prawie autorskim i prawach pokrewnych z dnia 4 lutego 1994 r. (Dziennik Ustaw 1994 nr 24 poz. 83 wraz z późniejszymi zmianami). Jestem świadoma, że niezgodność niniejszego oświadczenia z prawdą ujawnioną w dowolnym czasie, niezależnie od innych skutków prawnych wynikających z ww. ustawy, może spowodować unieważnienie stopnia nabytego na podstawie tej rozprawy.

Kraków, 25.02.2021 Anastasia Merzlaya

Abstract

The study of open charm meson production provides an efficient tool for detailed investigations of the properties of hot and dense matter formed in relativistic nucleus-nucleus collisions. In particular, charm mesons are of vivid interest in the context of the phase-transition between confined hadronic matter and the quark-gluon plasma as well as for interpretation of data on J/ψ production measured by the NA38/NA50 and NA60 experiments. Also, such study gives a unique opportunity to test the validity of theoretical models based on perturbative Quantum Chromodynamics and Statistical model approaches for nucleus collisions at the top SPS energy. Such models provide predictions for charm yields, that differ by up to two orders of magnitude.

Direct measurements of open charm mesons are challenging since the yields of D mesons are very low and their lifetimes are short, which means that such measurements require precise determination of particle tracks and high primary and secondary vertex resolution. To meet these challenges a new high resolution Small Acceptance Vertex Detector (SAVD) based on silicon pixel sensors MIMOSA-26AHR was constructed and installed in the NA61/SHINE experiment which was motivated by the importance and the possibility of the first direct measurements of open charm mesons in heavy ion collisions at SPS energies.

The SAVD was installed in 2016 to perform a test for Pb+Pb reactions with the beam momentum of 150A GeV/c. Later, in 2017 and 2018 large statistic data sets have been taken for Xe+La and Pb+Pb collisions at 150A GeV/c.

Within this PhD project reconstruction and analysis of the collected data of Xe+La and Pb+Pb collisions in the NA61/SHINE experiment were performed in order to determine the yield of $D^0+\overline{D^0}$. The obtained $D^0+\overline{D^0}$ signal was the first, direct observation of open charm in nucleus-nucleus collisions at the SPS energies. These results were compared to the theoretical model predictions as well as the estimation made by the NA50/NA60 experiments.

Furthermore, the NA61/SHINE experiment plans a systematic measurements of open charm production in Pb+Pb collisions in the period 2021-2024 after the major detector upgrade conducted during the Long Shutdown 2. The performed simulation study of the upgraded Vertex Detector showed, that these future data will allow for the more detailed research of charm particles.

Streszczenie

Badanie produkcji mezonów powabnych dostarcza skutecznego narzędzia do szczegółowych badań właściwości gorącej i gęstej materii powstałej w relatywistycznych zderzeniach jądro-jądro. W szczególności mezony powabne są bardzo interesujące w kontekście przejścia fazowego między materią hadronową a plazmą kwarkowo-gluonową, a także w interpretacji danych dotyczących produkcji J/ψ zmierzonych przez eksperymenty NA38/NA50 i NA60. Pomiary produkcji mezonów powabnych w zderzeniach jąder przy energiach osiąganych na akceleratorze SPS dają również wyjątkową okazję do testowania modeli teoretycznych zarówno tych opartych na podejściu w ramach perturbacyjnej chromodynamiki kwantowej jak i tych opartych podejściu statystycznym. Przewidywania takich modeli dotyczące krotności produkcji mezonów powabnych różnią się nawet o dwa rzędy wielkości.

Bezpośrednie pomiary mezonów niosących powab stanowią wyzwanie, ponieważ krotności tych mezonów są bardzo niskie, a ich czasy życia są krótkie, co oznacza, że takie pomiary wymagają precyzyjnego określenia śladów cząstek oraz określenia punków których nastąpiło pierwotne oddziaływanie jądro-jądro oraz wtórny rozpad mezonów (wtórny wierzchołek).

Aby sprostać tym wyzwaniom, w eksperymencie NA61/SHINE zainstalowano pilotażową wersję detektora wierzchołka o nazwie Small Acceptance Vertex Detector (SAVD). SAVD oparty jest na krzemowych sensorach pikselowych MIMOSA-26AHR.

SAVD został zainstalowany w 2016 roku w celu przeprowadzenia jego testów dla reakcji Pb+Pb z pędem wiązki 150A GeV/c. Później, w 2017 i 2018 roku SAVD został wykorzystany do regularnych pomiarów dla zderzeń Xe+La i Pb+Pb przy 150A GeV/c.

W ramach niniejszej pracy doktorskiej przeprowadzono rekonstrukcję i analizę danych zebranych dla zderzeniach Xe+La i Pb+Pb w eksperymencie NA61/SHINE w celu określenia wydajności $D^0 + \overline{D^0}$. Uzyskany sygnał $D^0 + \overline{D^0}$ jest pierwszą bezpośrednią obserwacją mezonów powabnych w zderzeniach jądro-jądro przy energiach SPS. Uzyskane wyniki porównano z przewidywaniami modeli teoretycznych, a także szacowaniem produkcji mezonów D^0 dokonanym w ramach eksperymentów NA50/NA60.

Eksperyment NA61/SHINE planuje systematyczne pomiary produkcji mezonów powabnych w zderzeniach Pb+Pb w latach 2021-2024 po poważnej modernizacji detektora wierzchołka przeprowadzonej podczas tzw. *Long Shutdown 2* w ośrodku CERN. Symulacje komputerowe działania zmodernizowanego detektora wierzchołka pokazały, że te przyszłe pomiary pozwolą na bardziej systematyczne i szczegółowe badania produkcji cząstek powabnych w relatywistycznych zderzeniach jądro-jądro.

Acknowledgements

I would like to express my gratitude to my supervisor Pawel Staszel for his guidance and support through my PhD study. His experience and knowledge made not only this thesis but the whole SAVD project possible.

I would like to thank Dag Larsen who introduced me to the SAVD project and was a great help not only on my first steps towards the SAVD reconstruction and simulation but also in further stages of work with assistance and valuable remarks.

I am very appreciative to Roman Planeta for giving me an opportunity to work within the Department of Hot Matter Physics in Jagellonian University.

I am thankful to Marek Gazdzicki and Peter Seyboth for the opportunity to participate in the NA61/SHINE Collaboration. Also, my path through the thesis benefited a lot from fruitful meetings with Tatjana Susa, Grigory Feofilov, Wojciech Brylinski and the V0/D0 group, Grzegorz Stefanek, Bartosz Maksiak and the Calibration/Reconstruction group, Yoshikazu Nagai and the Software group.

I also would like to thank my family and friends for support during my study.

The work was partially supported by the Polish National Center for Science Grants 2018/29/N/ST2/02595 and 2015/18/M/ST2/00125.

for my loved one

Contents

Chapter 1

Introduction

1.1 Heavy-ion physics

1.1.1 Standard Model and quantum chromodynamics

The discovery of electron in the end of 19th century led to the conclusion that atoms are not elementary particles. Later, in the beginning of 20th century it was established that atom nuclei is made of neutrons and protons. Throughout 20th century more and more particles have been experimentally discovered as well as understanding of the fundamental laws has been expanded. Nowadays it is well established fact that the matter is mostly built of electrons, neutrons and protons, and that last two are made of quaks and gluons.

To describe elementary particles and interactions between them the Standard Model [1] is used. The Standard Model is a quantum field theory. Many of its predictions were confirmed experimentally. However this theory is not complete – for example it doesn't include the gravitational interaction.

At this moment 12 elementary fermions (with their corresponding antiparticles) are known and by the way they interact they could be separated to six quarks and six leptons. The interaction between fermions are carried out by bosons: gluons for strong interaction, photons for electromagnetic, W^+, W^- and Z^0 for weak interaction. The Higgs boson is carrier of the interaction of the Higgs field which grants the particle their masses. The Standard Model encloses these particles and interactions. Schematic summary is shown in Fig. 1.1.

The important part of the Standard Model is the Quantum Chromodynamics (QCD), which describes the strong interaction. According to the QCD quarks and gluons have additional state of freedom called color charge. There are three colors and three anti-color, and each quark has one color (or anti-color) and each boson has pair of pair color and anti-color, and only neutral-color particles can be observed.

There are two important features of the QCD. The first one is called the color confinment and concerns the fact that quarks and gluons cannot be directly observed due to their color charge and are always bound within hadrons. The second one is called asymptotic freedom. The strong interaction is weak at short distances and significantly increases with the distance. Thus, if distances between quarks become extremely small they start to interact like quasi-free particles.

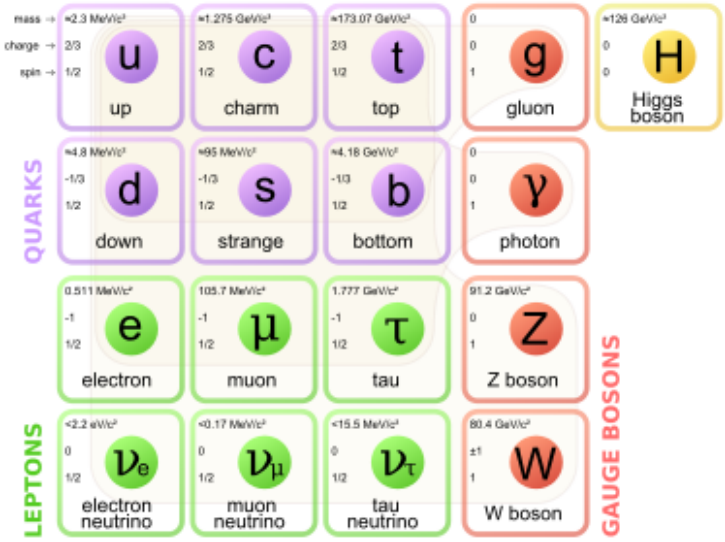

Figure 1.1: Table of the elementary particles described by the Standard Model. Violet squares presents the quarks, green – the lepton, red – the bosons, yellow – the Higgs boson [2, 3]

1.1.2 High energy collisions and quark-gluon plasma

Quark-gluon plasma (QGP) is a state of matter in which quarks and gluons are not confined in the hadrons. It is believed that the Universe was in the QGP state few milliseconds after the Big Bang. Later, the expanding Universe was cooling down and quarks and gluons became bound together to form hadrons.

To recreate conditions similar to those of the early Universe, powerful accelerators deliver head-on collisions of heavy ions. It is expected that QGP can be created in hot and dense systems produced in such collision.

Evolution of high energy nuclear collision

Fig. 1.2 shows two possible scenarios of space-time evolution of heavy-ion systems: the left side of the figure presents a scenario where the temperature and energy density are not sufficiently high to create the QGP state, the right side presents a scenario in which the QGP is created.

During a central collision of two heavy ions accelerated to velocities close to the speed of light, the initial energy of colliding nuclei dissipates and a new hot and dense system called fireball is formed. The formation time is estimated to be about 1 fm/c and is related to the time in which Lorentz contracted ions penetrate each other. After that, due to high number of interactions the system is thermalized and QGP is created. As it expands and cools down, quarks and gluons start to merge and form hadrons. This process is called hadronization and occurs approximately few fm/c after the creation of QGP. During hadronization the QGP state converts into the hadron gas state, which means that there are no quarks moving freely and all of them are confined in hadrons. The moment when the chemical composition of the system becomes fixed and hardons stop exchanging quarks between each other is called the chemical freeze-out. The system continues to expand and cool down while produced particles interact with each other and exchange their momenta. The instant when this process stops and momenta of the particles gets fixed is called kinetic freeze-out. These produced particles and/or products of their decays can be detected by the experimental apparatus.

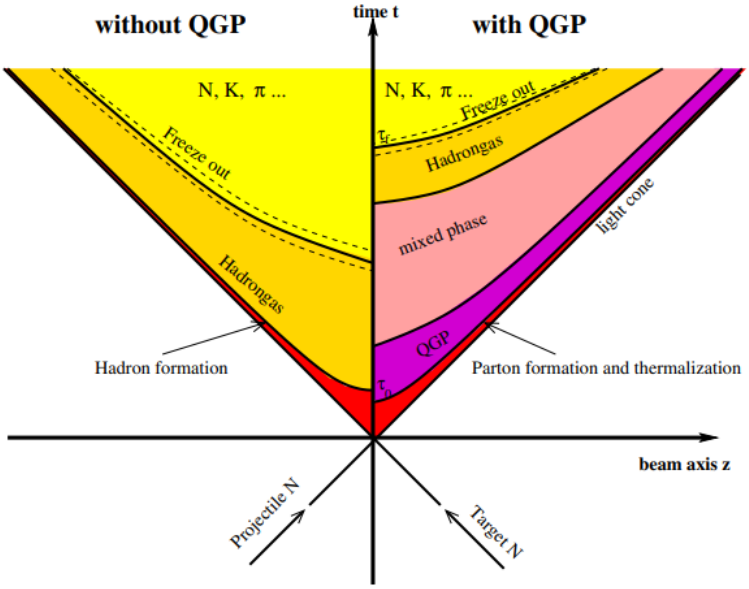

Figure 1.2: Space-time evolution of heavy-ion collision [4]

Phase diagram of strongly interacting matter

Hadron gas and QGP are the main phases of strongly interacting matter. Transition between these states can be obtained by changing the temperature T and baryon chemical potential μ_B (the energy needed to add or remove one baryon from the system) of strongly interacting matter.

The phase diagram is usually presented in T-μ_B plane. It is shown on Fig. 1.3. At low temperatures and relatively low baryon chemical potential the main phase of matter is the hadron gas state. With higher temperatures the system is in the QGP state. The matter with low temperatures and high baryon chemical potential exists in neutron stars.

Two types of the phase transition are predicted: for low baryon chemical potential with increasing temperature the phase is changing via crossover (rapid but continuous evolution of the system's physical parameters), while with higher values of baryon chemical potential the first order phase transition is predicted [5]. The line describing the first order phase transition ends with the critical point related to the second order phase transition [6].

Different regions of the phase diagram of strongly interacting matter can be probed experimentally by varying the size of the colliding nuclei, centrality of the collision and the collision energy [7].

Charm production as QGP signature

Conditions of the produced in the collision matter such as extreme temperature or short lifetime make a direct observation of the QGP state not possible. However QGP can be studies via analysis of properties of the particles that passed hadronization process. Thus, many observables have been developed (called QGP signatures) based on information delivered by particles produced in final state of interaction. These observables are expected to be sensitive to creation of QGP.

One of such QGP signatures is suppression of the J/ψ mesons production. Another one is the enhancement of the total charm production. This will be discussed in details in Chapter 2.

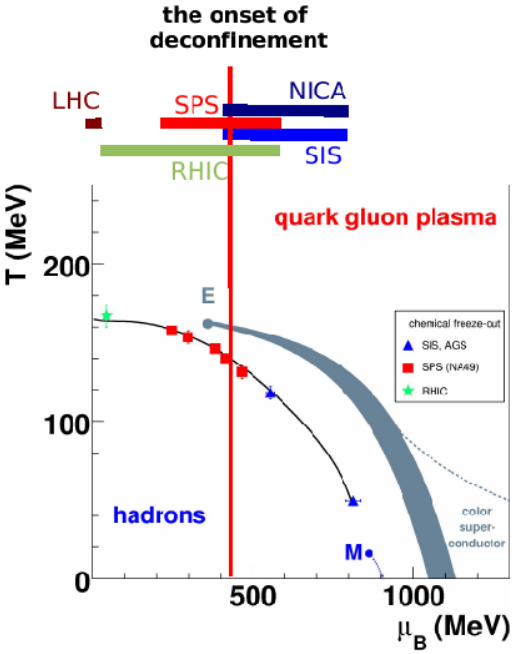

Figure 1.3: Phase diagram of strongly interacting matter. Points with error bars indicate the positions of chemical freeze-out of the systems collided with energies delivered by – RHIC (Relativistic Heavy Ion Collider), SPS (Super Proton Synchrotron), AGS (Alternating Gradient Synchrotron), SIS (Schwerionen-Synchrotron) accelerators. Grey band corresponds to the predicted first order phase transition ending with the critical point. The vertical dashed line indicates expected barionic chemical potential of the onset of deconfinement. On the top of the plot energy regions of experimental facilities indicated: Large Hadron Collider (LHC), RHIC, SPS, Nuclotron-based Ion Collider fAcility, SIS [8].

Open charm meson	Decay channel	$c\tau$ [μs]	Branching ratio
D^0	$\pi^+ + K^-$	122.9	$(3.89 \pm 0.04)\%$
$\overline{D^0}$	$\pi^- + K^+$	122.9	$(3.89 \pm 0.04)\%$
D^+	$\pi^+ + \pi^+ + K^-$	311.8	$(8.22 \pm 0.28)\%$
D^-	$\pi^- + \pi^- + K^+$	311.8	$(8.22 \pm 0.28)\%$

Table 1.1: Information about the most probable decay channels of open charm mesons.

1.2 Goal and structure of thesis

The main goal of the study presented in this thesis is to analyse the data collected by the NA61/SHINE experiment in order to obtain the first direct observation of the open charm in heavy-ion collisions (Xe+La and Pb+Pb) at the CERN SPS energy regime and estimate the $D^0 + \overline{D^0}$ yields. These results are compared to predictions of theoretical models as well as to the estimations made by the NA50/NA60 experiments.

Table 1.2 shows decay channels of the open charm mesons, that are considered in NA61/SHINE for measurements. In a present study only D^0 and $\overline{D^0}$ were considered.

The thesis consists of 9 chapters. After theoretical introduction to heavy-ion collisions in Chapter 1 the motivation and importance of open charm measurements is discussed in details in Chapter 2. Chapter 3 describes the NA61/SHINE experiment at CERN SPS and the new Small Acceptance Vertex Detector (SAVD) with the help of which open charm measurements became possible in NA61/SHINE. In Chapter 4 data reconstruction techniques in the native NA61/SHINE detectors are briefly presented, and reconstruction procedure in SAVD as well as track and vertex reconstruction results in SAVD are discussed in details. Data calibration performed for the Time Projection Chambers and SAVD is described in Chapter 5.

In Chapter 6 the used data sets and selection of the analysed events are presented. Analysis procedure and results are discussed in Chapter 7. Chapter 8 is focused on

the description of the dedicated computer simulations. Finally, in Chapter 9 the results are summarised and future plans for open charm measurements in the NA61/SHINE experiment are discussed. Chapter 10 concludes the thesis.

1.3 Author's contribution

The author has been a member of the NA61/SHINE Collaboration since Master studies (2014-2016) and has been actively working on the Vertex Detector project. Since the beginning of the PhD studies (2016) the author was actively participating in the data taking campaigns and, in particular, supervising the Small Acceptance Vertex Detector operation during data taking in 2016 (test data taking), 2017 and 2018. Further, the author passed through all stages preceding analysis and interpretation of the data: starting from preliminary performance simulations, developing the reconstruction chain, calibration of the collected data, selection of the events, performing full simulation chain for efficiency calculation and analysis correction. The author made major contribution to implementation of SAVD events reconstruction in the Shine framework. Also, the author provided implementation of GEANT4 simulation and reconstruction chain in the Shine framework. The simulation performed by author were used to determine acceptance and reconstruction efficiencies of the NA61/SHINE experimental setup including the SAVD device. The obtained information was used to correct the rough experimental yields and obtained results on the D meson production presented in this thesis. The simulations were also used to determine the geometrical layout and expected yields for the upgraded version of the Vertex Detector to be used after the Long Shutdown 2.

Finally, the author performed analysis of the reconstructed data as well as simulated data according to two models (PHSD and AMPT) in order to obtain results presented in this thesis. These results were compared to theoretical models as well as the estimations made by the NA50/NA60 experiments.

Chapter 2

Open charm measurements motivation

2.1 Model predictions of charm yield

One of the important issues related to relativistic heavy-ion collisions is the mechanism of charm production. Several model predictions was introduced to describe charm production. Some of them based on the dynamical approach and some - on the statistical approach.

The dynamical approach is inspired by the perturbative QCD (pQCD) and describes charm particle production in elementary hadronic and nuclear collisions [9]. According to this approach, pre-charmonium states are created due to the binding interaction between $c\bar{c}$ quarks. In nucleon-nucleus (p+A) and nucleus-nucleus (A+A) reactions this pre-charmonium state encounters interactions with the surrounding matter [10]. Further, that produced charm states form bound states of closed charm particles (J/ψ and excited charmonium states) as well as open charm particles which are produced from the binding interaction between charm quark and the lighter quark (d,u and s).

The statistical approach used for describing the production of open and hidden charm is based on thermodynamical treatment of the initial stage in which partons are considered as primary degrees of freedom. In 1997 it was observed, that the J/ψ yield in A+A collisions is proportional to the pion multiplicity, and that the experimental results of J/ψ yield may be explained by a statistical production at the hadronisation stage [11]. This motivated the development of statistical approaches for open and closed charm production. In such approaches one assumes that c and $\bar{c}$ quarks are generated at the early stage of the collisions according to the collision volume and available energy. The globally equilibrated state created in the early stage expands and finally freezes–out into hadrons and hadronic resonances.

The estimates from dynamical and statistical approaches for charm yield for central Pb+Pb collisions at 158A GeV/c differ by about two orders of magnitude [11, 12]. Fig. 2.1 presents the predictions on $\langle c\bar{c}\rangle$ production provided by different models:

- A pQCD-inspired models [13, 14] - predictions based on PYTHIA [15] calculations for nucleon-nucleon collisions scaled to central Pb+Pb collisions using the nuclear thickness function;

- The Hadron String Dynamics (HSD) model [16] - uses parametrization of the charm mesons and hadrons cross sections based on the word wide data for p+N and π-

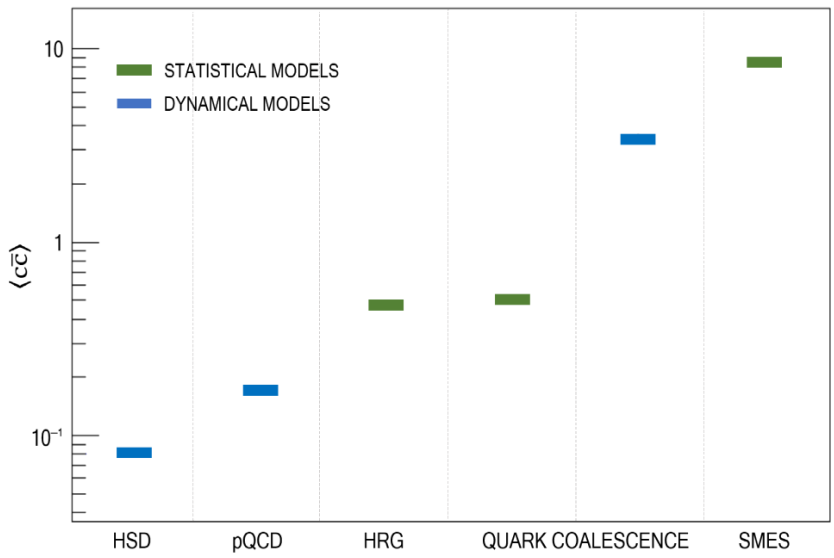

Figure 2.1: Mean multiplicity of charm quark pairs produced in the full phase space in central Pb+Pb collisions at 158A GeV/c calculated with dynamical models (blue bars): HSD, pQCD–inspired and Dynamical Quark Coalescence, and statistical models (green bars): HRG, Statistical Quark Coalescence and SMES [12].

N reactions. To describe charm production in A-A collisions the parametrised $c\bar{c}$ yields are scaled with the number of hard binary collisions. In addition to primary hard N-N collisions, the open charm mesons or charmonia may also be generated by secondary meson-baryon interactions.

- The Dynamical Quark Coalescence model [17] - the mean number of $\langle c\bar{c} \rangle$ pairs is calculated using the measured $\langle J/\psi \rangle$ multiplicity [18] and the probability of a single $c\bar{c}$ pair hadronizing into a J/ψ calculated within the model that assumes a microscopic hadronization mechanism of deconfined matter;

- The Statistical Quark Coalescence model [19] - the mean number of $\langle c\bar{c} \rangle$ pairs is calculated using the measured $\langle J/\psi \rangle$ multiplicity [18] and the probability of a single $c\bar{c}$ pair hadronizing into a J/ψ calculated within the model that assumes a statistical distribution of c and $\bar{c}$ quarks between hadrons;

- The Hadron Resonance Gas model (HRG) [19] - a calculation of equilibrium yields of charm hadrons assuming parameters of a hadron resonance gas fitted to mean multiplicities of light hadrons;

- The Statistical Model of the Early Stage (SMES) [20] - the mean number of charm quarks is calculated assuming an equilibrium QGP at the early stage of the collision and using the grand canonical ensemble for predictions. Mostly due to the significantly higher temperature at the early stage of the collision then at the hadronization stage the charm yield predictions are higher in SMES then in HRG.

The predictions on mean multiplicity of charm quark pairs $\langle c\bar{c} \rangle$ suffer from large systematic uncertainties. In the statistical models this is mostly due to uncertainties of the system temperature and volume, whereas in dynamical approaches - due to uncertanties in modelling charm production in nucleon-nucleon interactions.

Also, these approaches predict different dependencies on the system size. In the dynamical models the open charm yield is proportional to the number of nucleon-nucleon collisionsThe SMES model uses the grand canonical ensemble volume dependence of the yield, which means that the predicted yield is proportional to the number of wounded nucleons N_W (taking into account that for a large enough number of participant nucleons ($\langle N_P \rangle > 50$) the calculated charm yields are larger then one) [9]. For collisions of identical nuclei the ratio of number of nucleon-nucleon collisions to the number of wounded nucleons changes as $N_W^{1/3}$ and thus increases by factor of about 6 between nucleon-nucleon and central Pb+Pb collisions.

Therefore, obtaining precise data on $\langle c\bar{c} \rangle$ will allow to disentangle between theoretical predictions and learn about the charm quark and hadron production mechanism. In particular such study should allow to establish a border between the applicability of pQCD-based and statistical models.

Fig. 2.2 presents how the charm quarks are distributed over the most abundant charm carriers according to Parton Hadron String Dynamics model (PHSD) calculations [21]. Thus, a good estimate of $\langle c\bar{c} \rangle$ can be obtained by measurements of D^0, D^+ and their antiparticles because these mesons carry about 85% of the total produced charm as indicated in Fig. 2.2. However, even measurements of D^0 and $\overline{D^0}$ mesons should already provide reasonable estimation as they contain the largest fraction of charm (31% each).

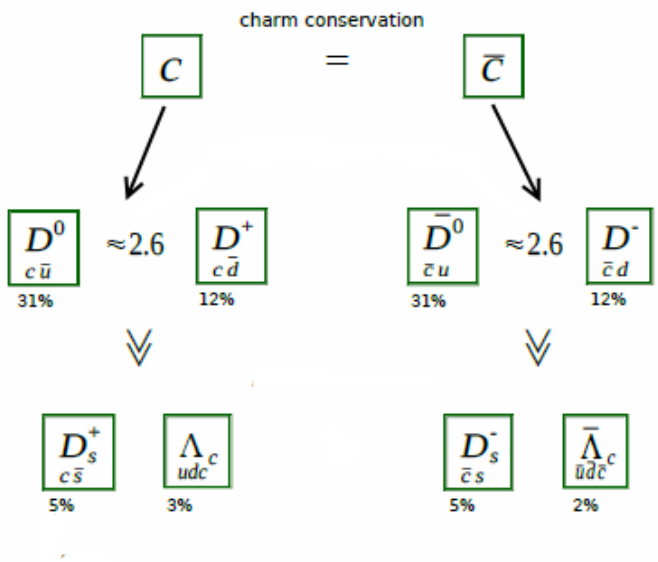

Figure 2.2: Schema of the total charm distribution over most abundant charm hadrons in 0–20% central Pb+Pb collisions at beam energy $150A$ GeV/c (the value is predicted by PHSD). The percentages of fraction of charm carried by given hadron species are indicated.

2.2 Charm measurements for phase transition study

The study of open charm meson production is a sensitive tool for detailed investigations of the properties of hot and dense matter formed in nucleus-nucleus collisions at ultra-relativistic energies [10, 22, 23]. In particular, charm mesons are of vivid interest in the

context of the phase-transition between confined hadronic matter and the QGP.

The $c\bar{c}$ pairs produced in the collisions are converted into open charm mesons and charmonia (J/ψ mesons and its excited states). The production of charm is expected to be different in confined and deconfined matter, which is caused by different properties of charm carriers in these phases. In confined matter the lightest charm carriers are D^0 and $\overline{D^0}$ mesons, whereas in deconfined matter the charm carriers are charm and anti-charm quarks. Thus, in case of confined matter production of a pair of charm carries $D\overline{D}$ requires energy of $2m_D = 3.7$ GeV, which is about 1 GeV higher than production of a $c\bar{c}$ pair which takes energy of $2m_c = 2.6$ GeV. The effective number of degrees of freedom of charm hadrons and charm quarks is similar [24]. Thus, more abundant charm production is expected in deconfined than in confined matter.

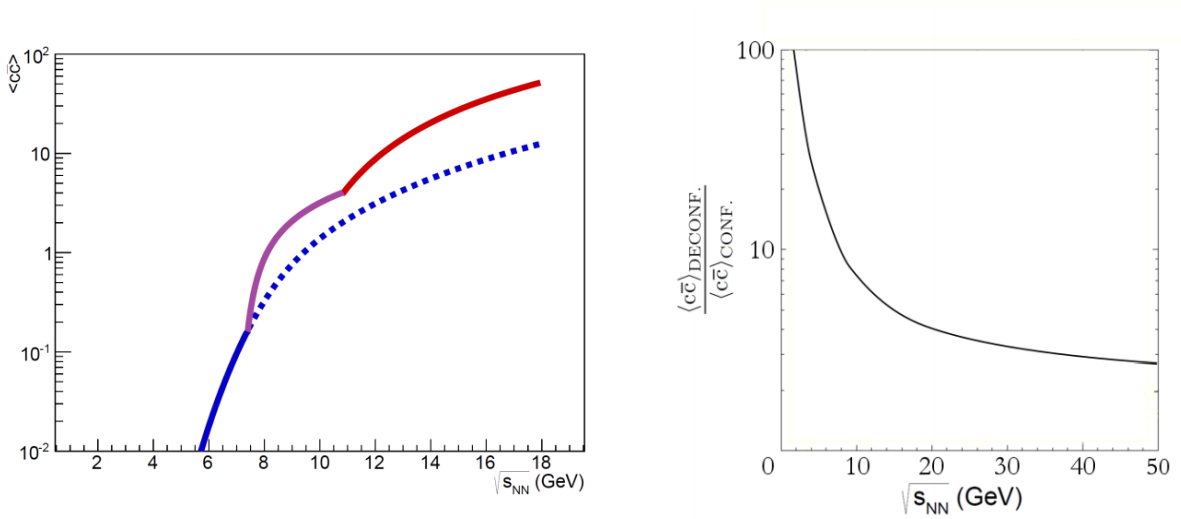

Figure 2.3: Left pad: Energy dependence of $\langle c\bar{c}\rangle$ in central Pb+Pb collisions calculated within the SMES model [20, 12]. The blue line corresponds to confined, the purple line to mixed phase, and the red line to deconfined matter, the dashed line presents the prediction without a phase transition. Right pad: Energy dependence of the ratio of $\langle c\bar{c}\rangle$ in deconfined and confined matter in central Pb+Pb collisions calculated within the pQCD-inspired model [19, 12]

Both dynamical and statistical approaches for charm production predict a rapid change of collision energy dependence when crossing the energy of the onset of deconfinement. Fig. 2.3 presents the collision energy dependence of charm production in central Pb+Pb collisions at 150A GeV/c predicted by SMES model (left pad) and a pQCD-inspired model (right pad). According to SMES model, when crossing the phase transition energy range ($\sqrt{s_{NN}}$ = 7 - 11 GeV), an enhancement of $\langle c\bar{c}\rangle$ production as compare to confined state should be observed. At the beam energy 150A GeV/c ($\sqrt{s_{NN}}$ = 16.7 GeV) an enhancement by a factor of about 4 is expected. Right panel of Fig. 2.3 shows the ratio of mean multiplicity of $c\bar{c}$ pairs in deconfined and confined matter evaluated at the same collision energy calculated within the pQCD-inspired model. At 150A GeV/c ($\sqrt{s_{NN}}$ = 16.7 GeV) an enhancement by a factor of about 3 is predicted. Consequently, according to both theoretical approaches a change of collision energy dependence of $\langle c\bar{c}\rangle$ may be a signal of onset of deconfinement.

Furthermore, the $c\bar{c}$ pairs produced in the collision can be converted to open or hidden

charm. Fig. 2.4 presents two scenarios for such conversions. In the first case (left pad) in p+p interaction produced $c\bar{c}$ pairs hadronize in a vacuum. Open charm and charmonia are produced with a certain probability, which is at high collision energies is typically 10% of $c\bar{c}$ pairs for charmonia formation and 90% for open charm hadrons. In the second case (right pad) for A+A reactions the charmonium production follows the standard scenario [10]: $c\bar{c}$ pairs form a precharmonium state in the QGP, then the produced charmonia encounters further interactions with the surrounding deconfined medium. Due to the color screening, which may lead to disintegration of this state and prevent the binding of charm quarks and anti-quarks to produce charmonia, the probability of charmonium production is suppressed in favour of open charm production. Thus, the charmonium production is reduced in this case and probabilities at high energies are 2% and 98% for close an open charm hadrons formation, respectively. Thus the effect of the medium on charm production can only be determined by studying the ratio between the charmonium and the open charm mesons yield.

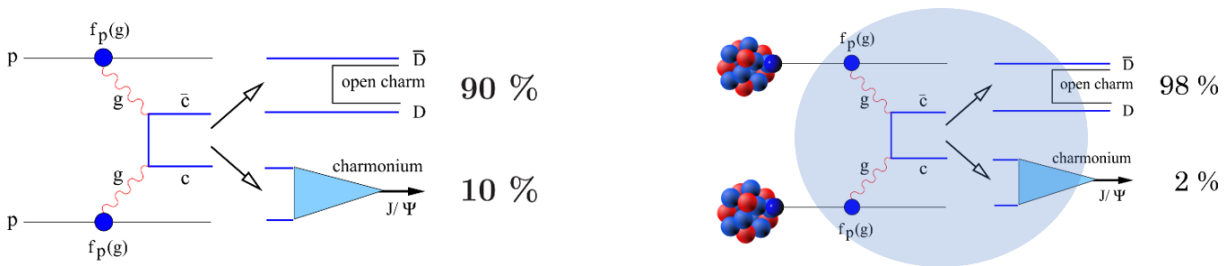

Figure 2.4: Schematic view of J/ψ production in p+p collisions (left pad) and central heavy ion collisions (right pad) [22].

2.3 Previous charm measurements

2.3.1 NA49 open charm measurements

The first attempt to estimate of the upper limit of mean multiplicity of D^0 and $\overline{D^0}$ mesons by a direct measurement was done by the NA49 experiment in Pb+Pb collisions at the top SPS energies [25]. D^0 and $\overline{D^0}$ mesons were searched via their $D^0 \rightarrow \pi^+ + K^-$ and $\overline{D^0} \rightarrow \pi^- + K^+$ decay channels and the invariant mass distribution of identified kaons and pions was studied. However, due to accuracy in reconstruction of the vertex longitudinal position on the level of 1 cm which is significantly larger then the distance between the interaction point and the secondary vertices of D^0 and $\overline{D^0}$, no open charm signal was observed. The upper limit of the yield was estimated to be $M(D^0 + \overline{D^0}) = 1.5$ per event at 98% confidence level in central Pb+Pb collisions at 158A GeV/c [25] (the mixture of two data set was used: 3M events with centrality 0–23.5% and 0.8M events with centrality 0–10%). The obtained upper limit discards only prediction made by the SMES model (see Fig. 2.1).

2.3.2 NA38/NA50 and NA60 charm measurements

The NA38/NA50 and NA60 experiments performed measurements of J/ψ production at top SPS energies [26, 27, 28]. The apparatus of these experiments consists of the muon spectrometer (which they were inheriting after one another), and charm study is based

of dimuon production in heavy-ion collisions at the SPS energies. The dilepton invariant mass spectrum was obtained as wide continuum dominated by the resonance (ρ, ω, ϕ, J/ψ, ϕ') decay peaks. This vector mesons have well pronounced structures in the invariant mass distribution, can be described by cocktail determined from p+p collisions however the analysis of the mass spectrum between ϕ and J/ψ required the dedicated study. The contribution in this region was described in terms of Drell-Yan and $D\overline{D}$ estimated according to the PYTHIA event generator [15] (based on pQCD calculations). However, the spectrum for central Pb+Pb collisions at 158A GeV/c obtained by NA38/NA50 (see Fig. 2.5) could be reproduced when the open charm contribution is scaled up by a factor of about 3 with respect to the pQCD calculations [29], which gives $\langle D^0 + \overline{D^0} \rangle = 0.6$ per event.

Thereby, despite the indirectly obtained indication of open charm this results is strictly model depended and thus very sensitive to kinematics distributions and correlations used in PYTHIA, the results suffer from uncertainties in the estimate of the di-muon spectrum background.

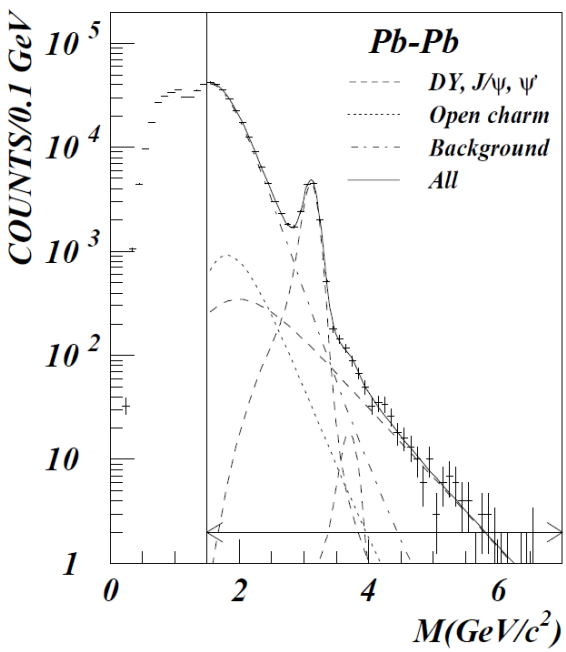

Figure 2.5: The invariant mass spectrum obtained in NA50 for central Pb+Pb collisions at 158A GeV/c. The Drell-Yan, J/ψ and ϕ'contributions are shown as dashed lines, the open charm as a dotted line, the background as a dashed-dotted line [29].

An additional controversy comes from the NA60 experiment. The results of NA60 on prompt and non-prompt muon production in In+In collisions at 158A GeV/c show di-muon enhancement as seen by NA38/NA50 in Pb+Pb collisions [30]. However, it was experimentally shown by NA60, that the enhancement observed in In+In is mostly due of prompt muons and was interpreted in terms of creation of a muon radiation source at early stage of the collision phase which was attributed to QGP [30].

Even though the study of di-muon spectra provides imprecise measurements of open charm it allowed for detailed study of charmonium production. In Fig. 2.6 the production of J/ψ in In+In and Pb+Pb collisions relative to the pQCD predictions (assuming normal nuclear absorption in the medium) is shown as a function of the number of participating nucleons N_{part}. For lower number of participants the yields are consistent with the theoretical estimations. However, at $N_{part} \approx 200$ the result shows significant drop. The observed effect is known as an anomalous J/ψ suppression. This suppression of the

production of J/ψ mesons in central Pb+Pb collisions at 158A GeV/c was an important argument for the CERN announcement of the discovery of a new state of matter [31]. Within the Matsui-Satz model [10] the suppression is attributed to onset of QGP formation in nuclear collisions. However, due to initial state effects in nucleus-nucleus reactions, like shadowing, parton energy loss etc. [32], the overall scaled number of the $\langle c\bar{c}\rangle$ pairs produced in nuclear collisions may be reduced. Hence the effect of the medium on J/ψ survival can only be determined by studying the charmonium yield relative to the yield of open charm mesons [22]. Thus, only precise measurement of both open and hidden charm can provide information on influence of the final state interaction on charmonia yield in a model independent way.

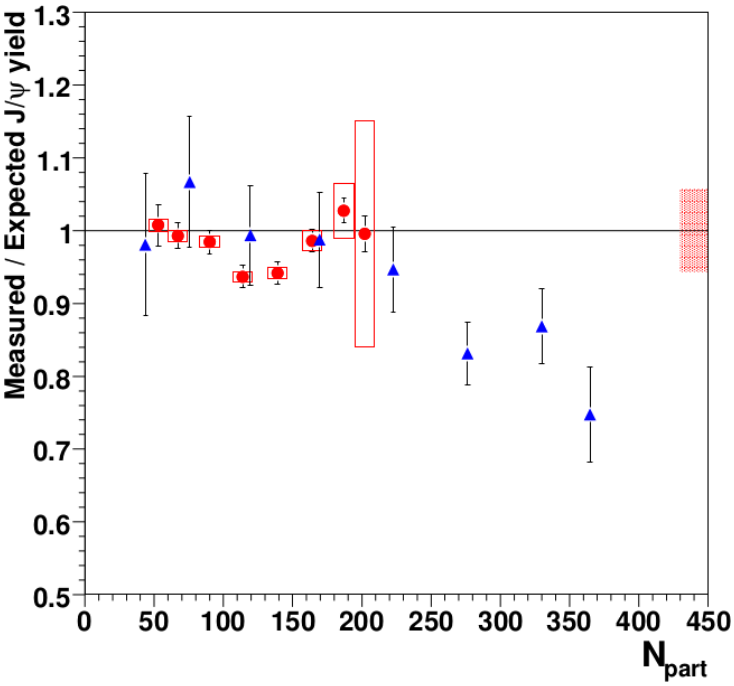

Figure 2.6: J/ψ suppression pattern measured in In+In (circles) and Pb+Pb (triangles) collisions as a function of the number of participants N_{part} at 158A GeV/c. The boxes around the In+In points represent correlated systematic errors. The filled box corresponds to the uncertainty in the absolute normalization of the In+In points. [33].

Therefore for the interpretation of existing results on J/ψ production systematic measurements of open charm production are urgently needed. Such measurements would allow to disentangle between initial and final state effects, revealing properties of hidden and open charm transport through the dense medium created in nucleus-nucleus collisions.

2.3.3 Charm measurements at higher energies

Detailed charm measurements are performed at RHIC [34] and LHC [35, 36], where energies are much higher then at SPS and as consequence the charm particle production cross sections are significant higher. In Fig. 2.7, the multiplicities of charm mesons in the central Au+Au collisions from AGS to RHIC energies as predicted by the HSD model are presented. According the these predictions, charm meson measurements are rather challenging at SPS energies due to the low yields.

The charm measurements at $\sqrt{s_{\rm NN}} = 200$ GeV were performed at the Solenoid Tracker at RHIC (STAR) [34] and the Pioneering High Energy Nuclear Interaction eXperiment (PHENIX) [37]experiments located at RHIC. The nuclear modification factor R_{AA} dependence on N_{part} is shown in Fig. 2.8 for high (left panel) and low (right panel) transverse momenta p_T. For high transverse momenta the R_{AA} shows consistency for open charm

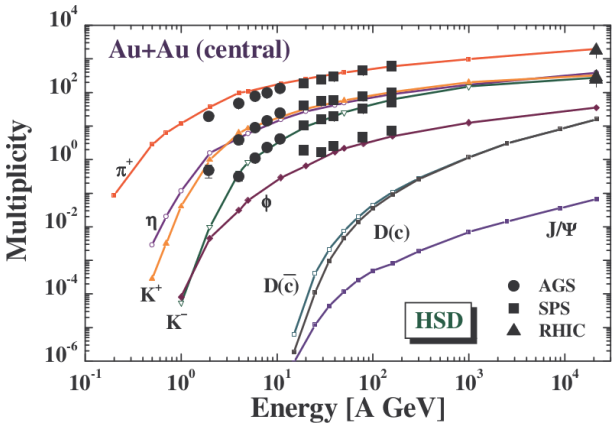

Figure 2.7: Overview of the experimental meson multiplicities of π, η, ϕ, K^+,K^-, D, $\overline{D}$ and J/ψ observed in central Au+Au collisions as a function of the collision energy from AGS to RHIC energies. The lines show the HSD model predictions [16].

and charmonia, however at low p_T R_{AA} for open charm is consistent with unity within the errors but R_{AA} for J/ψ shows significant suppression by up to 75% for the most central collisions. This J/ψ suppression at low transverse momenta can be attributed to presence of the final state iterations [22].

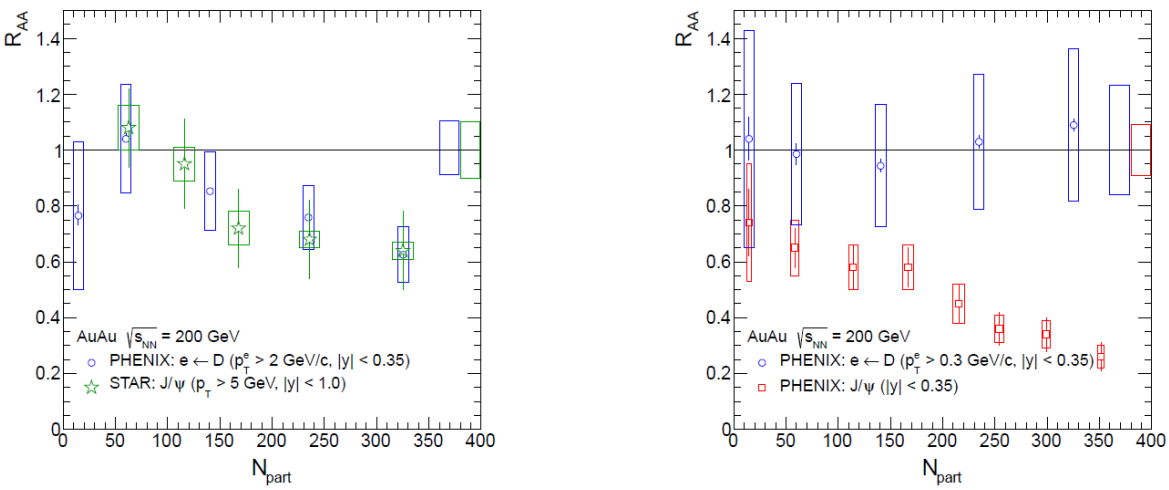

Figure 2.8: Comparison of the nuclear modification factor R_{AA} for J/ψ and open charm production at high (left pad) and low (right pad) transverse momenta based on data obtained by STAR and PHENIX for Au+Au collisions at $\sqrt{s_{\rm NN}} = 200$ GeV [22, 34, 37].

At LHC a comparison at such low p_T is not yet conclusive due to difficulties in measuring low transverse momentum D mesons. Fig. 2.9 shows the dependence of R_{AA} for J/ψ and open charm on number of participants for intermediate (left panel) and high (right panel) p_T obtained in A Large Ion Collider Experiment (ALICE) [35, 38] and the Compact Muon Solenoid (CMS) experiment [36]. For both cases J/ψ and open charm productions are significantly decreasing with increasing of the centrality. Since the reduction of the J/ψ is in complete agreement with open charm reduction, there is neither suppression not enhancement of J/ψ production and fraction of $\langle c\bar{c}\rangle$ converted to J/ψ remains the same for A+A and p+p collisions [22].

Therefore, on the example of higher energies it is clearly seen how important for interpretation of the medium effect is to obtain data on both the charmonium and the open charm meson yields.

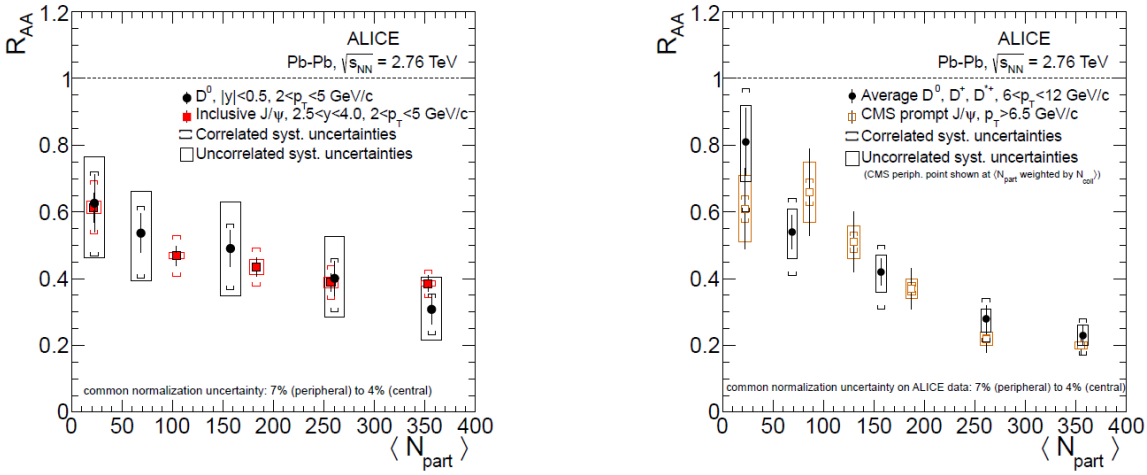

Figure 2.9: Comparison of the nuclear modification factor R_{AA} for J/ψ and open charm production at high (left pad) and low (right pad) transverse momenta based on data obtained by ALICE and CMC for Pb+Pb collisions at $\sqrt{s_{\rm NN}} = 2.76$ TeV [22, 35, 36].

2.4 Future facilities for charm measurements

Fig. 2.10 shows present and future facilities and their regions of coverage in the phase diagram of strongly interacting matter. However, not all of them are performing/planning measurements of charm hadrons in nucleus-nucleus collisions:

- LHC and RHIC at high energies ($\sqrt{s_{\rm NN}} \gtrsim 200$ GeV): measurements of charm particles will be performed in a significantly limited acceptance due to the collider kinematics [39, 40, 41, 42]. At very high energy collisions the multiplicities of $c\bar{c}$ pairs is high, which may lead to secondary formation of J/ψ mesons, preventing the study of the in-medium effect of produced J/ψ mesons;
- RHIC Beam Energy Scan (BES) collider ($\sqrt{s_{\rm NN}} = 7.7 - 39$ GeV): measurement are not considered in the current program due to difficulties related to collider geometry and kinematics as well as the low charm production cross-section [43, 44];
- RHIC BES fixed-target ($\sqrt{s_{\rm NN}} = 3 - 7.7$ GeV): not considered in the current program [45];
- SPS ($\sqrt{s_{\rm NN}} = 5.1 - 17.2$ GeV):
  - The SPS Heavy Ion and Neutrino Experiment (NA61/SHINE): direct open charm measurements are planned after LHC Long Shutdown 2 with upgraded experimental facility, see more details in Chapter 9 [12];
  - NA65/DsTau experiment: measurements of D_s mesons in p+A collisions are planned to be performed in order to study τ neutrinos [46];
- NICA ($\sqrt{s_{\rm NN}} < 11$ GeV): open charm measurements during stage 2 (after 2023) are considered [47];
- Japan Proton Accelerator Complex - High Intensity (J-PARC-HI) ($\sqrt{s_{\rm NN}} \lesssim 6$ GeV): under consideration, might be possible after 2025 [48];

- The Facility for Antiproton and Ion Research (FAIR) SIS-100 ($\sqrt{s_{\mathrm{NN}}} \lesssim 5$ GeV): measurements of charm hadrons are not possible due to the very low cross-section at SIS-100, systematic charm measurements are planned with SIS-300 ($\sqrt{s_{\mathrm{NN}}} \lesssim 7$ GeV), however no time estimation available [49].

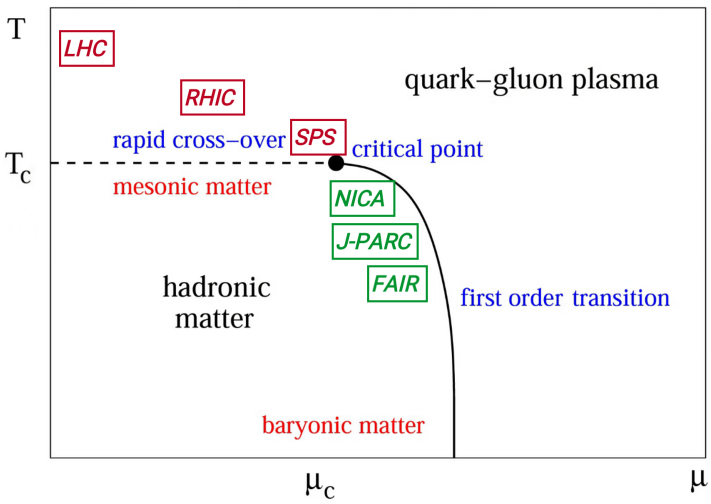

Figure 2.10: Sketch of the phase diagram of strongly interacting matter with indicated regions probed by present (red) and future (green) heavy ion facilities [50].

Recently performed by NA61/SHINE measurements of open charm (which are the topic of this thesis) and planned after LHC Long Shutdown 2 will be the only available measurements of open charm production in heavy ion collisions at high energies in the near future. The corresponding potential measurements at very high (LHC, RHIC) and lower (FAIR, J-PARC) energies could complement the NA61/SHINE results and establish collision energy dependence of charm production. Potential measurements at NICA and RHIC BES fixed target will allow to cross-check the NA61/SHINE data.

In summary:
Direct systematic measurements of open charm production have never been performed before at the SPS energy range due to complications related to their low yield and short life-time, however they are urgently needed for the interpretation of the existing results on J/ψ. This will allow to obtain model-independent information on suppression or enhancement due to the medium formed in the collision. Also such study gives a unique opportunity to test the validity of theoretical models based on dynamical and statistical model approaches for nucleus collisions at SPS energies, which provide very different predictions for charm yields.

Chapter 3

New Small Acceptance Vertex Detector in the NA61/SHINE experiment

3.1 The NA61/SHINE experiment

3.1.1 The physics programme

The SPS Heavy Ion and Neutrino Experiment (NA61/SHINE) [51, 52] was designed for studies of the properties of the onset of deconfinement and search for the critical point of strongly interacting matter. These goals are being pursued by performing a comprehensive two-dimensional scan of the phase diagram of strongly interacting matter. This is done by varying the system size by colliding the following systems: p+p, Be+Be, Ar+Sc, Xe+La, and Pb+Pb and the beam momenta from $13A$ to $158A$ GeV/c ($\sqrt{s_{NN}} = 5.1$ – 17.3 GeV/c) for ions and up to 400 GeV/c for protons. Collected data would allow to cover the region, where the critical point is expected (according to one of lattice calculations $T = 162 \pm 2$ MeV and $\mu_B = 360 \pm 40$ MeV [53]).

Beyond the strong interactions programme, NA61/SHINE is also performing reference measurements for long-baseline neutrino and cosmic-rays experiments. The goal of the neutrino program is to collect data on particle spectra in p+C interactions, as the reference for the T2K experiment [54]. The goal of cosmic rays program is to collect data on particle spectra in p+C, p+p, π+K and K+C interactions as the reference for the cosmic-ray experiments (Pierre-Auger and KASCADE) [54]. Recently, the program of NA61/SHINE was extended by Fermilab neutrino program to collect high-precision data on hadron production to improve beam modeling for future experiments at Fermilab [55].

3.1.2 Beam acceleration chain

The facility of NA61/SHINE is placed in the H2 beamline of the North Area of SPS in the European Organization for Nuclear Research (CERN). The CERN accelerator complex is shown in Fig. 3.1. Before beam reaches the North Area it passes through a series of accelerators.

SPS obtains accelerated ions, such as lead and xenon, originating from the Linear accelerator 3 (Linac3), which accelerates ions to momenta of $4.2A$ MeV/c. The Linac3 delivers the particles to the Low Energy Ion Ring (LEIR). After acceleration in LEIR the

ions with momenta of $72A$ MeV/c are injected into the Proton Synchrotron (PS) where they can reach momenta upto $25A$ GeV/c. As the next step, these ions are sent to the SPS where they are accelerated further, to the final desirable momenta, and delivered to the experiments located in the North Area.

In case of proton beams, their starting point is the Linear accelerator 2 (Linac2), which delivers the particles accelerated to momenta of 50 MeV/c to the PS Booster. In the PS Booster protons achieve momenta of 1.4 GeV/c. Later, after acceleration, they are sent to PS, which can push the proton beam to the maximal momentum of 25 GeV/c, and then to SPS.

Ion beams with momenta of $13A$–$25A$ GeV/c are injected to SPS. After acceleration is SPS beams can reach momenta of $13A$–$158A$ GeV/c and then are delivered to the North Area. Recently due to safety rules the maximal momenta of ion beams was restricted to be $150A$ GeV/c. Proton beams having momenta before SPS of 13–25 GeV/c reach the North Area with momenta of 13–450 GeV/c.

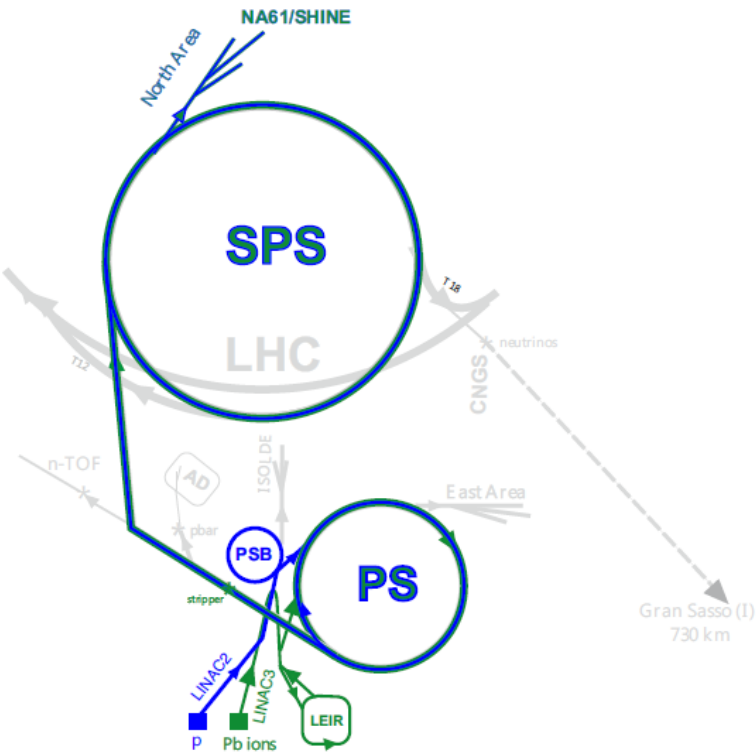

Figure 3.1: Schematic layout of the CERN accelerator complex with its components relevant the NA61/SHINE ion and proton for beams operation shown with bold lines (not to scale) [52].

3.1.3 The experimental facility

NA61/SHINE is a fixed target experiment, and fixed target experiments are suited more then a typical collider experiment for detection of strange and multi strange particles, as well as heavy flavours, like charmed particles. The layout of the experimental setup is shown in Fig. 3.2.

The main components of the facility is large acceptance hadron spectrometer, which was inherited from the NA49 experiment [56].

The setup includes the beam position detectors (BPD), Cherenkov counters and the scintillator detectors located upstream the target, which provide information on timing,

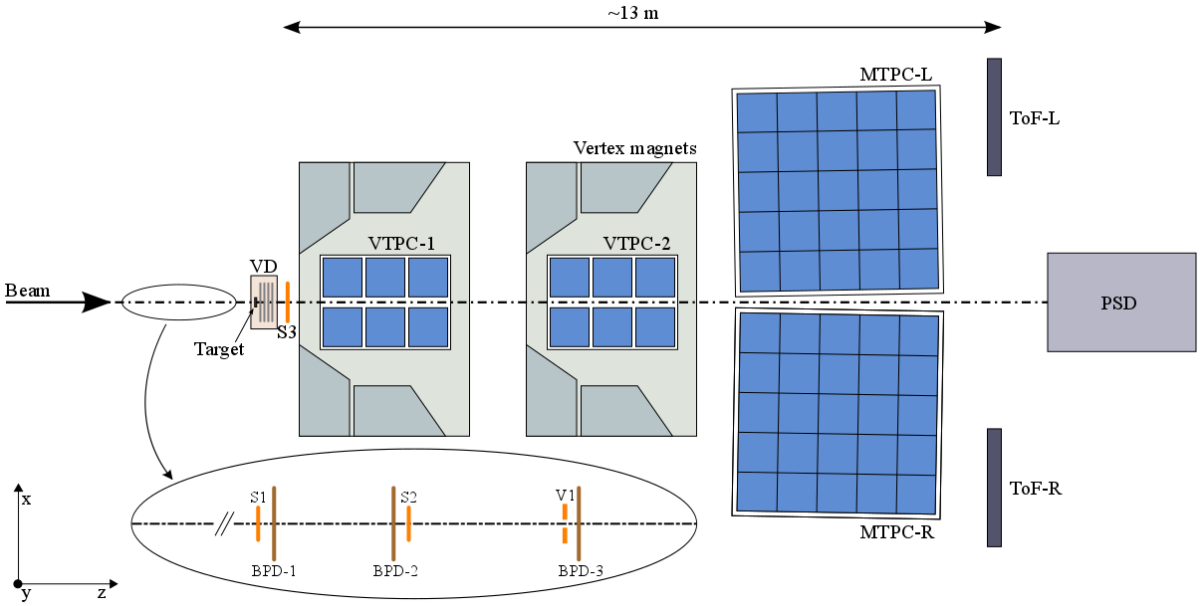

Figure 3.2: Layout of the NA61/SHINE experimental set-up used during Pb+Pb data taking in 2016 (top view, not to scale) [52].

charge and position of beam particles. The experiment includes two Vertex Time Projection Chambers (VTPC-1 and VTPC-2), which are located inside magnets, Gap TPC and two main TPCs (MTPC-L and MTPC-R). These TPCs provide acceptance in the full forward hemisphere, down to $p_T = 0$. The TPCs allow for tracking, momentum and charge reconstruction as well as measurement of mean energy loss per unit path length. The Time of Fight (ToF) walls which are used for additional particle identification measurements are located behind the main TPCs. The Projectile Spectator Detector (PSD) measures the energy of projectile spectators and delivers information on collision centrality.

The detailed description of the facility could be found in [52].

Beam detectors and triggers

To provide information about properties and position of the beam a set of scintillator and Cherenkov detectors and small proportional chambers have been placed along the beam upstream of the target. Also, counters are placed downstream of the target for triggering events with an iteration.

The S1 and S2 scintillation counters provide precise timing reference for the triggering system, signals coming from these counters are used in coincidence in the trigger logic. S1 delivers the starting signal to start data registration in all readout systems. The S1 and S2 scintillators measure the energy deposited by passing through them beam ions, which allows to determine type of beam particles.

The veto scintillation counter V1 has a hole in its centre, which allows to register and reject in anti-coincidence logic beam halo particles.

The scintillation counter S3 is located downstream of the target on the beam line and is used for selection inelastic iterations of the beam with the target. If the signal from S3 is above some threshold (adjusted for given data taking) the event is recognised as collision with elastic beam iteration

Cherenkov detectors are used for identification of the beam particles and monitor

purity of the beam. They were not used during data taking periods discussed is this thesis.

The position of the incoming beam particles in the transverse plane is measured by a telescope of three BPDs placed upstream of the target. These detectors are proportional gas chambers that are filled with Ar/CO_2 gas mixture in the proportion 85/15. Their active area is 48×48 mm^2. Each detector consists of two orthogonal wire planes sandwiched between three cathode planes made of aluminized Mylar foils. Passing beam particles deposit charge in each BPD which results in a signal in the adjacent strips. The calculation of the average of the strip positions weighted with the corresponding signal's amplitude allows reconstruction of the position of the beam in transverse plane. Combination of three-dimensional points of the beam position (calculated transverse coordinates and position of a BPD along the beam) from each of BPDs allows for reconstruction of the beam particle trajectory towards the target.

Time Projection Chambers

Time Projection Chambers are the main tracking detectors of the NA61/SHINE experiment. They consist of large gas volumes which are ionised when charged particles are crossing it. The produced electrons drift with a constant velocity in the electric field towards the top plate of a TPC. The plates of TPCs are Multi-Wire Proportional Chambers (MWPC), they are divided to segments called pads. MWPCs are build from gating grid, cathode, anode and pad planes. Gating grid prevents positive ions to drift back to the drift volume. During triggered event the gate is open and electrons came to cathode plane, and afterwards the gate closes and prevents electrons from entering the amplification region. The charge signal is amplified and collected. Using the information of positions of the clusters in the pad plane and knowing the arrival time the trajectory of the particle inside TPCs could be reconstructed.

Two of TPCs, called VTPC-1 and VTPC-2, are located inside super-conducting dipole magnets. The magnetic field is parallel to the electric field, thus it doesn't affect the drift direction. For the beam momentum $150A$ GeV/c the field in VTPC-1 is 1.5 T and in VTPC-2 is 1.1 T, the field is scaled down proportionally for lower beam momenta. Presence of the magnetic field allows measurements of the charge and momenta of the particles produced in the interaction based on their track curvature. Also, in MTPC-L and MTPC-R track reconstruction is easier due to the fact that tracks are more uniformly distributed in their volume because of bending. Moreover, TPCs allow particle identification using energy loss per path length (dE/dx) method.

TPCs are filled with Ar/CO_2 gas mixture in the proportion 90/10 in VTPCs and 95/5 in MTPCs. Drift velocity is measured by the Detector Control System (DCS) in each TPC separately. This measurement serve as an input to the drift velocity calibration procedure (see Chapter 5 for more details).

NA61/SHINE is also quipped with smaller TPCs called Gap TPC and Forward TPCs (FTPC): FTPC-1, FTPC-2 and FTPC-3. They are centred on the beam line and cover a narrow cone around the beam direction allowing measurements of particles with very small track angles. However, they are not used for heavy-ion system collisions due to the high track density and the large deposited charge by the beam ions.

Time-of-fight detector

The Time of Fight walls (ToF-L, ToF-R and ToF-F) installed behind the main TPCs consist of a large set of rectangular scintillator detectors. ToF-F is used only for reactions with low multiplicity of produced particles, thus it is not used for heavy-ion collisions. ToF detectors are used for particle identification. They measure time of flight of the particle with high precision (on the level of several tens of ps). The detector register the arrival time of the particle with respect to trigger time. The particle mass m is obtained knowing time of flight t, particle momentum p and measured track length l by formula: $m^2 = (p/c)^2((ct/l)^2 - 1)$.

The information delivered by ToF detectors are not used in the analysis presented in this thesis, however ToF measurements are used as reference for the performed drift velocity calibration (see Chapter 5 for more details).

Projectile Spectator Detector

The most downstream detector in the NA61/SHINE facility is Projectile Spectator Detector. This is a zero-degree hadron calorimeter which measures the energy of the projectile nucleons, which didn't interact in the collision. A hadron interacting with the material of the calorimeter creates a particle cascade followed by electomagnetic cascade, which leaves all its energy inside. This deposited energy is probed by scintillators. The deposited energy is proportional to number of projectile nucleons, thus it allows to determine the centrality of the collision.

PSD consists of 16 small (10×10 cm^2) and 28 large (20×20 cm^2) modules, each 150 cm long. Each module has sandwich structure of lead and scintillator layers perpendicular to the beam.

3.2 The Small Acceptance Vertex Detector

For open charm measurements in nucleus-nucleus collisions, the NA61/SHINE experimental setup was upgraded with the Small Acceptance Vertex Detector (SAVD) - a first version of the future detector introduced to test the possibility of the open charm measurement in the fixed target experiment.

3.2.1 The concept

As was already mentioned, open charm mesons are difficult to measure because of their low yields and short life times. These mesons could be measured in their decays channels into pions and kaons, however, in heavy ion collisions πs and Ks are produced in large numbers by other sources giving huge background. To distinguish the daughter particles of D^0 mesons from hadrons produced in primary nucleus-nucleus interaction, one aims to select only hadron pairs generated in a secondary decay vertex. To reconstruct the vertex the trajectories are extrapolated to the target region and intersection points are identified. The primary vertex will typically appear as intersection point of multiple tracks while the tracks of daughter particles originating from selected decays will intersect at the well-defined displaced point (secondary vertex) (see Fig 3.3).

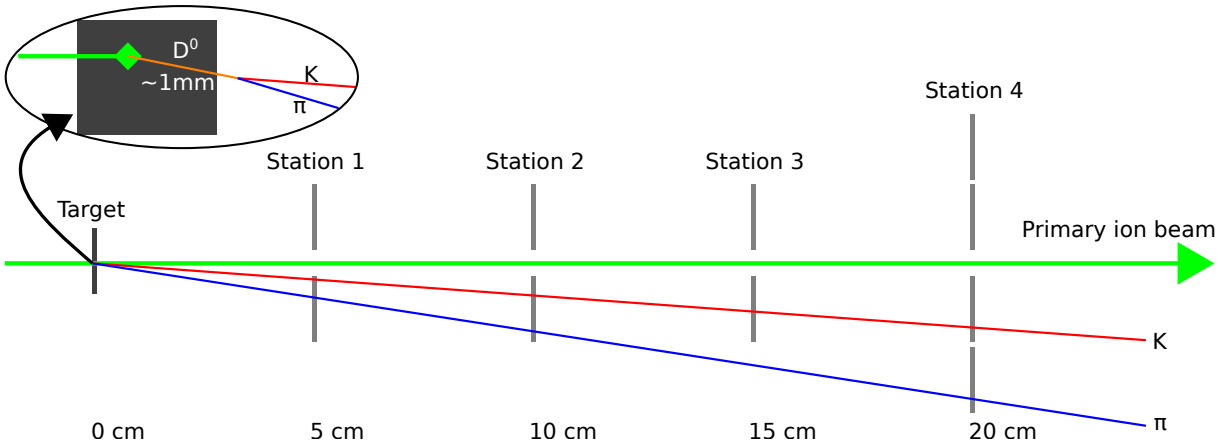

Figure 3.3: Visualization of D^0s reconstruction strategy via their decay into charged pion and kaon ($D^0 \rightarrow \pi^+ + K^-$). The role of Vertex Detector providing precise tracking close to the target is emphasized in the insert (*top-left).*

3.2.2 The detector setup

The SAVD was designed to improve spacial resolution of particle tracks and vertices. The detector concept was developed in simulations [57, 58, 59].The goal was to keep number of sensors low while acceptance of the system would cover most of produced open charm mesons.

The SAVD is positioned between the target and VTPC-1 (see Fig. 3.4). In Fig. 3.4 the photograph of the detector is presented. It consists of two spectrometer arms (called Jura and Saleve according to the standard NA61/SHINE convention: the Jura arm is located on the Jura Mountains side of the experiment (left relative to beam direction) whereas the Saleve arm is located on the Saleve Mountains side (right to the beam)). Each arm is composed of four planes (stations) located at 5, 10, 15 and 20 cm distance downstream of the target. Each arm hosts in total eight coordinate-sensitive pixel detectors (sensors) for all station.

High position resolution silicon pixel MIMOSA-26AHR Monolitic Active Pixel Sensors (MAPS) on the CMOS (Complementary Metal-Oxide-Semiconductor) technology [60] were chosen as the basic detection element of the SAVD stations. The sensors have very low material budget (50 μm thickness), which significantly decrease multiple scattering effect on the detection planes. The 1.06×2.13 cm^2 sensitive area of a single MIMOSA-26 sensor is covered by 1156 columns made of 576 pixels (which gives 663.5k pixels/chip). The pixel pitch is 18.4 μm in each direction, which leads to high spatial resolution on 5 μm [61].

The MIMOSA-26AHR sensors are mounted on extra-light weight vertically oriented carbon fibre support "ladders", developed for the upgrade of ALICE ITS [62]. The ladders are held by dedicated C-shape support frames as shows in Fig. 3.4. The ladders have integrated pipes for water cooling and are mounted in C-frames made from aluminum. The four C-frames of each arm share a movable support plate, which allows to put the sensors into a save position during beam tuning. The first and second stations consist of one ladder each holding one sensor, the third stations consist of one ladders holding two sensors and the last station consist of two ladders holding two sensors each. The layout of the sensors is illustrated in Fig. 3.5.

A target (made of lead or lanthanum) was placed in front of the arms on an additional,

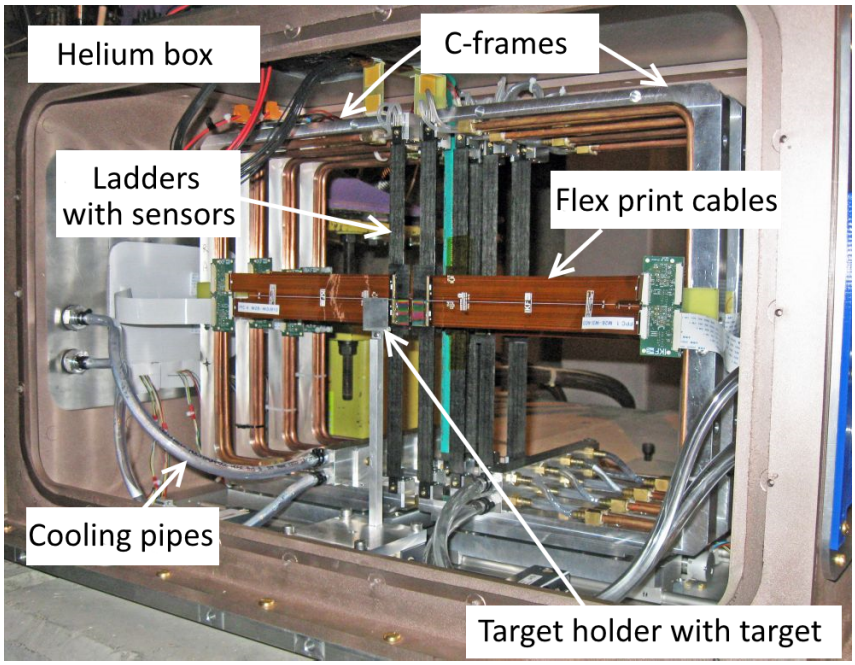

Figure 3.4: Photograph of the SAVD before closing the detector with the front and exit windows. The detector elements are indicated.

movable support.

Further, the whole structure is installed on a thick aluminium base plate, which provides mechanical stability. After installation of front and back windows made of thin Mylar foils, the SAVD arms and the target are kept in a helium enclosure (aquarium). The helium gas (held at atmospheric pressure) helps to minimise beam-gas interactions and the multiple Coulomb scattering of the produced particles.

The device is located close to the edge of the VTPC-1 magnet, thus the magnetic field in the SAVD volume is small and inhomogeneous (0.13 - 0.25 T).

The estimated average material budget of the detector in its active area amounts $\sim 0.3\%\ X_0$.

All columns of the sensor are read out in parallel in the rolling shutter mode. The readout time is equivalent to the time resolution and is 115.2 μs, which is sufficient for data taking at the collision rate <1 kHz (the NA61/SHINE collision rate is on the level of 80 Hz).

The local DAQ of SAVD is depicted in Fig. 3.6. It relies on hardware and software modules, which were initially developed as the prototype of the CBM Micro Vertex Detector [63] and adopted to the needs of SAVD.

The sensors are connected to front-end boards (FEBs), which are located outside of the SAVD acceptance on the C-frames. The role of FEBs is to stabilise bias voltage provided to sensors but they also interface slow and fast control between the sensors and the converted boars (CB), which are located outside of the SAVD box. The converter boards host remote controlled voltage regulators. Moreover, the boards host a latch-up protection system. This system scans the bias currents of the sensors individually for possible over-currents as caused by latch-up. In case a short circuits is detected, a rapid power cycle on a given sensor is enforced.

The sensors are steered and readout by two TRBv3 FPGA boards [64]. The TDC-

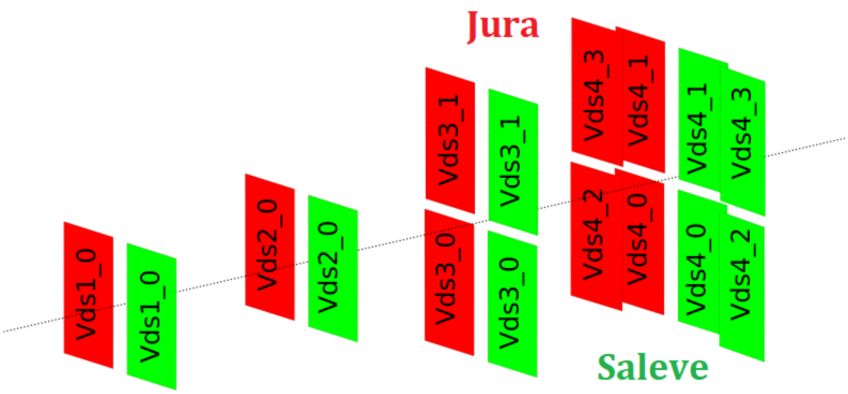

Figure 3.5: The layout of the SAVD sensors. Naming convention of the sensors is indicated.

firmware of this board was replaced by a dedicated code for steering MIMOSA-26 sensors. Hereafter, each board served the sensors of one detector arm. During the 2016 test run, the two boards were operated with internal clock. In consequence, the data was synchronized based on the global trigger of NA61/SHINE, only. During data takings in 2017 and 2018, the boards were operating on a common clock and the sensors remained synchronized also in hardware.

The sensors and the TRBv3 boards operate continuously and stream out their data with the UDP protocol through gigabit-Ethernet interface to a DAQ-PC. To synchronize the data with the trigger of NA61/SHINE, the TRBv3 boards receive the trigger signal via the converter board. Information on the arrival time of the trigger is added in real time to the data stream but for the sake of simplicity, the data selection is performed in software on the DAQ-PC. Five sensor frames per trigger were forwarded to the central DAQ after the selection was performed, all other data was rejected. The DAQ-PC also performs basic checks on data integrity. In the case of inconsistencies suggesting sensor mulfunctioning, a sensor reset is scheduled and the necessary reprogramming of the sensors via the JTAG interface is performed during the next spill break.

The data acquisition push data mode is protected by a busy logic, which prevents mixing events with different trigger numbers. If any of the detector busy logic lines is asserted, the whole system needs to wait. If this waiting time surpasses delay limit, data acquisition is stopped and all subsystems run through restart procedure.

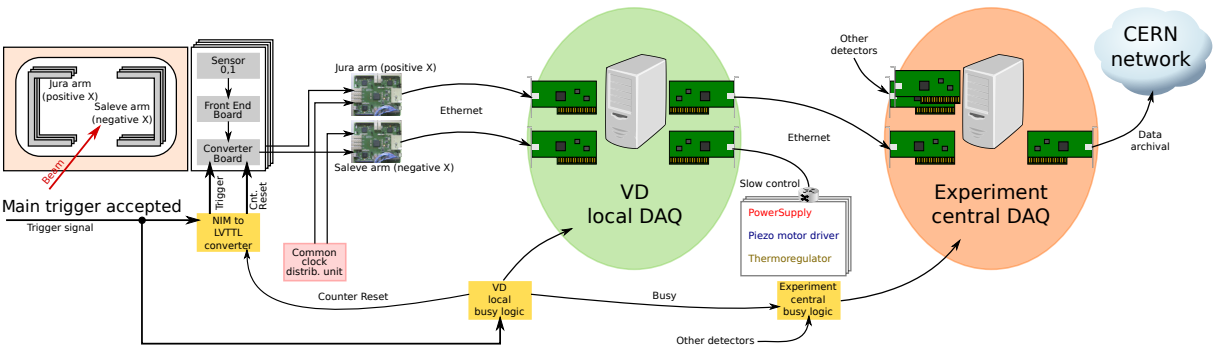

Figure 3.6: Schematic diagram of SAVD readout in NA61/SHINE experiment.

The sensors are connected to the FEBs through 20 cm long Flex Print Cables (FPCs). This made it possible to place the FEBs outside the VTPC acceptance to reduce the

material budget seen by them. Since MIMOSA-26AHR do not have internal filters, this made them more susceptible to pick-up noise injected by the long cables. However, adding external capacitors on filters reduced the problem.

The sensor is performing an internal signal discrimination, zero suppression and a first stage of data compression. Four threshold values set for each chip may be set, they are shared by the pixels of 289 columns (each sensor has four segments). For the optimal trade-off between registration efficiency of the sensors and noise rejection the thresholds should be tuned accurately. Increasing the thresholds will suppress the noise, however it results in lost of signals hits and degraded the reconstruction efficiency. On the other hand, decreasing the threshold will increase the probability of false tracks. During data takings (except first pilot data taking) sensor efficiencies were kept well above 90%, while keeping noise on the acceptable level of $<10^{-4}$ hits per pixel per frame.

Chapter 4

Data reconstruction

The NA61/SHINE experiment has its own software framework called SHINE Offline Framework. The data processing, namely reconstruction, simulation, calibration, analysis, etc. is performed within this software. When SAVD was introduced to the experiment all SAVD-related software was being integrated to SHINE Offline Framework.

For the plots presented in this Chapter, no event selection was applied.

4.1 Data reconstruction in TPC detectors

During the event reconstruction process the digitised signals from all NA61/SHINE detectors are translated to particle trajectories and other characteristics. Data reconstruction in TPCs consists of the several steps described below.

As the first step the reconstruction of TPCs clusters is performed. The algorithm is looking at the obtained signals on TPC pads in all time-slices of the event and searching for signals located on the adjacent pads that are in the correlated time-slices. These associated together signals are merged and called a cluster. The 3D position of the cluster is calculated using the centre-of-gravity method taking into account the deposited charge in a given pad in a given time-slice.

After all clusters in TPCs are found, neighbouring clusters are connected into so-called local tracks in each of TPCs separately. In MTPC-L and MTPC-R, which are located outside the magnets, the found tracks are fitted with strait lines, while in VTPC-1 and VTPC-2 tracks are fitted using the Kalman Filter algorithm since they are curved in the magnetic field.

Further, the matching of the local tracks is performed and merged track called global track is refitted taking into account clusters from all local tracks. This procedure allows to determine parameters of the tracks such as momentum, electric charge sign and energy loss.

The last stage of event reconstruction concerns reconstruction of the primary vertex. The z position is fitted using extrapolated to the target region TPC tracks; the x and y positions of the primary vertex are calculated by extrapolating the beam trajectory measured by BPDs to the interaction plane. In high track multiplicity events, the vertex resolution is on the level 150 μm in the bending plane and on the level of 2 mm along the beam direction [65]. After finding the primary vertex the global tracks are assumed to be primary tracks, and are refitted after adding to the set of clusters an extra point representing the position of the primary vertex. The resulted tracks are called vertex tracks.

Also, the reconstruction algorithm can search for secondary vertices: for each pair of tracks the algorithm attempts to reconstruct a secondary vertex, and if the secondary vertex is enough distant from the primary vertex the tracks are assigned to it; this procedure works mostly for particles with mean life time on the level of several centimetres as Λ and K_s^0.

The spatial resolution of clusters defined as an average distance between te points and reconstructed trajectory is on the level of several hundred μm. The momentum resolution is $\sigma/p^2 \sim 10^{-4}$ (GeV/c)$^{-1}$. [65].

4.2 Data reconstruction in SAVD

4.2.1 Cluster reconstruction

The first step of data reconstruction is cluster recognition. A particle passing through a sensor may fire more than one neighbouring pixel in a given sensor. These pixels should thus not be considered independent particle hits, but rather together constituting a particle hit. Such a composite particle hit is called a "cluster". A computer algorithm, the so-called "clusteriser", is used to identify such clusters. It takes each pixel as a starting point, and searches neighbouring pixels for hits in both dimensions. The search is repeated recursively for neighbouring fired pixels until no more neighbouring fired pixels can be found. The set of fired pixels is used to calculate the centre-of-gravity, which is taken as the centre of the resulting clutter.

All sensors columns are read out simultaneously row by row, in the continues cycle which is not synchronized with collision triggers. The data set read during the single readout cycle is called a frame. Every frame contains so-called timer – the information about time that passed between the start of the trigger and the instance at which a readout process of the given frame was initialised.

For each triggered collision, a total of five complete frames (numbered from 0 to 4) are read out and stored as raw data to assure all potentially valuable data is preserved. The timer distribution for the first frame which is spanned in the interval from 0 to the integration time of the sensor (t_{int} = 115.2 μs) is shown as the black histogram in Fig. 4.1 (frame 0), further frames (1, 2, 3, 4) are shown as coloured histograms. Timer of the nth frame is equal the timer of the 0th frame + $n \times t_{int}$, which is reflected in the distribution. Since the trigger arrival time is independent from the readout time of sensor, the distribution of the timer is uniform.

The dependence of average pixel multiplicity on timer is plotted on the same Fig. 4.1 with the thick blue line. It is seen, that the average pixel multiplicity significantly increases in the second and third frames, while in others frames only noisy pixels, observed as a continues pedestal, are presented. As an input to the off-line reconstruction (clusteriser), merged data from the 1st and 2nd are used. As mentioned, the sensor is continuously read out row-by-row (columns are read in parallel). Through calibration, it is possible to determine a fixed time offset between the actual arrival of particles generated in the collision, and the receipt of the trigger by the sensor read-out electronics. Thus, the first row (r_o) to be read out after the passing of the particles can be deduced from the timer value:

$$r_o = (1 - \frac{timer}{t_{int}}) * N_{rows}, \tag{4.1}$$

where N_{rows} corresponds to total number of rows in the sensor, i.e 575. This can be any row with equal probability. Hence, the frame to be considered by the clusteriser is composed of the fraction of frame 1 (all rows following r_o) and a complementary fraction of frame 2 (all rows before r_o).

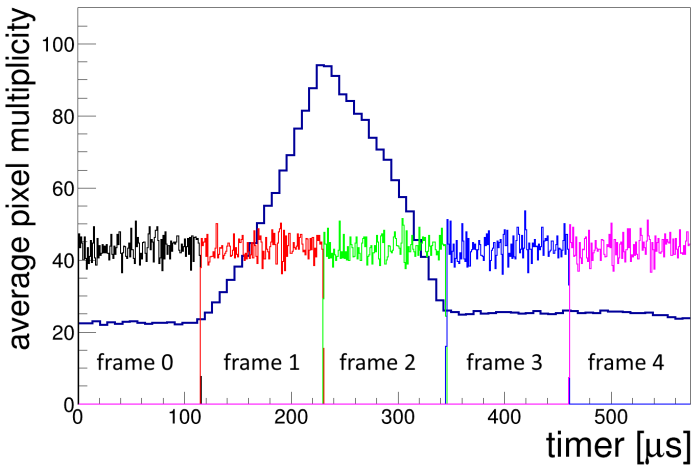

Figure 4.1: The example of average pixel multiplicity versus time (thick blue histogram). With other colours five consecutive frames that were read during event are shown.

4.2.2 Track and vertex reconstruction

Tracks in SAVD are slightly curved because of presence of the magnetic field. However, since this curvature is sufficiently weak it is possible to use a straight line to identify clusters in different SAVD stations belonging to the same track. Consequently, a straight line was chosen as the track model:

$$x(z) = Az + x_0$$
$$y(z) = Bz + y_0.$$

Using this parametrization a combinatorial track identification procedure based on checking the combinations of all hits from different stations was introduced. If the hits detected on different SAVD stations lie on a straight line according to a χ^2 criterion, the combination is accepted as a reconstructed track.

Track reconstruction procedure was firstly implemented for field-off data set. From the distributions of the residuals of hits from the reconstructed and fitted with a straight line tracks, the spatial sensor resolution was determined to be on the level of 5μm as was expected (Fig. 4.2).

It turned out, that the same straight line combinatorial method could also be applied for reconstruction of the tracks for physics data sets with the magnetic field turned on. However, with applied straight line track model for the curved tracks, the hits on the third and forth station of SAVD visibly deviate from the fitted straight line. The result of this is a double-peak structure in the distribution of cluster residuals for the x direction rather than a single Gaussian distribution. This effect is caused by the vertical B_y component of the magnetic field in SAVD volume. Therefore, on the next steps of the reconstruction the positions of hits are fitted using a second order polynomial function for x and linear function for y:

$$x(z) = A_2x^2 + A_1z + x_0$$
$$y(z) = Bz + y_0.$$

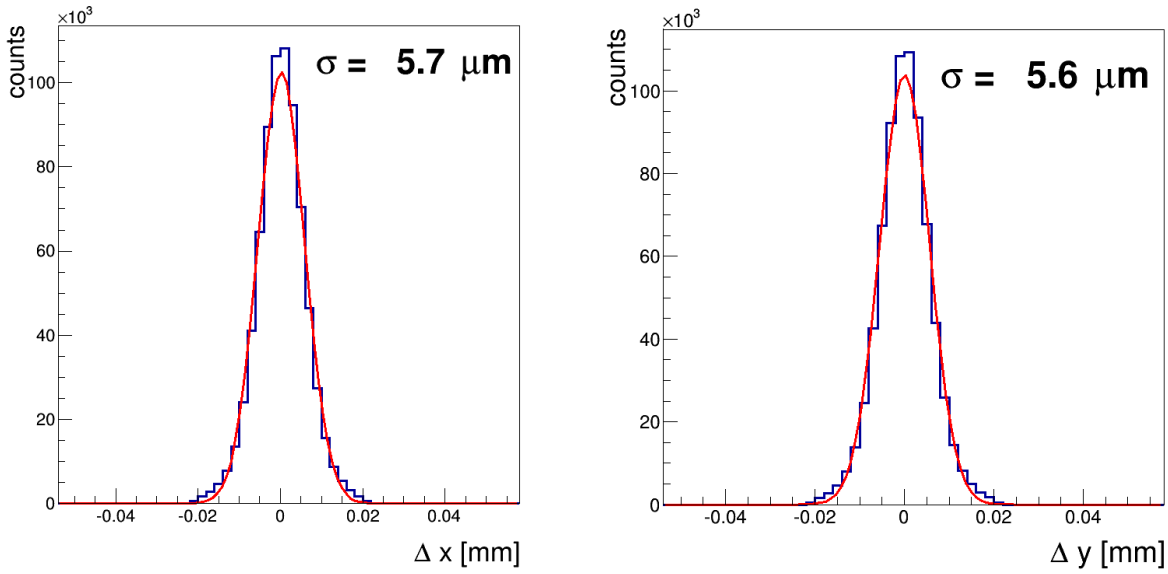

Figure 4.2: Distribution of the x (left pad) and y (right pad) residuals of hits from the straight line fitted to track clusters. Blue lines represent a Gaussian fit to the distributions, the sigma values are indicated on plots. The plots are done for at Xe+La at 150A GeV/c data taken with the magnetic field turned off.

The angular distribution of the reconstructed tracks in the $x - z$ plane is shown in Fig. 4.3. The distribution for each arm has a clear three-peak structure for each arm. Firstly, the narrow inner-most peak (small angles, coloured in green in Fig. 4.3) was associated with particles produced far upstream and travelling parallel to the beam for a long distance. Next, the middle peak (coloured in red) corresponds to particles produced upstream of the target. Finally, the outer peak (coloured in blue) is generated by particles produced in the target – only these tracks are used for further analysis. The distribution was done for Pb+Pb at 150A GeV/c test data set, for Xe+La and Pb+Pb physics data taking the position of SAVD arms was optimised to capture mostly tracks produced on the target.

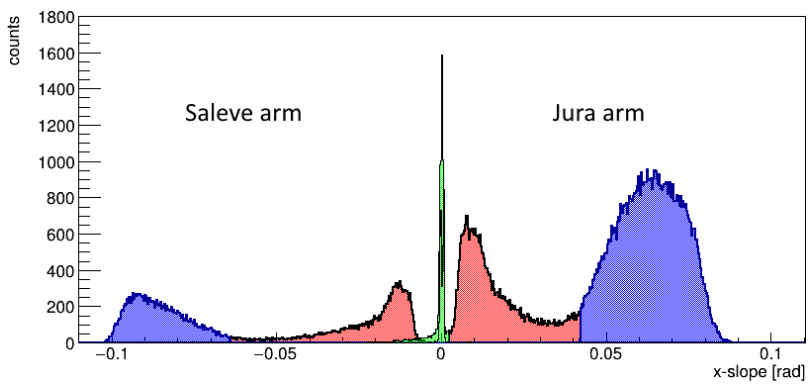

Figure 4.3: Angular distribution of reconstructed tracks in the x, z plane (x-slope) for Jura (positive values) and Saleve (negative values) arms. Plot was done for Pb+Pb at 150A GeV/c test data set.

Fig. 4.3) shows correlation between tracks originating from target that are reconstructed in Jura and in Saleve arms. The plot is done for reconstruction performed in the arm independently, thus the areas for zero multiplicity in Jura or Saleve arms are present. This effect can be suppressed by combining information delivered by both arm as would be discussed below.

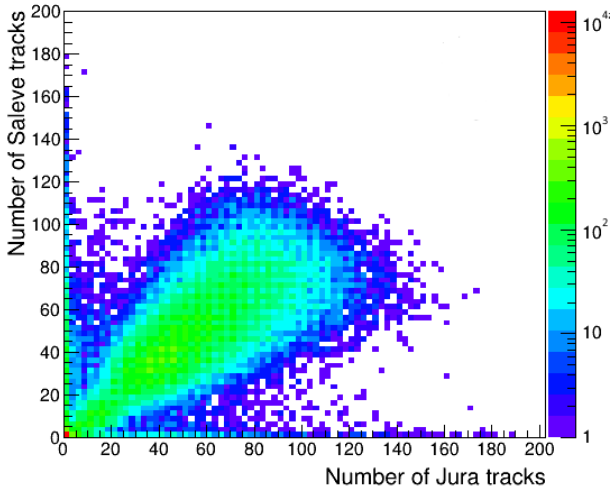

Figure 4.4: Correlation of tracks originating from target reconstructed in Jura and in Saleve arms. Plot was done for Xe+La at 150A GeV/c data set.

The primary vertex is defined as the point of the closest convergence of all reconstructed tracks. Thus, the longitudinal coordinate of the primary vertex is found by minimising the expression:

$$D(z) = \sum_{i<j} \{(A_i z + x_i^0 - A_j z - x_j^0)^2 + (B_i z + y_i^0 - B_j z - y_j^0)^2\},$$

which describes the sum of the relative distances of all track pairs reconstructed in a single event at the given transverse plane defined by the longitudinal coordinate z. The x_{prim} and y_{prim} coordinates are afterwards calculated as the average of x and y positions of tracks at $z = z_{prim}$.

Primary vertex reconstruction was done separately for two samples of tracks with x-slope in the interval 0.02 to 0.04 radian (part of distribution in Fig. 4.3 coloured in red) and with x-slope > 0.04 radian (coloured in blue). The longitudinal distribution of the primary vertex for these samples of tracks (Fig. 4.5) shows that indeed the tracks associated with the most outer peak in Fig. 4.3 originate from the target which is located about 5 cm upstream of the fist SAVD station. The primary vertices associated with tracks from the middle peak in Fig. 4.3 are relatively smoothly distributed upstream of the target in the range from -1200 mm (exit from the beam line) to -50 mm (near the target). At -190 mm the distribution has a sharp peak which is related to interactions in the aluminised Mylar front window of the SAVD cover box. One can also sof 5 ee that between the window and the target the frequency of interaction drops by the factor due to drop of interactions in helium gas kept in the SAVD cover box enclosure. The components of the primary vertex longitudinal distribution associated with the interactions in the target and with the interactions upstream the target can be well separated as the corresponding tracks can be distinguished by their x-slope.

Similar distribution of the primary vertex position could be obtained from the TPC reconstruction procedure. In Fig. 4.2.2 the distributions for reconstructed z position of the primary vertex is shown for target IN and OUT data for Xe+La at 150A GeV/c. It is seen that sometimes the interaction is happening not in the target volume but on detector materials. Vertex distribution using TPC tracks has broader interval then using SAVD tracks due to different acceptance. From these plots it is seen that:

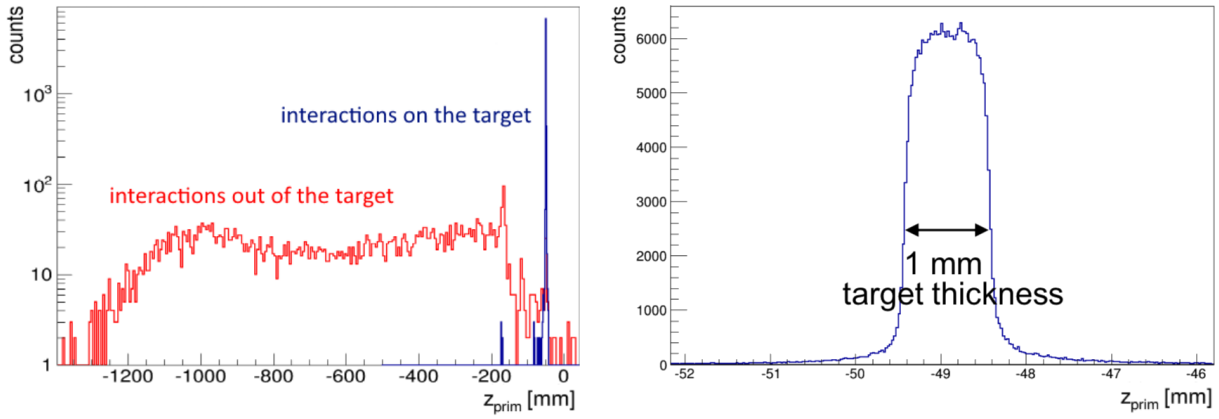

Figure 4.5: Left pad: Distribution of the longitudinal coordinate z_{prim} of primary vertices for two sub-samples of tracks (see text). Right pad: Distribution of z_{prim} for tracks produced in the target. Plot was done for Pb+Pb at 150A GeV/c test data set.

- The distributions for target IN and OUT have similar shape except for target region (-602.5 cm) with for target OUT data was absent (but target holder was still present). This explains absence of the large peak in target OUT data at the target position;
- The distributions start at ∼-680 cm with the peak corresponding to the beam pipe window;
- The next peak at ∼-665 cm is associated with the interactions on BPD-3 materials;
- The distributions relatively smoothly continue from the exit from the beam line to the ∼-610 cm. At this position the distributions have a sharp peak which is corresponds to interactions in the aluminised Mylar front window of the SAVD cover box;
- Further the distributions drop (it is more clear visible on the distribution for the target OUT since the large peak corresponding to the target iterations is not interfering with the background interactions) due to the He filled SAVD box instead of air;
- On the distribution for the target IN data there are two small peaks on both sides of the target (±2 cm) iteration peak which corresponds to enclosure box in which La target was held;
- At ∼-575 cm a peak corresponding to the iterations on the Mylar exit window of the SAVD cover box is located, it has similar size as the front window interactions peak;
- The relatively large peak at ∼-570 cm is associated with the interactions on the S3 scintillator installed downstream to SAVD.

The location of the detector elements seen on the primary vertex distribution is confirmed by the survey measurements.

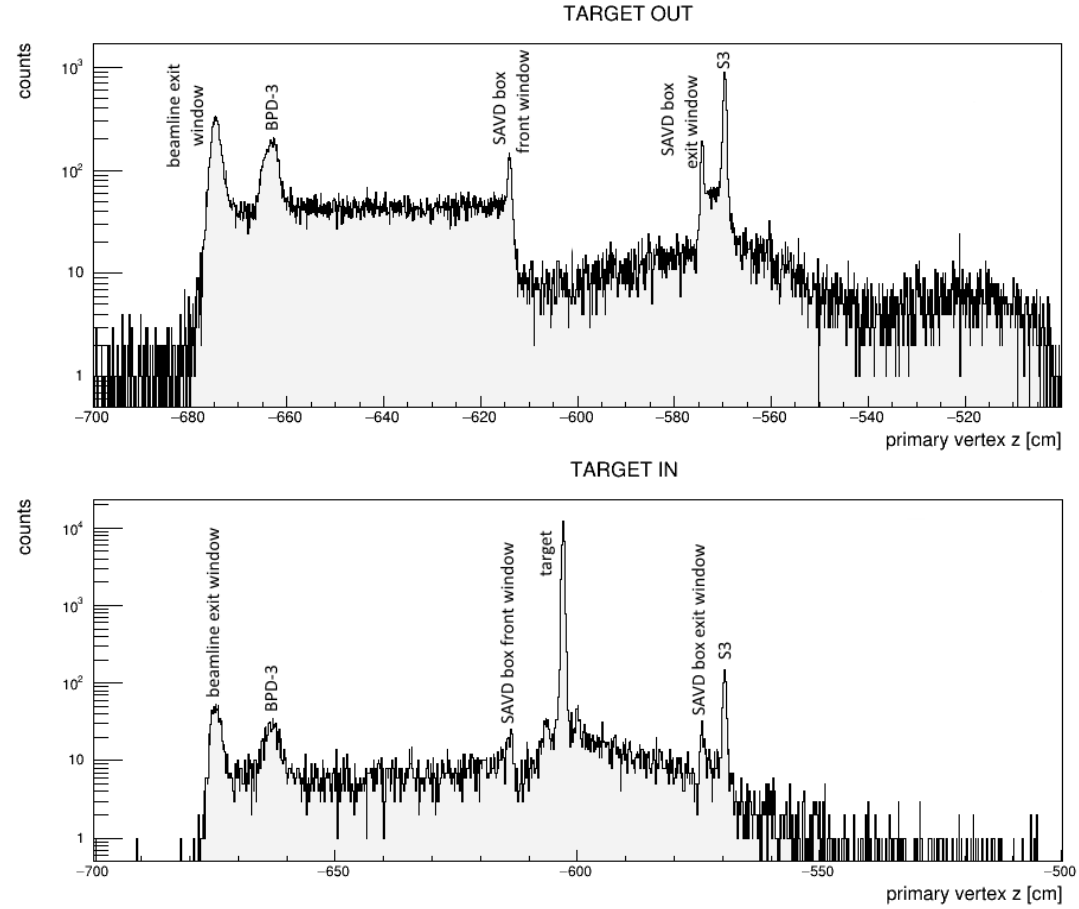

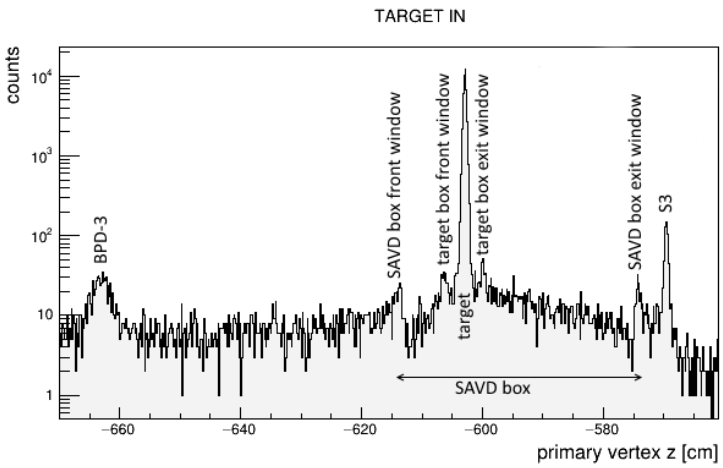

Figure 4.6: Distributions of the reconstructed primary vertex using TPC information for Xe+La at 150A GeV/c data. The distributions are plotted for measurements with target OUT (top pad) and target IN (middle pad) and zoomed in the region around target for the target IN case (bottom pad).

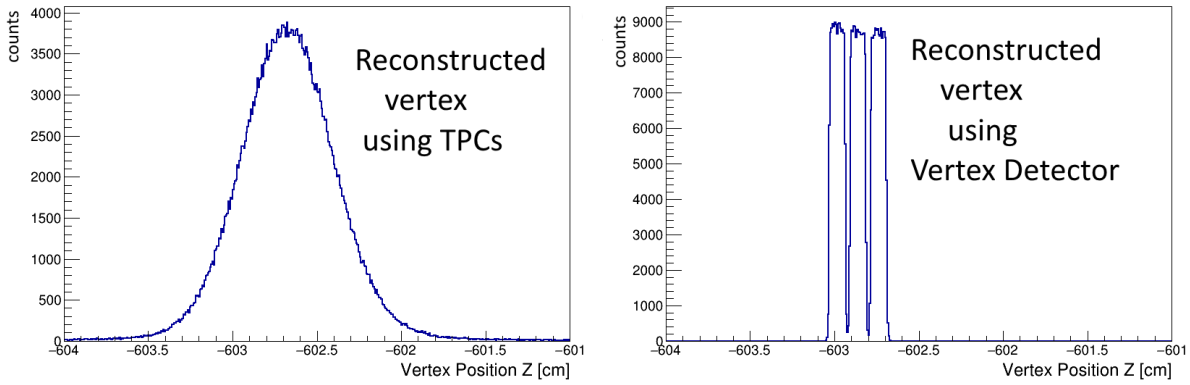

Figure 4.7: Left: Distribution of z_{prim} reconstructed using TPC tracks. Right: Distribution of z_{prim} for SAVD tracks produced in the La target. Plots are plotted in the same z_{prim} scale and were done for Xe+La at 150A GeV/c data set.

The distribution of z_{prim} from the interactions in the target for Pb+Pb test run is shown on the right panel of Fig. 4.5. The near rectangular shape of the distribution allows to reconstruct the thickness of the target (= 1 mm) and its location with respect to SAVD.

For Xe+La run the distribution of z_{prim} from the interactions in the target is presented in the right panel of Fig. 4.7. Segmented target was used for this data taking (three 1 mm thick La blocks squeezed together). The structure of the target can be well seen in the z_{prim} distribution plot.

Applying the same vertex reconstruction algorithm for TPC tracks allows for better vertex resolution then using BPD information. However, sue to much higher cluster position uncertainty and larger distance to the interaction point the TPC vertex has much worse resolution then SAVD. For the comparison the z_{prim} distribution from the reconstructed TPC tracks is shown in the left panel of Fig. 4.7. The target profile is not visible due to poor primary vertex resolution of TPCs.

To determine the spatial resolution of the primary vertex reconstruction, in the simulation study the position of the reconstructed vertex should be compared to the simulated position (see Chapter 8). However it is possible to estimate it based only on the real data. For this purpose the SAVD tracks from the same event were split into two non-overlapping sub-samples, namely every second track from Jura and Saleve arms was assigned to sub-sample 1, whereas the remaining tracks were assigned to sub-samples 2. In this way one obtains two equivalent track samples and the primary vertex spatial resolutions obtained with sub-sample 1 and sub-sample 2 are expected to be identical since the opening angle interval for both samples is the same. The distributions of differences between x, y and z coordinates of the primary vertices reconstructed using tracks from sub-sample 1 and sub-sample 2 are shown in upper pads of Fig. 4.2.2 for Xe+La at 150A GeV/c data, in bottom pads of Fig. 4.2.2 - for Pb+Pb at 150A GeV/c data. In the simulation study it was observed that the widths of the peaks show weak dependency for whole set of tracks and for sub-sample. Thus, the observed widths of the peaks can be converted to the spatial resolution of the primary vertex $\sigma_x \approx 3.9$ μm, $\sigma_y \approx 1.8$ μm and $\sigma_z \approx 29.9$ μm for Xe+La at 150A GeV/c test data set. For Pb+Pb data it was found to be $\sigma_x \approx 3.0$ μm, $\sigma_y \approx 1.4$ μm and $\sigma_z \approx 23.4$ μm. The difference between σ_x and σ_y is caused by the presence of a vertical component of the magnetic field in the SAVD volume. The resolution for

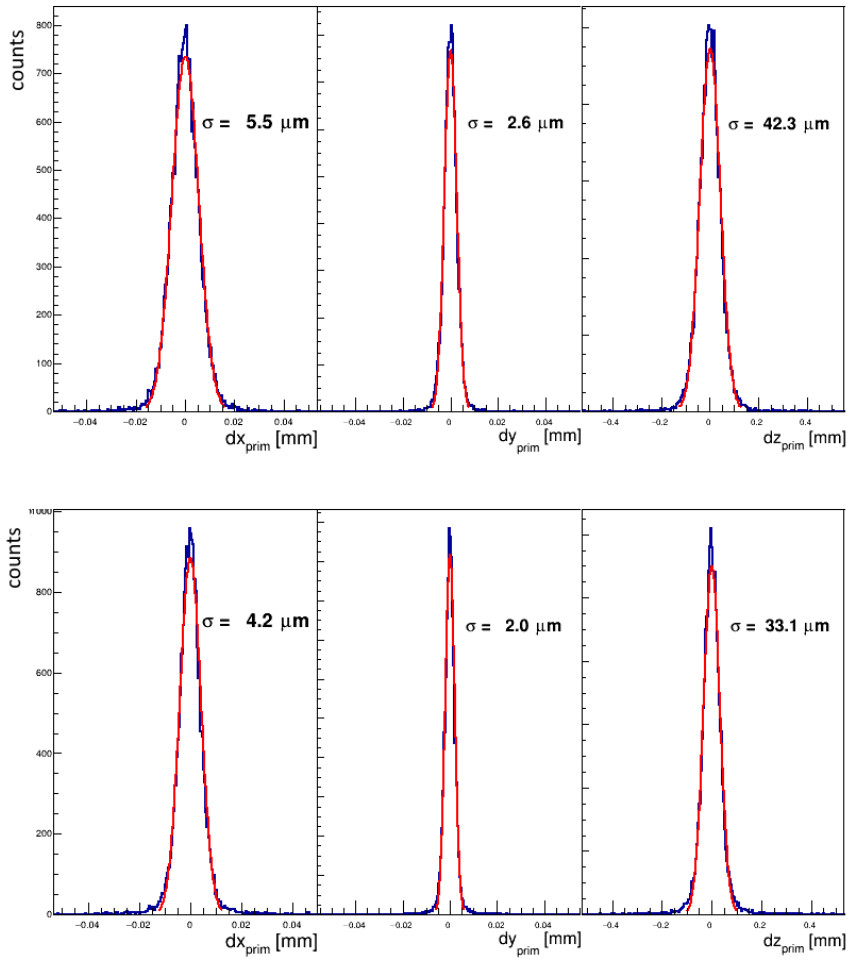

Figure 4.8: Distributions of differences between x, y and z coordinates of the primary vertexes reconstructed using tracks from sub-sample 1 and sub-sample 2 (see text for details) for Xe+La at 150A GeV/c data (upper pads) and for Pb+Pb at 150A GeV/c data(bottom pads). Lines correspond to Gaussian fits to the distributions, the sigma value is shown.

Pb+Pb data is slightly better due to higher track multiplicities.

After the primary vertex is found, in the next step, the algorithm searches for 4-hit and 3-hit tracks using the Hough transform method [66]. It is global method of track reconstruction where each cluster is processed only once. Thus, the time consumption of this method in proportion to number of all detected hits and is much faster, than the combinatorial method, which is accessing clusters in the nested loops over clusters detected in selected stations. However, the HT method requires the information about the origin point thus, it is implemented as a second step of the SAVD track reconstruction chain. The HT procedure is based on representing track as a set of two slope parameters (a_x, a_y), which can be used to describe straight track lines according to following parametrization:

$$x(z) = a_x z$$
$$y(z) = a_y z,$$

where x, y, z are cluster coordinates with respect to the primary vertex position. Then, for each hit its position in coordinate space (x, y, z) are transformed to so-called Hough space of parameters (a_x, a_y). Further, hits that were left by the same particle would have same track parameters and would appear as peaks in the Hough space presented as 2-dimensional histogram. The algorithm is searching for such local peaks which correspond to tracks. However due to multiple scattering and curvature of tracks, hits that belong

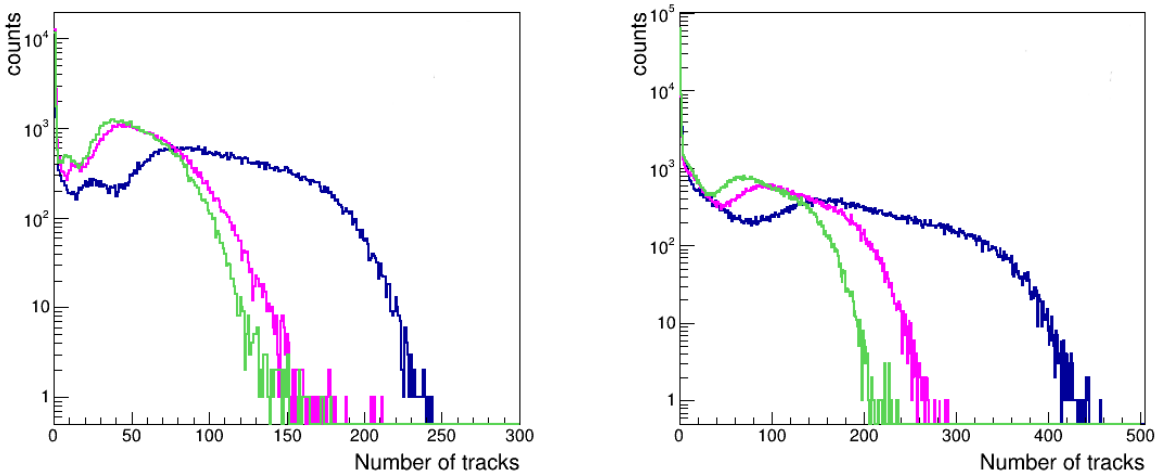

Figure 4.9: Track multiplicities for Xe+La (left pad) and Pb+Pb (right pad) at 150A GeV/c data. Track multiplicity in Jura arm is shown as magenta line, in Saleve – as green line, in both arms – as blue line.

to the same track might appear in different bins of the Hough space histogram. Thus the algorithm is performing the clusterization procedure: combining neighbouring bins into one cluster.

In Fig. 4.9 multiplicities of the reconstructed SAVD tracks are shown for Xe+La and Pb+Pb at 150A GeV/c data. As one can see Pb+Pb as heavier system has higher track multiplicity then Xe+La. Note that no event selection was done on the event of SAVD reconstruction, thus the low track multiplicity region is present on the plots.

Presence of the magnetic field in the SAVD volume allows momentum reconstruction of the SAVD tracks. The following formula was used to calculate track momentum:

$$p_{xz} = \frac{Ze \int B_y dl}{\sin\alpha_1 - \sin\alpha_2},$$

where α_1, α_2 are angles of the track in the first and last stations respectively. Momentum reconstruction is imprecise due to the fact that the magnetic field is weak ($\int B_y dl =$ 0.04 T·m) and obtained value is not used for final analysis. Nevertheless, the reconstructed momentum values are useful for verifying track matching between SAVD-tracks and TPC-tracks.

4.2.3 Track matching

The track multiplicity correlation between tracks reconstructed in SAVD and the TPCs is shown in Fig. 4.10. As one can see the multiplicities of SAVD and TPC tracks are well correlated, which proves, that the tracking procedures described above is correct.

Because of the weak magnetic field in SAVD volume the track momenta determined with SAVD alone are not accurate enough to allow precise extrapolation of SAVD tracks through the magnetic field into the TPC volumes. Also, due to low spacial resolution of the TPC tracks their extrapolation to SAVD volume does not allow for clear one to one association of tracks. To avoid this, the track matching algorithm tries all possible

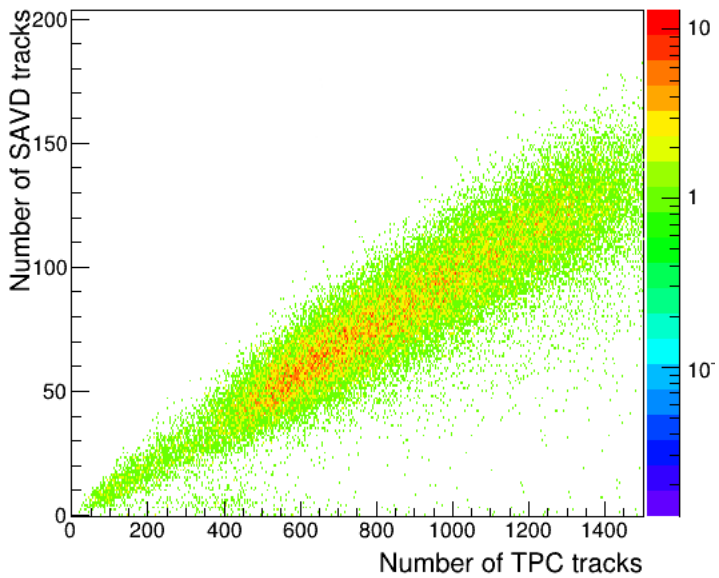

Figure 4.10: VD track multiplicity versus TPC track multiplicity. Plot was done for Xe+La at 150A GeV/c data set.

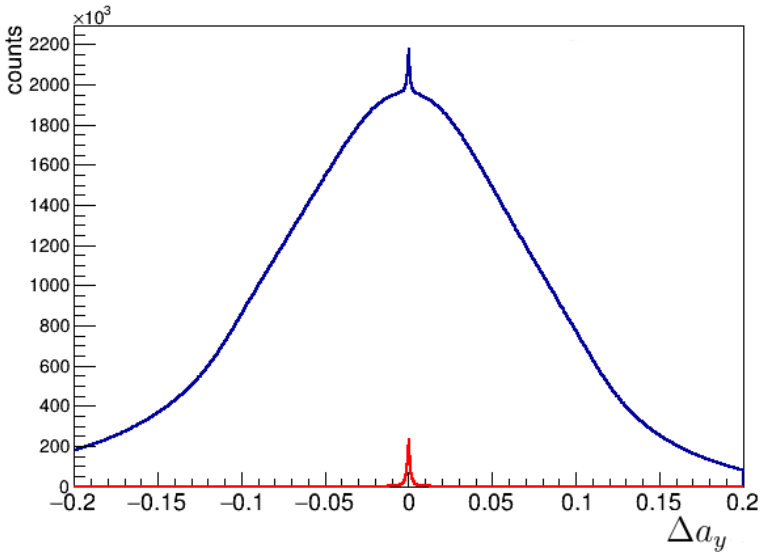

Figure 4.11: The distribution of the difference between SAVD–VTPC track pair slopes in the y coordinate. Blue histogram is plotted for all combinations of tracks, red histogram corresponds to best match of tracks.

combinations of pairs of SAVD with TPC tracks and searches for the best match among all combinations based on the difference in the position and direction of the tracks.

The matching procedure consists of three steps:

- Since tracks are not affected by the magnetic field in the y direction all SAVD tracks are combined with VTPC tracks and for each SAVD–VTPC track pair the difference of the tracks slopes in the y coordinate, Δa_y, is calculated. The distribution of Δa_y shows a sharp peak on a large combinatorial background as shown in Fig. 4.11 (red histogram). A $\pm 5\sigma$ cut around this peak is applied for the pre-selection of SAVD and TPC track pairs that potentially match.

- For a given track pair the TPC momentum is assigned to the SAVD track. This allows to extrapolate the SAVD track to the VTPC front surface where tracks are matched in x, y (z is matched by construction as it defines the matching plane) coordinates and the difference of the track positions Δx and Δy are calculated.

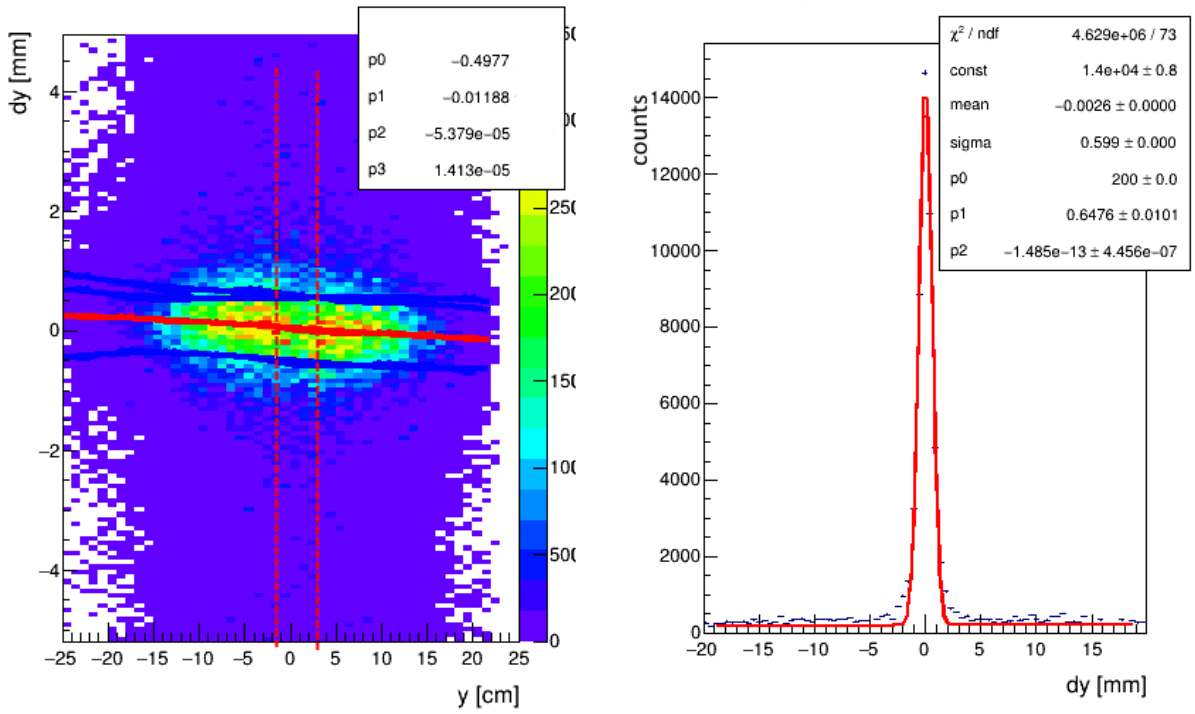

Figure 4.12: Left pad : Difference in y coordinate of SAVD and TPC tracks (Δy) versus y at the matching plane for *Jura* - *Jura* track combination. The histogram is fitted with Gaussian in each y slice and the mean values are marked as red dots. The values were fitted with third order polynomial line (red line on plots). The blue lines are $\pm$ 3σ around the mean values. The parameters of the fit are indicated on the plots. Right pad: example of the projection of distribution of Δy versus y onto the Δy coordinate for $-1.5\text{mm} < y < 3.2$ mm (single slice, shown as interval between dotted lines on right pad). See text for details.

Left panel in Fig. 4.12 shows the distribution of Δy versus y position of tracks from Jura arm of SAVD matched to *Jura* side tracks of VTPC-1. Because the average value of Δy depends on y, narrow ranges of y of the distribution are projected onto Δy. The projected distributions (slices) are then fitted with a sum of a second order polynomial which describes the background related to false matchings and a Gaussian that accounts for the true matchings. An example of a single slice is shown in right panel of Fig. 4.12. The dependence of the fitted mean ($\langle \Delta y \rangle$) and variance ($\sigma_{\Delta y}$) on y are then fitted with a third order polynomial function. The results of these fits are shown as red ($\langle \Delta y \rangle (y)$) and blue lines ($\pm\ \sigma_{\Delta y}(y)$) in left panel of Fig. 4.12. A similar procedure was used for Δx versus z matching. Both, Δy versus y and Δx versus z distributions were constructed for *Jura* - *Jura*, *Jura* - *Saleve*, *Saleve* - *Saleve* and *Saleve* - *Jura* track combinations, separately for VTPC-1 and VPTC-2.

- The values of $\langle \Delta y \rangle$, $\sigma_{\Delta y}$ and $\langle \Delta x \rangle$, $\sigma_{\Delta x}$ obtained from the fits are used to apply elliptic cuts to select the right matchings.

Fig. 4.13 shows the distribution of the difference of SAVD and TPC momentum components Δp_x and Δp_z calculated at the matching plane for SAVD and TPC track com-

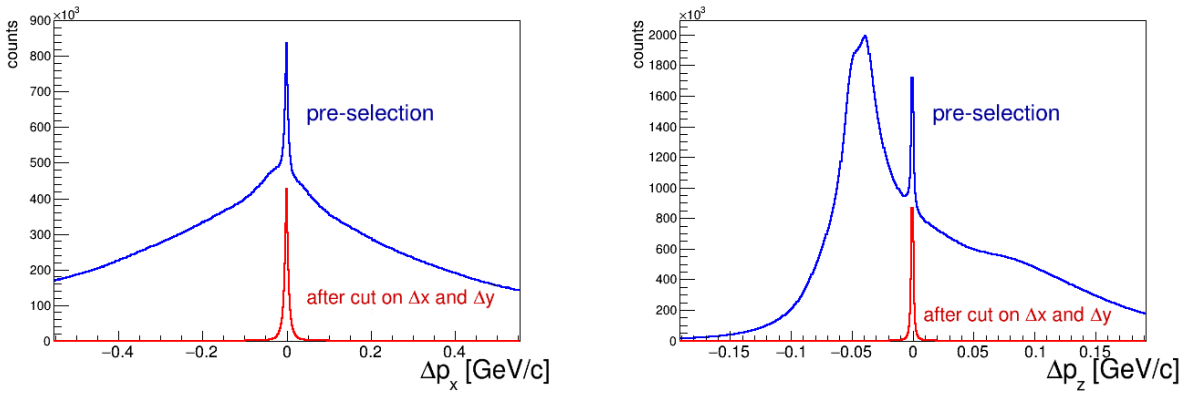

Figure 4.13: Difference of momentum components Δp_x (left pad) and Δp_z (right pad) calculated at the matching plane for SAVD - TPC track combinations that passed the cut on Δa_y (blue) and after additional elliptical 4σ cuts on Δx and Δy (red).

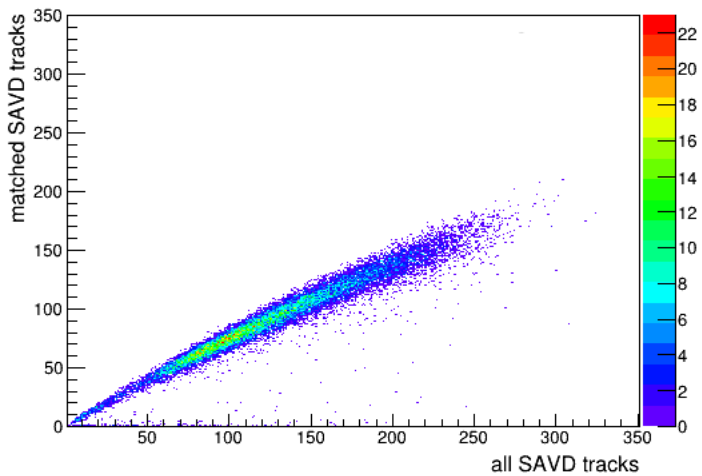

Figure 4.14: Matched SAVD track multiplicity versus SAVD track multiplicity. Plot was done for Xe+La at 150A GeV/c data set.

binations that passed the cut on Δa_y (blue) and with the elliptical 4σ cuts on Δx and Δy (red). After applying the Δx and Δy cuts the distributions are practically free of background.

As it is shown in Fig. 4.14, about 73% of SAVD tracks are matched to TPC tracks. This result corresponds to Geant4 simulations described in Chapter 8. The remaining tracks either miss the VTPC acceptance, or decay before reaching the VTPC.

Finally, the global track which has hits in both SAVD and TPCs is refitted using a Kalman Filter and used for further analysis.

4.2.4 Sensor efficiencies

As was mentioned earlier, the sensor thresholds were tuned for the optimal trade-off between registration efficiency and noise rejection. Sensor efficiencies are determined in the following procedure. For each 3-hit track the position where it is crossing the station, which was not used in construction of the given track is calculated (black points in Fig. 4.15). In case there is a cluster on the station at the crossing point (red points in Fig. 4.15) the 4-hit track can be constructed (3 hits plus the cluster on this station matched to the 3-hit track) and the sensor is considered as being "efficient". Thus the sensor efficiency is calculated as ratio between number of cases when matching cluster

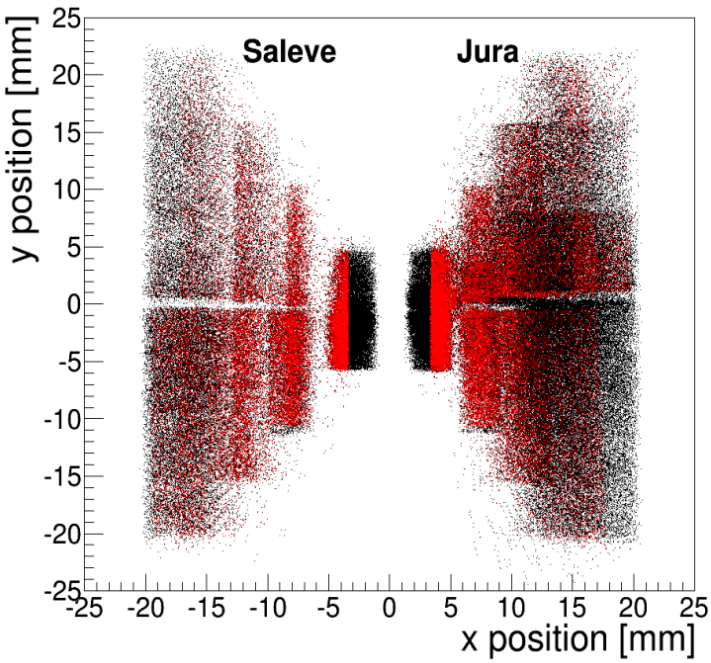

Figure 4.15: Red Points: the positions where 3-hit tracks crossing station which was not used in construction of the given track and which have the cluster near it. Black points: the positions where 3-hit tracks crossing station which was not used in construction of the given track. See text for details. Plot was done for Xe+La at 150A GeV/c data set.

Saleve sensor	efficiency	Jura sensor	efficiency
Vds1_0	0.905	Vds1_0	0.954
Vds2_0	0.950	Vds2_0	0.967
Vds3_0	0.909	Vds3_0	0.949
Vds3_1	0.863	Vds3_1	0.912
Vds4_0	0.970	Vds4_0	0.920
Vds4_1	0.974	Vds4_1	0.957
Vds4_2	0.949	Vds4_2	0.963
Vds4_3	0.925	Vds4_3	0.958

Table 4.1: Sensor efficiencies during the Xe+La at 150A GeV/c data taking. Sensor naming convention is indicated in Fig. 3.5.

Saleve sensor	efficiency	Jura sensor	efficiency
Vds1_0	0.885	Vds1_0	0.996
Vds2_0	0.993	Vds2_0	0.996
Vds3_0	0.903	Vds3_0	0.965
Vds3_1	0.827	Vds3_1	0.900
Vds4_0	0.987	Vds4_0	0.919
Vds4_1	0.985	Vds4_1	0.943
Vds4_2	0.981	Vds4_2	0.974
Vds4_3	0.927	Vds4_3	0.960

Table 4.2: Sensor efficiencies during the Pb+Pb at 150A GeV/c data taking. Sensor naming convention is indicated in Fig. 3.5.

exists (red points) versus all cases (black points).

As one can see from Table 4.2.4 and Table 4.2.4, during data takings (except first pilot data taking) sensor efficiencies were kept well above 85%.

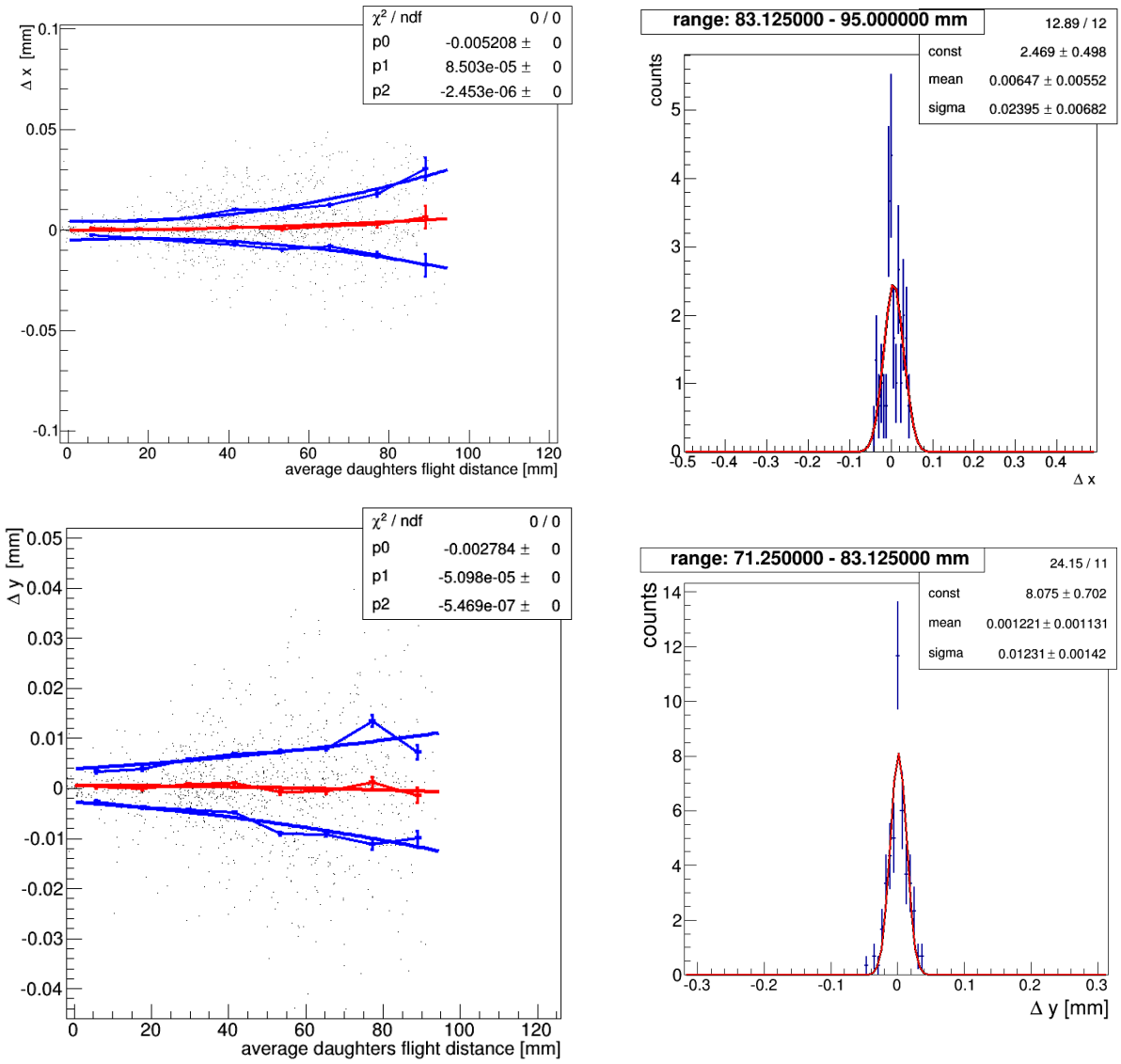

Figure 4.16: Left pads: the distribution of the difference between extrapolated positions of Λ daughter tracks Δx (upper pad) and Δy (bottom pad) versus the distance from the secondary vertex to the first hit of the tracks. Each flight distance slice the distribution is fitted with Gaussian (right pads) and red line indicated mean values of the fit and blue line $\pm 3\sigma$ around the mean value. Right pads: the distributions in the selected slice (which corresponds to largest flight distance) for x and y, the distributions are fitted with Gaussian (red line) and the parameters are indicated on plots.

4.2.5 Secondary vertex resolution

Secondary vertex (x_v, y_v, z_v) is determined as the point at the closest proximity of daughter tracks. To determine the resolution of the secondary vertex the Λ decays to $\pi + p$ channel are considered (details of the Λ reconstruction are described in Chapter 7). The daughter tracks are extrapolated to the plane defined by z_v and the respective transverse coordinates, (x_1, y_1) and (x_2, y_2), are calculated. The sigmas of the difference between secondary vertex and extrapolated positions of daughter tracks $f_1 = x_1 - x_v$ and $f_2 = x_2 - x_v$ (and same for y coordinates) reflect the the single track resolution. The difference between extrapolated positions of daughter tracks $f = f_1 - f_2$ for x component $\Delta x = x_1 - x_2$

and y component $\Delta y = y_1 - y_2$ are shown in Fig. 4.16 (left pads). It was found, that the width of the distributions depends on the average flight distance of the daughters from the secondary vertex to their first hits on Vds1_0 or Vds2_0 sensor (right pads in Fig. 4.16). Thus, to estimate secondary vertex resolution for D mesons, which decay close to the target, the region of the largest flight distance of the daughter tracks was selected. Since $\sigma(f) = \sqrt{2}\sigma(f_{1,2})$, one obtains secondary vertex resolution on the level of 16 μm and 8 μm in x and y, respectively.

Since for primary vertex resolution it was obtained that: $\sigma(z) \approx 8\sigma(x)$ and $\sigma(z) \approx 16\sigma(y)$ (see Fig.4.2.2), one can estimate z secondary vertex resolution assuming the same ratio: $\sigma(z_v) \approx 8\sigma(x_v)$ and $\sigma(z_v) \approx 16\sigma(y_v)$. Thus, secondary vertex resolution in z coordinate is on the level of 100 μm. Note, that it is rough estimation obtained from the data and more precise study (based on simulations) is described in Chapter 8.

Chapter 5

Data Calibration

In order to improve accuracy of the obtained results a calibration procedure was performed. Some of calibration coefficients are connected to detector setting and are constant throughout data taking period such as relative geometrical positions of the detectors. However other coefficients are slowly changing in time, example of such coefficient is electron drift velocity in TPCs.

Data crucial for the study presented in this thesis, was obtained using SAVD and TPCs, therefore the calibrations of these two detectors were performed.

The plots in this chapter are shown for Xe+La at $150A$ GeV/c data however, the procedure and the final distributions both, for Pb+Pb and Xe+La at $150A$ GeV/c are very similar.

5.1 TPC calibration

The software for TPC calibration was developed by the NA61/SHINE Collaboration and is described in details in [67]. The calibration procedure is used to find time offset of the drift time sampled with respect to the time reference of the event, to find the geometrical alignment of TPCs, as well as a drift velocity which is time-dependent. Calibration is realised sequentially for each of these parameters.

In particular, the important stage of the calibration is dedicated to determination of electron drift velocity in each of the TPCs. The drift velocities are measured by dedicated drift velocity monitors it the gas outlet of each of the TPCs. It is ensured to keep the similar conditions of electric field, gas temperature and pressure inside the monitors as it is encountered in the volume of TPCs.

For the accurate global track reconstruction the precision of the drift velocity determination should be of the order of 1 ‰, however, the DCS measurements give less accurate values. For this reason the drift velocities are determined using experimental data.

The procedure starts with the reconstruction of global tracks in TPCs using DCS drift velocity as an input. Then, the reconstructed tracks are dissected into local tracks and are refitted using only clusters in a given chamber. The MTPC-L local tracks are extrapolated to the ToF-L volume, and matched with ToF-L hits. The segmentation of the of ToF-L in the TPC drift velocity direction (y coordinate) allows to verify the positions of the TPC tracks in the y direction.

The procedure is illustrated in Fig. 5.1. The difference between the y coordinate of the extrapolated track, y_{reco}, and the y coordinate of the ToF-L hits, y_{real}, is calculated for each track, and is denoted as Δy.

If y_0 is the vertical shift of MTPC-L, t_0 is the drift time offset, t_{drift} is the measured drift time in MTPCs, $v_{drift,reco}$ is the drift velocity obtained by DCS, and $v_{drift,real}$ is the searched calibrated drift velocity, then y_{reco} and y_{real} can be expressed in the following way:

$$y_{reco} = y_0 - (t_0 - t_{drift}) \cdot v_{drift,reco},$$
$$y_{real} = y_0 - (t_0 - t_{drift}) \cdot v_{drift,real}.$$

It is seen that ratio of Δy and y_{real} is proportional to $(v_{drift,reco} - v_{drift,real})/v_{drift,real}$. Thus the slope of Δy vs y_{real} will reflect value of $v_{drift,real}$.

After obtaining values for MTPC-L, the drift velocities of other chambers are calculated in the same way taking previously calibrated chamber as a reference.

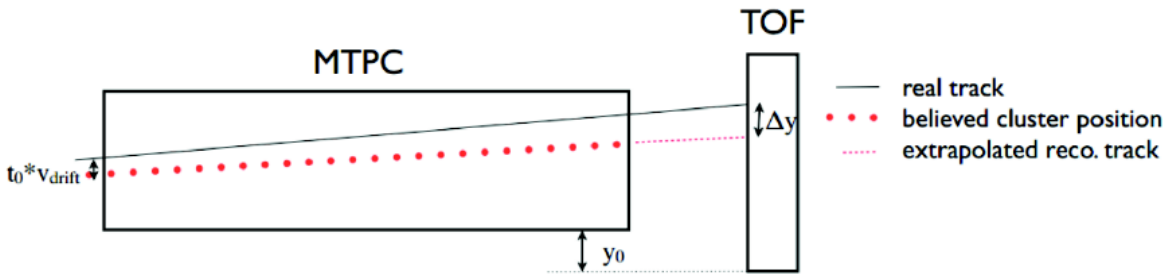

Figure 5.1: Illustration of the principle of the Δy vs y analysis for drift velocity determination [67].

The example of Δy vs y_{real} plots is shown in Fig. 5.2 before the calibration. The calibration procedure searches for t_0, y_0 and $v_{drift,reco}$ parameters to obtain $< \Delta y >= 0$ for for each value of y_{real}. Fig. 5.3 shows Δy vs y_{real} for the calibrated parameters. The fact, that after the calibration Δy no longer depends on y_{real} verifies correctness of the calibration procedure.

Study of the residuals between reconstructed tracks and clusters assigned to them, provides a powerful tool to check if the data is properly calibrated and reconstructed. The so-called residual plots for x and y coordinate are presented in Fig. 5.4. The green colour of the distribution corresponds to mean value of the residuals equal to zero. The regions with colour deviated from green are located at the borders of MTPCs. This is caused by the instabilities in the calibration procedure due to a low track multiplicities in these regions.

5.2 SAVD related calibration

Although survey measurements were done before the beginning of data takings, very precise spacial resolution of SAVD allows to perform fine tuning of geometry based on collected data. Calibration of SAVD includes calibration of sensor and arm positions and position of the whole device in NA61/SHINE global coordinate system. Also, it includes calibration of the parameters used in the tracking procedure, namely cuts applied in combinatorial tracking and parameters for tracking procedure using Hough Transform approach as well as the parameters used in the SAVD-TPC track matching algorithm.

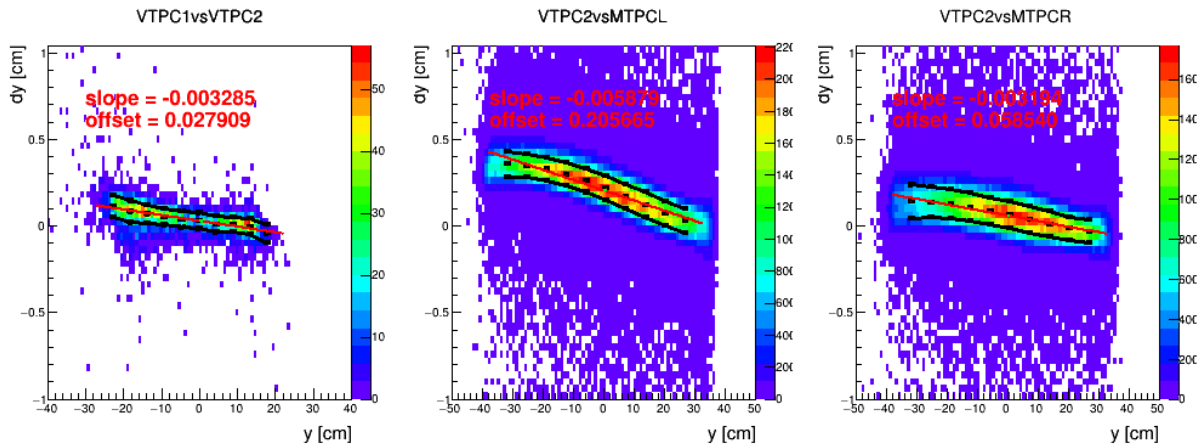

Figure 5.2: The example Δy vs y_{real} plot for single run taken for Xe+La at 150A GeV/c. Drift velocity is calculated using DCS measurements. The histogram was fitted with Gaussian in each y slice and the mean values are marked as black dots. The black lines are $\pm$ 3σ around the mean values. The black dots were fitted with straight line (red line on plots). The parameters of the fit are indicated on plots.

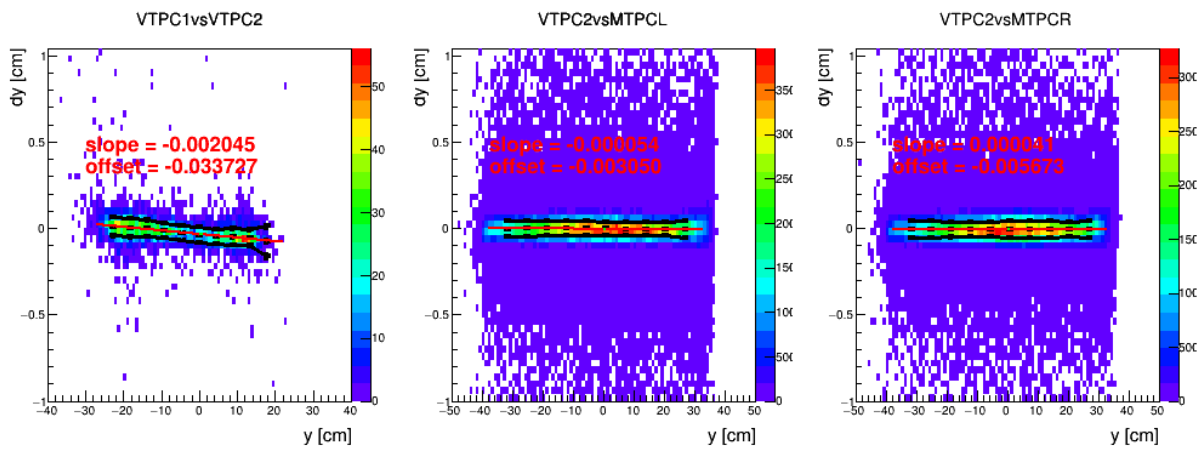

Figure 5.3: The example Δy vs y_{real} plot for single run in Xe+La at 150A GeV/c data. Drift velocity is calculated using the described above calibration procedure. The histogram was fitted with Gaussian in each y slice and the mean values are marked as black dots. The black lines are $\pm$ 3σ around the mean values. The black dots were fitted with straight line (red line on plots). The parameters of the fit are indicated on plots.

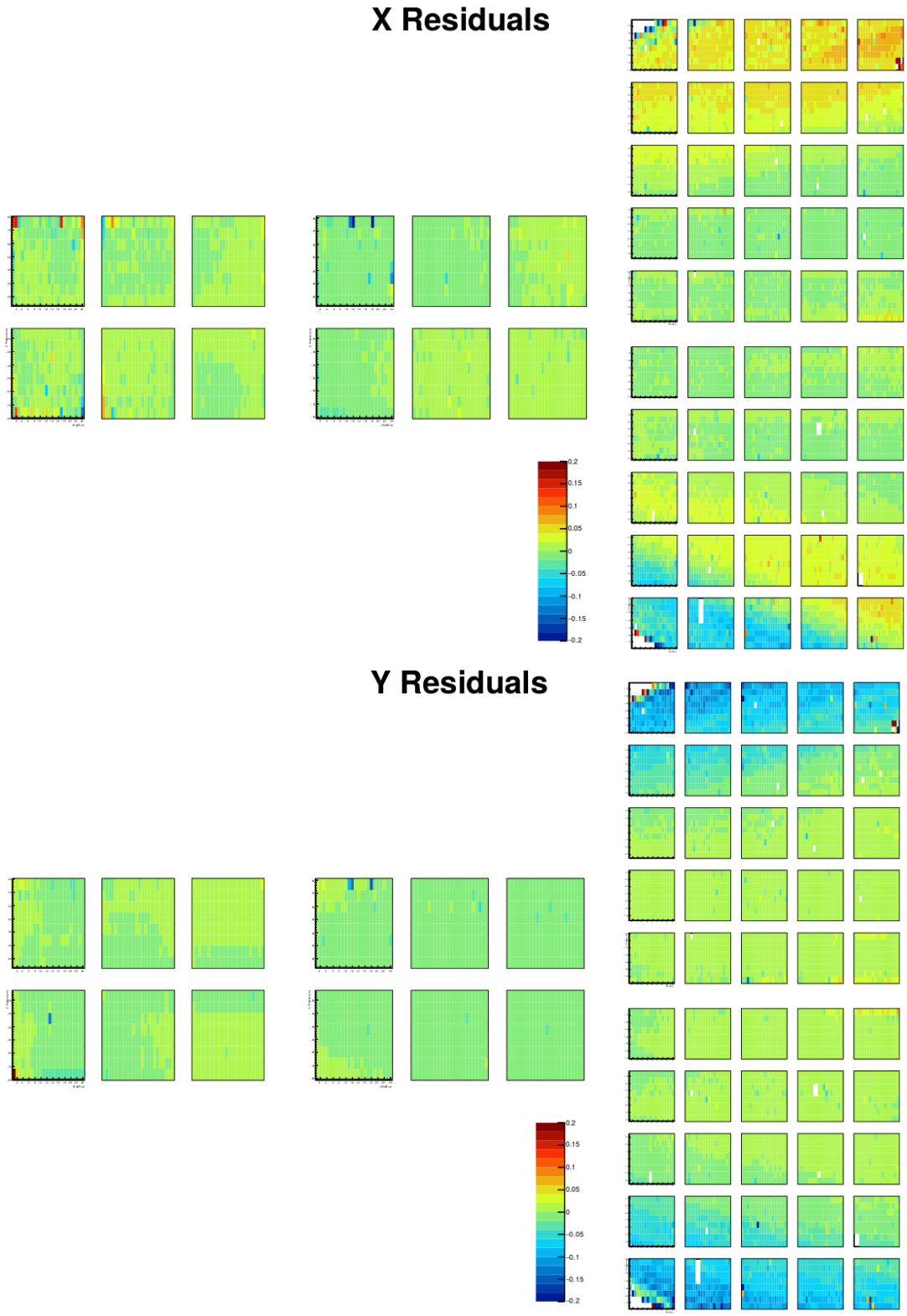

Figure 5.4: The residuals plots for x (top pad) and y (bottom pad). The binning of the plots corresponds to the size of the TPC pads.

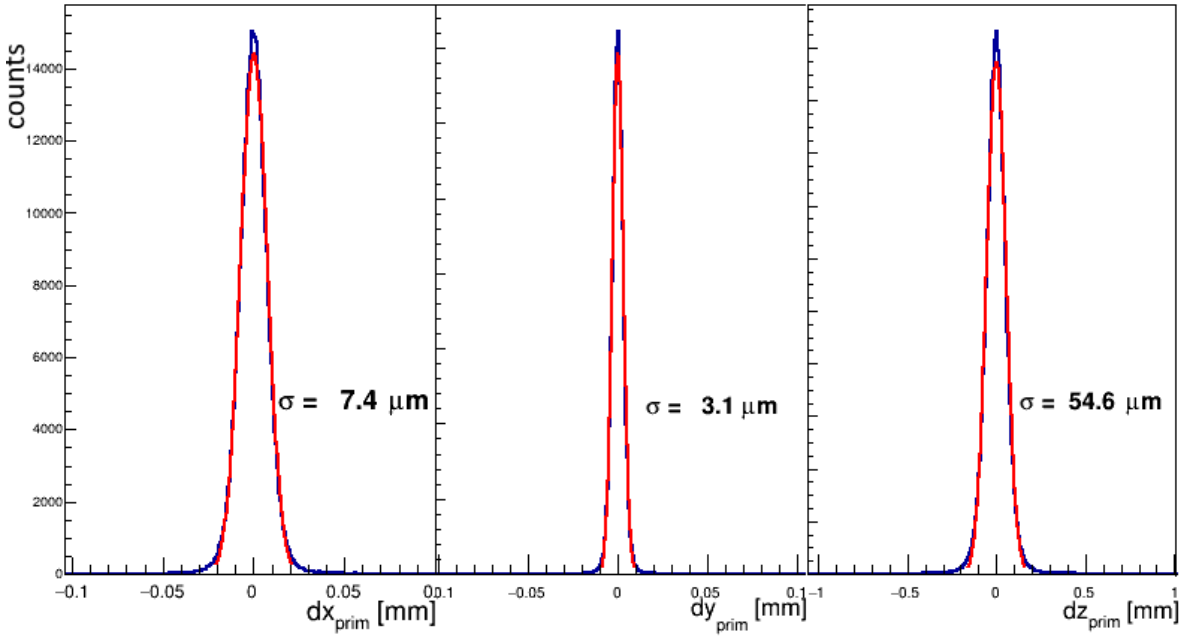

Figure 5.5: The distribution of difference between reconstructed vertex in Jura and Saleve arms dx_{prim}, dy_{prim} and dz_{prim}. The red lines represent Gaussian fit, the sigma value of the fit are indicated on plots.

Sensor geometry calibration

As first step of SAVD corrections for the sensor positions and rotation angles have to be found. The alignment of sensors was done for Xe+La data taken with the magnetic field turned off. This was not done within this PhD project. More details could be found in [68, 69].

In case of correct geometry hits produced by the same particle should lie on a straight line (assuming that magnetic field is off). Considering three hit track the deviation in x and y direction of the middle hit from the line connecting first and third hits was introduced. The alignment algorithm based on MINUIT package [70] searches for optimal parameters of position and rotations angles of sensors in order to minimise the deviations.

Relative arm position calibration

The horizontal movement was used to set the optimal horizontal position of arms, which means that, on one hand, detector will be registering more tracks and, on the other hand, sensors will be not illuminated by the beam halo (to reduce radiation damage of sensors). Typicaly the gap between the edges of the inter-most sensors was kept on the level of ±3 mm. During the production measurements the currents on the dedicated dipole magnets of the beam line were tuned once per day to keep the horizontal and vertical positions of beam spot on target unchanged.

To preform calibration of rotations of the arms relative to the beam, no target data was collected with arms located in such a way, so that the beam passes through one of the arms. The example of the distribution of the fired pixels of the sensor on the first station is shown in Fig. 5.2. The most illuminated area corresponds to the pixels fired by

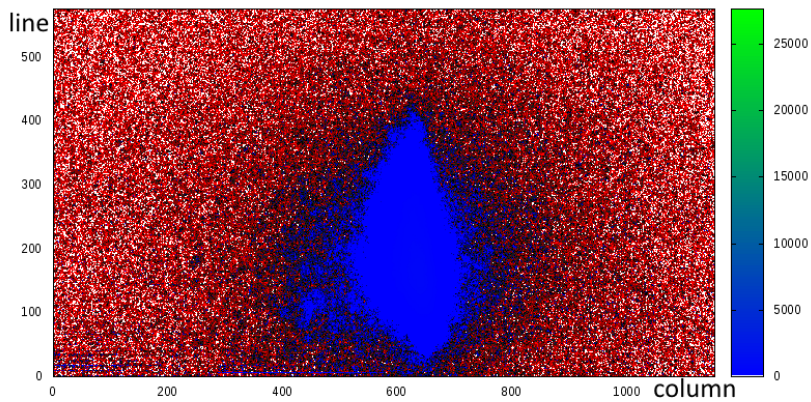

Figure 5.6: The distribution of fired pixels on the first sensor of Jura arm during Xe+La data taking. The most illuminated area (blue) corresponds to the pixels fired by beam particles.

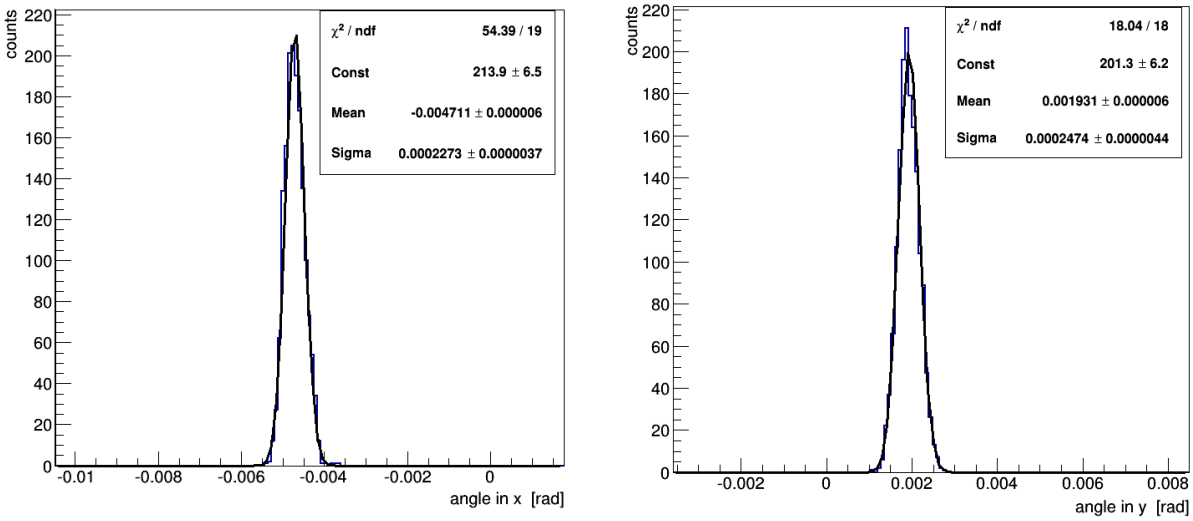

Figure 5.7: The x (left pad) and y (right pad) angle distribution of reconstructed beam tracks (see details in the text). The distributions are fitted with Gaussian (black line) and the parameters are indicated on plots.

beam particles. Such particles usually fire of about 200 pixels and pass almost with strait line though SAVD. The angle distributions (in x and y directions in rexpect to z axis) of these tracks (see Chapter 4) are shown in Fig. 5.7. The obtained fit parameters allow to determine rotation of arms in respect to beam direction with precision of 6 μrad.

Independent reconstruction of the primary vertices using Jura and Saleve arms allows to find the relative position of the arms. The distributions of difference between the positions of the Jura and Saleve vertices in x, y and z were fitted with Gaussian as shown in Fig. 5.5. The obtained mean value of the fit is used to correct arm positions.

SAVD position calibration relative to TPCs

The correlation between positions of the vertex reconstructed using SAVD tracks and the vertex reconstructed using TPC tracks is shown in Fig. 5.2. The correlation in z had three regions due to segmented target structure of target visible in the z coorginate provided by the SAVD device.

Fine tuning of the position of SAVD relative to the TPCs is done by observing the distribution of difference between the positions of vertices in x, y and z. The distributions were fitted with Gaussian as shown in Fig. 5.9. The obtained mean value, of the fit are

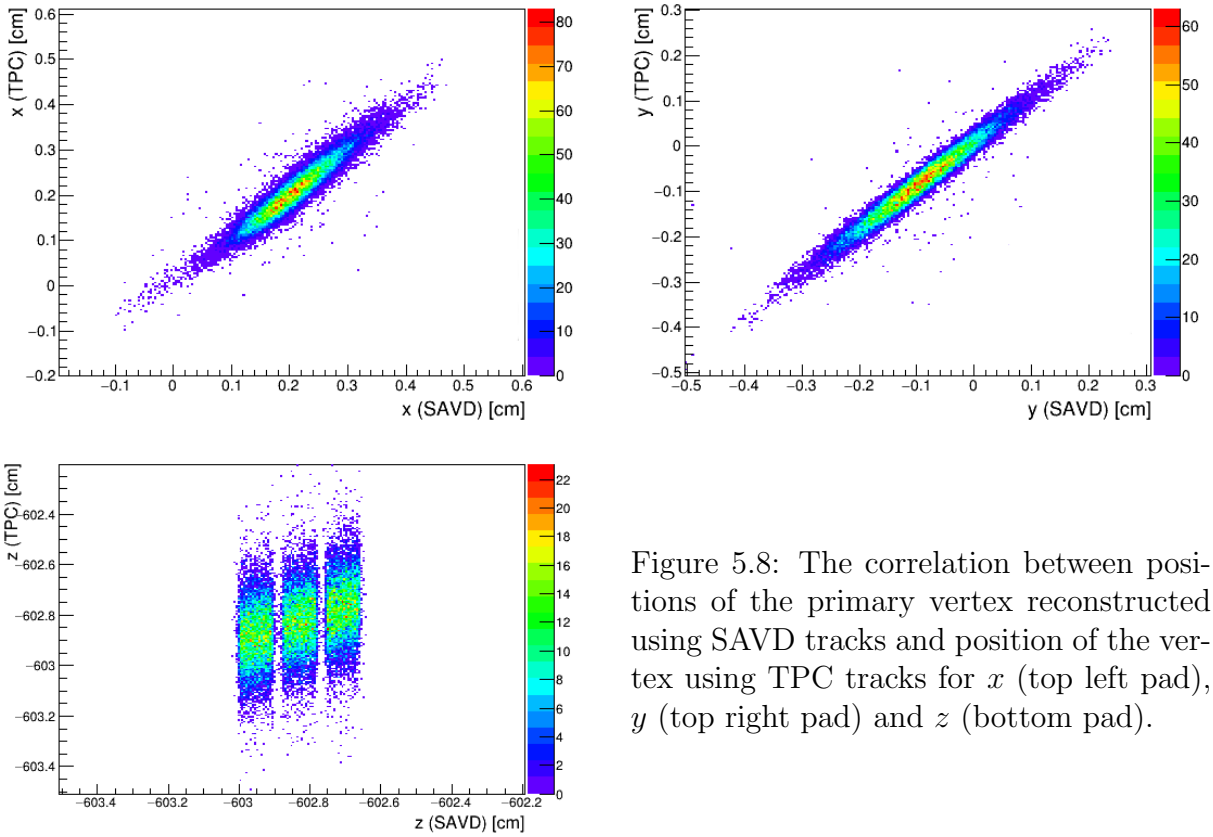

Figure 5.8: The correlation between positions of the primary vertex reconstructed using SAVD tracks and position of the vertex using TPC tracks for x (top left pad), y (top right pad) and z (bottom pad).

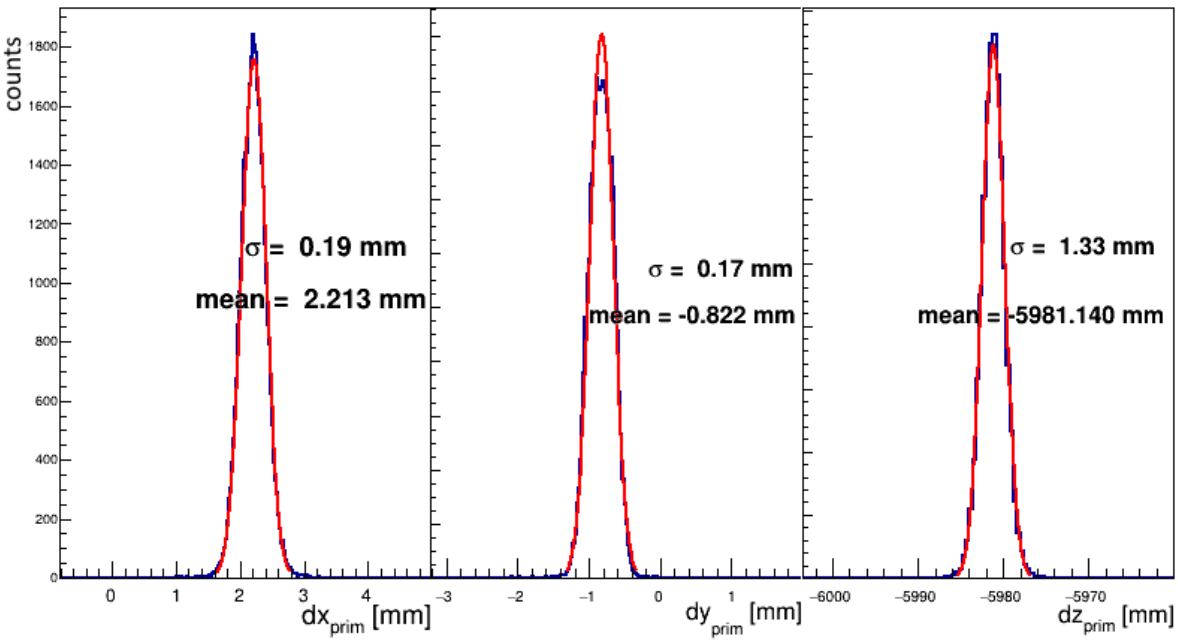

Figure 5.9: The distribution of difference between reconstructed vertex using SAVD tracks and TPC tracks for x, y and z coordinates. The red lines represent Gaussian fit, the sigma and mean values of the fit are indicated on plots.

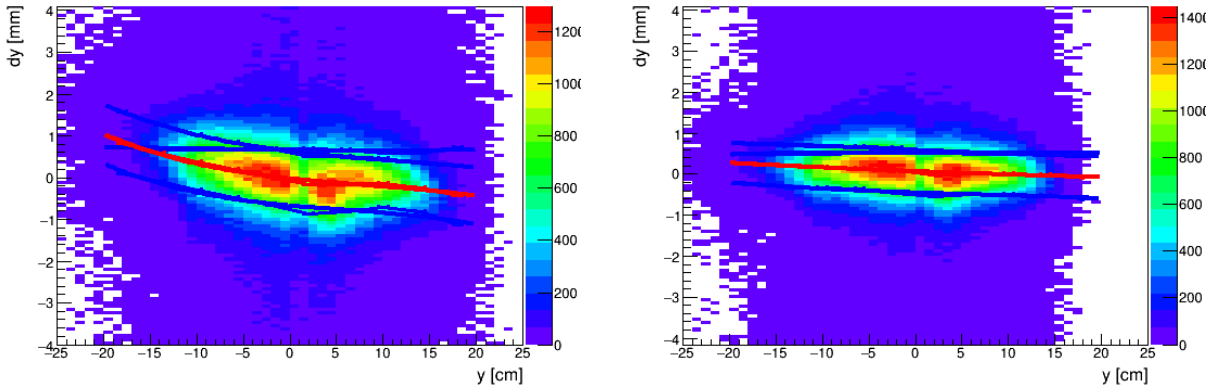

Figure 5.10: Difference in y coordinate of tracks from Jura arm of SAVD and Jura part of VTPC-1 (Δy) versus y at the matching plane before drift velocity calibration (left pad) and after (right pad). The histograms were fitted with Gaussian in each y slice and the mean values are marked as red dots. The values were fitted with third order polynomial line (red line). The blue lines are $\pm$ 3σ around the mean values.

used to correct the SAVD position with an accuracy about 10 μm in x, y and 70 μm in the z coordinate.

SAVD-TPC track matching calibration

According to the procedure described in Chapter 4, for SAVD-TPC track matching the values of $\langle \Delta y \rangle$, $\sigma_{\Delta y}$ and $\langle \Delta x \rangle$, $\sigma_{\Delta x}$ should be obtained. For this both Δy versus y and Δx versus z distributions are constructed for *Jura* - *Jura*, *Jura* - *Saleve*, *Saleve* - *Saleve* and *Saleve* - *Jura* track combinations, separately for VTPC-1 and VPTC-2. These distributions are fitted and values from the fits are used to apply cuts to select the right matchings.

Although performed calibration of the TPC drift velocity improved the distributions (see Fig. 5.10), the distributions are still not strictly horizontal, i.e. the cut value is slightly depends on position of the track. Also, fluctuations exist from run to run, and to compensate this cuts were obtained for not whole data taking but for several time periods.

Chapter 6

Characteristics and selection of the analysed data

6.1 Collected data

The data on Xe+La and Pb+Pb interactions were collected at the top SPS energy in 2017 and 2018 respectively with the NA61/SHINE detector. The data taking periods and statistics of the collected events are listed in Table 6.1.

The data were collected within so-called runs. A run lasts from several minutes (if the data acquisition system stops unexpectedly due to hardware or software faults) to several hours. The long-lasting runs contain up to few 100k events. Runs were taken with target inserted (target IN) and removed (target OUT) alternately. Only target IN runs are of the interest of the analysis.

6.2 Triggers

The on-line triggering system used during heavy-ion data taking was set to register four classes of events defined as described below:

- T3 (halo trigger) S1 $\times$ $\overline{S2}$;
- T1 (beam trigger) S1 $\times$ S2 $\times$ $\overline{V1}$;
- T4 (interaction trigger) S1 $\times$ S2 $\times$ $\overline{S3}$ $\times$ $\overline{V1}$;
- T2 (central trigger) S1 $\times$ S2 $\times$ $\overline{S3}$ $\times$ $\overline{V1}$ $\times$ PSD;

Reaction	data taking period	all collected events	verified events
Xe+La at 150A GeV/c	26.10.2017 - 05.11.2017	3.79M	1.86M
Pb+Pb at 150A GeV/c	16.11.2018 - 02.12.2018	2.99M	1.00M

Table 6.1: Information about the collected data analysed within this thesis. The statistics is presented for all collected physics data and after selection of the events presented in this Chapter.

where for example S1 denotes requirement of the signal from the S1 counter and $\overline{V1}$ denotes requirement of the absence of the signal from the V1 detector.

Unfortunately, during Pb+Pb at 150A GeV/c data the triggers were not set properly and information about triggers saved in the events is wrong (but the events themselves are good and uncorrupted). Likely, it is possible to recover information about trigger selection by applying cuts. Also, short unbiased data set for T1 and T4 triggers was taken, which allowed centrality selection (see below).

6.3 Event selection

The collected data was verified in various ways in order to reject runs of bad or uncertain quality. Most of the event selection criteria (cuts) were similar to other analysis performed for the NA61/SHINE data, however, the values of these cuts were adjusted for a given data set.

Event selection criteria are divided into two groups: the upstream cuts (those that use information from the detectors located upstream from the target) and the downstream cuts (based on information delivered by detectors positioned after the target).

6.3.1 Upstream cuts

Waveform analyser (WFA)

Due to a bunched time structure of the beam there is a possibility of two or more beam particle interacting on target within a short time interval leading to registration of the so called pile-up events. Such particles coming in a ± 25 μs time window (the TPC data collection time) in respect to time instant of the generated event trigger are called off-time particles.

To limit the possibility of events with such particles the timing for two signals is stored sing a waveform analyser (WFA). To reject the pile-up events the cut on the WFA time is applied, namely, the event is rejected if it contains at least one off-time particle within $\pm 25\mu$s interval. Fig. 6.1 shows the time structure of the inelastic events (signal from T4) before and after applied cut.

S1 and S2 signals

S1 and S2 counters deliver also information on the charge deposed in the these detectors by the beam particles. Using this information one can analyse the beam composition. As shown in Fig. 6.2 the distributions for S1 and S2 have single peak corresponding to the Xe beam particles which is typical for the primary beams, therefore no cut is needed. It is worth to note that, when the beam was composed of secondary particles the charge signal delivered bu S1 and S2 can be used to select the given particle species.

BPD

Supplementary information, that allows to verify charge of the beam ions is delivered by the BPD-3 counter. Fig. 6.3 shows the distributions of the charge signal obtained on x and y planes of BPD-3. To reject the events with possibly wrong beam ion the $\pm 4\sigma$ cut was applied, where mean and σ values based on fits with Gaussian function shown in the figure in red colour.

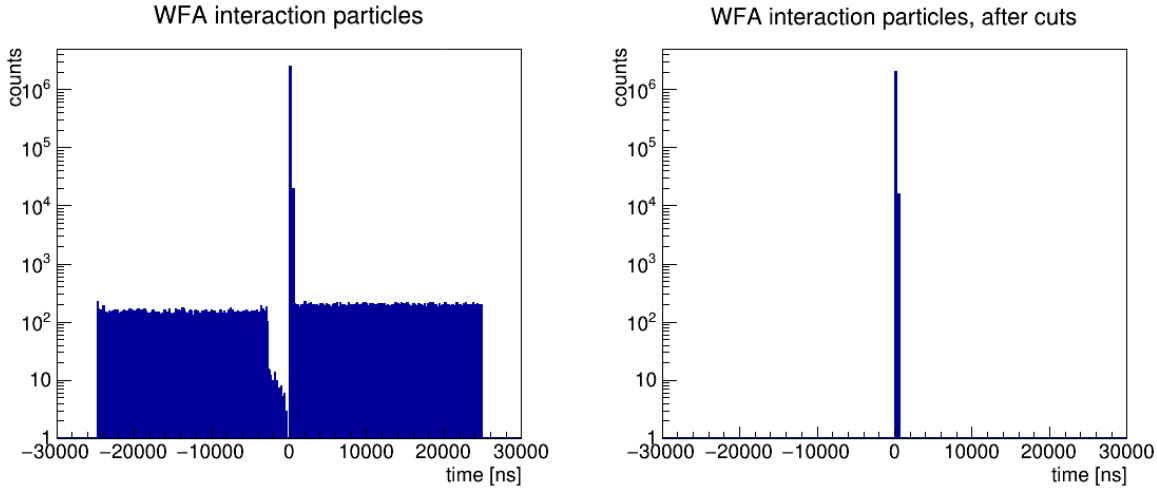

Figure 6.1: The time distribution of the beam particles measured within the T4 with respect to the trigger particle before (left pad) and after (right pad) the applied WFA T4 cut. The peak at $time = 0$ μs corresponds to the trigger particle. The rest of the distribution corresponds to the off-time beam particles. The minimum at $-2 < time < 0$ μs corresponds to the hardware mechanism disabling the trigger for 2 μs after each non-interacting beam particle. The other small maxima are related to the beam time stricture in the SPS. The distribution is plotted for Xe+La at 150A GeV/c data.

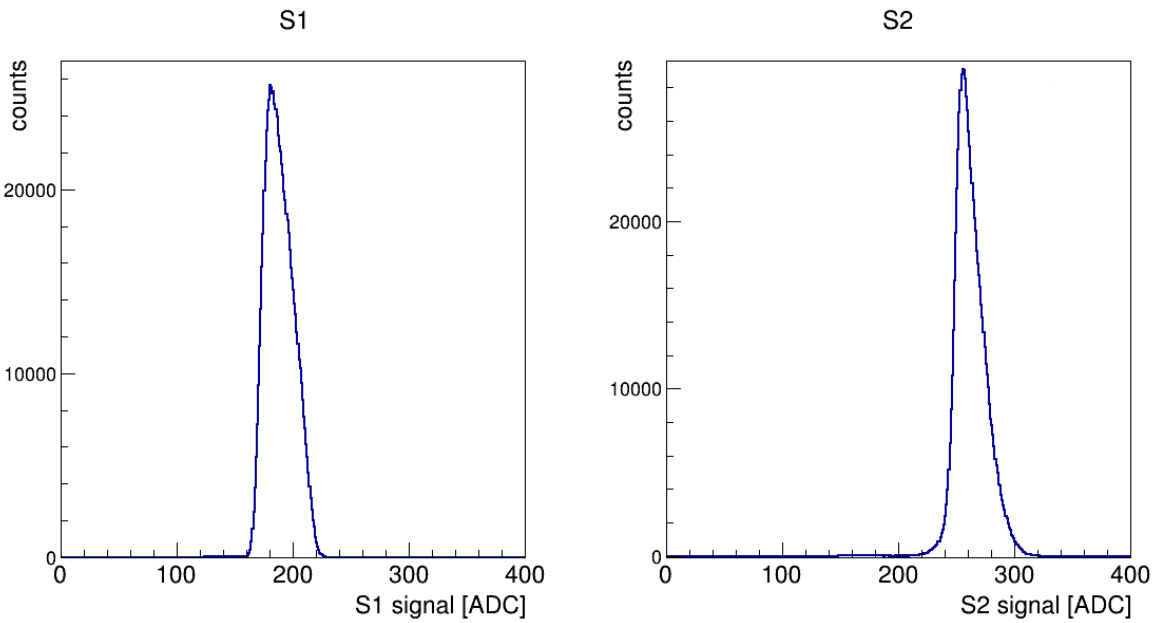

Figure 6.2: The distributions of the signal from S1 (left pad) and S2 (right pad) counters which is proportional to squared charge of the beam particles. The distribution is plotted for Xe+La at 150A GeV/c data.

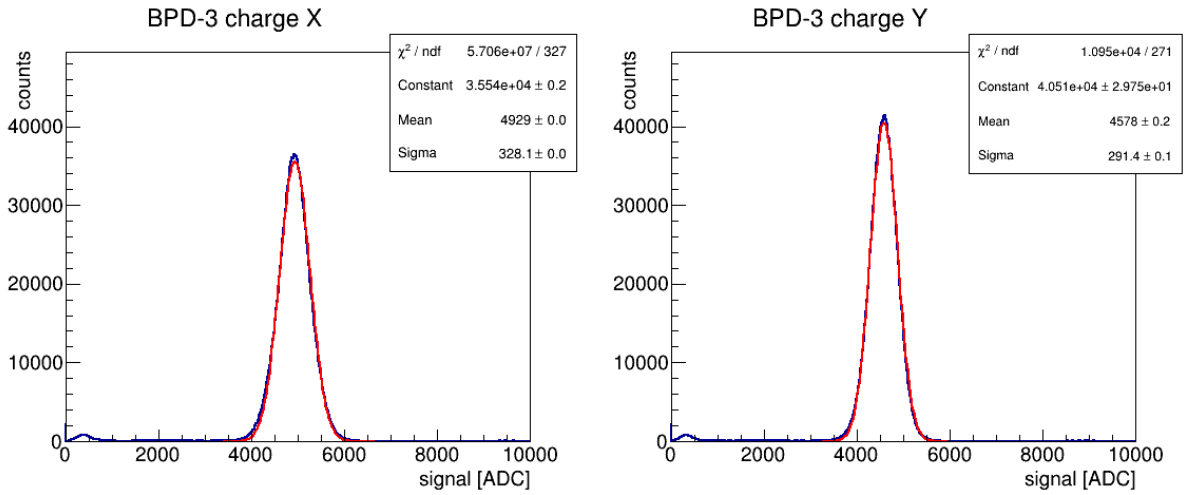

Figure 6.3: The distributions of the obtained charge signal from BPD-3 in x (left pad) and y (right pad). Red line corresponds to Gaussian fit. The distribution is plotted for Xe+La at 150A GeV/c data.

To ensure that the accepted event has well defined beam trajectory a cut on the beam position measured by three BPDs was studied.

A good fit of the beam particle position is required to assure the right calculation of the x and y positions of the primary vertex delivered within standard reconstruction procedure (see Chapter 4). It was found that with the requirement of successful primary SAVD vertex reconstruction, most of events with not properly measured positions in the BPD detectors are rejected. Thus, the specific cut on the x and y positions of the beam delivered by BPDs was not used.

The event is accepted if it has correct signals in both x and y planes of BPD-3 (the closest one to the target) and at least one x and y plane measured by any other BPDs. No cut on x and y values was applied. Fig. 6.4 presents the beam particle position distributions registered by BPDs before and after the applied cut, and without the applied cut but with the requirement of the reconstructed SAVD vertex.

6.3.2 Downstream cuts

S3 signal

To remove elastic interactions the signal delivered by S3 counter proportional to squared charge of the particles is used. Thus, by applying selection based on the vetoed S3 signal such events can be rejected. As indicated above the S3 signal is included in T4 (interaction) and T2 (central) triggers. The deposited charge distributions of the signal from S3 counter for Xe+La data at 150A GeV/c are shown in Fig. 6.3.2. One can see a double peak structure - the peak located at higher values of ADC corresponds to beam ions thus is assigned to the elastic interactions. The remaining part of the distribution, at lower values of ADC, is associated with the inelastic interactions. On the same plots the distributions of the same quantity are plotted (red line in Fig. 6.3.2) applying the selection of the events with the reconstructed SAVD vertex. It is seen from the plot, that the requirement of the reconstructed SAVD vertex selects the inelastic interaction events. Thus, no additional cut on S3 signal was applied in the analysis presented in this thesis.

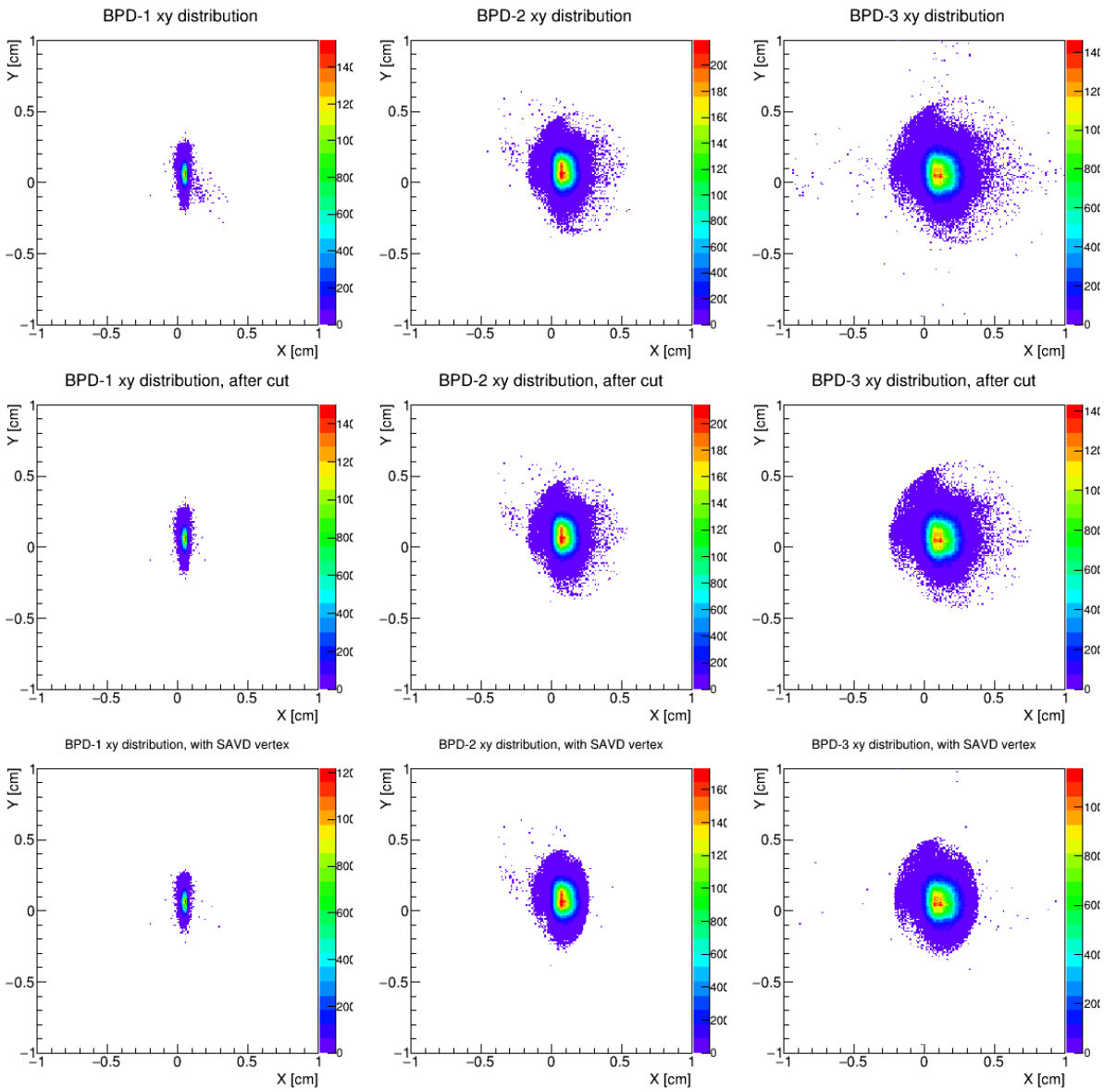

Figure 6.4: The beam particle position distributions registered by the BPDs before the applied cut (top pads), after (middle pads) and without the applied cut but with the reconstructed SAVD vertex (bottom pads). The distribution is plotted for Xe+La at $150A$ GeV/c data.

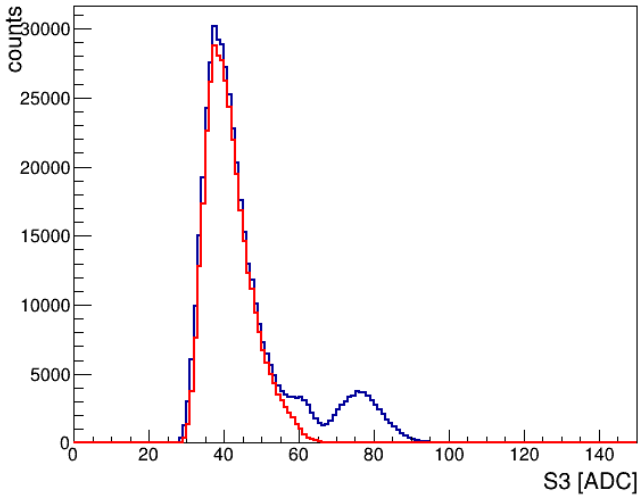

Figure 6.5: Deposited charge distributions of the signal from S3 counter. The blue line corresponds to all events, the red line corresponds to events with the reconstructed SAVD vertex. The distribution is plotted for Xe+La at 150A GeV/c data.

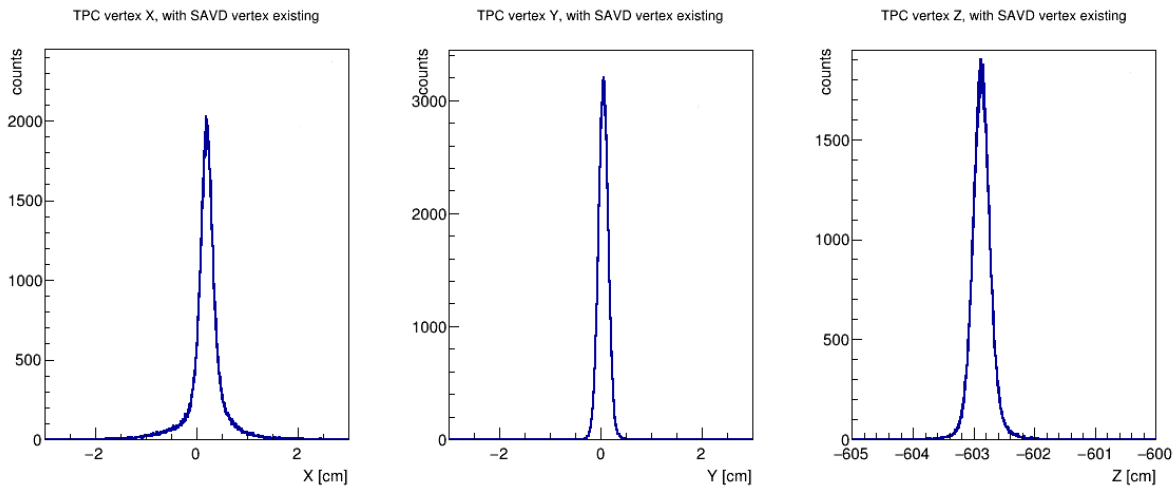

Figure 6.6: The distributions of the x, y, z coordinates of the TPC primary vertex with the applied cut rejecting events without reconstructed SAVD vertex. The distribution is plotted for Xe+La at 150A GeV/c data.

TPC primary vertex

The reconstruction software tries to fit tracks reconstructed within TPCs to the common interaction point placed along the beam track extrapolated from the BPD measurements (see Chapter 4). The vertex positions reconstructed by TPC can be studied in order to ensure interaction happening inside the target and not on BPD-3, mylar windows, target holder, etc. Fig. 6.6 presents the reconstructed x, y, z coordinates of the TPC primary vertex with the requirement that the SAVD vertex was reconstructed within the event. It is seen that events with the TPC primary vertex outside target are rejected, therefore no additional cut was applied.

Also, as seen from Fig. 6.7 no additional cuts on position of the SAVD vertex is needed. Note, that the distributions in Fig. 6.6 and Fig. 6.7 are plotted with in the same range.

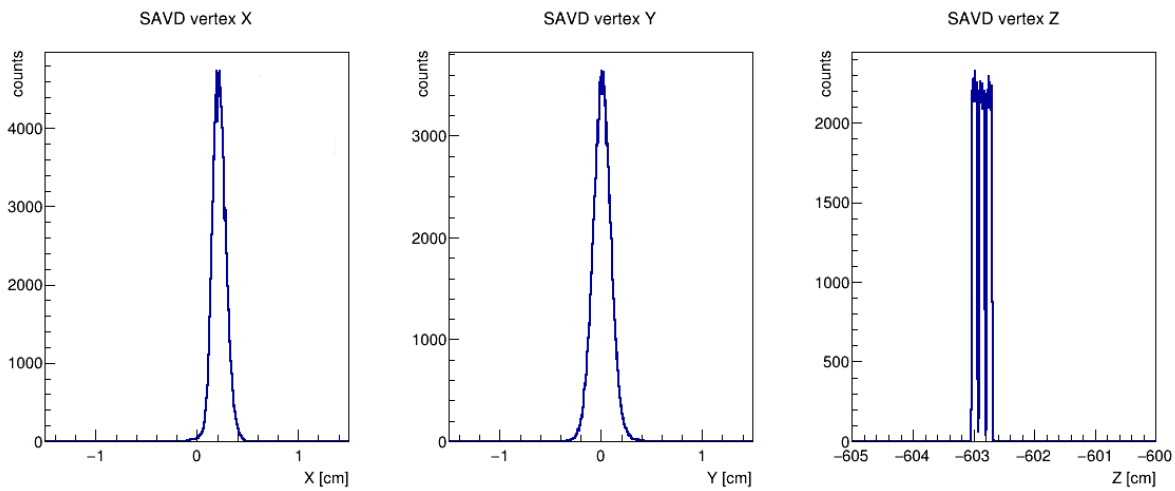

Figure 6.7: The distributions of the x, y, z coordinates of primary vertex reconstructed in the SAVD detector. The distribution is plotted for Xe+La at 150A GeV/c data.

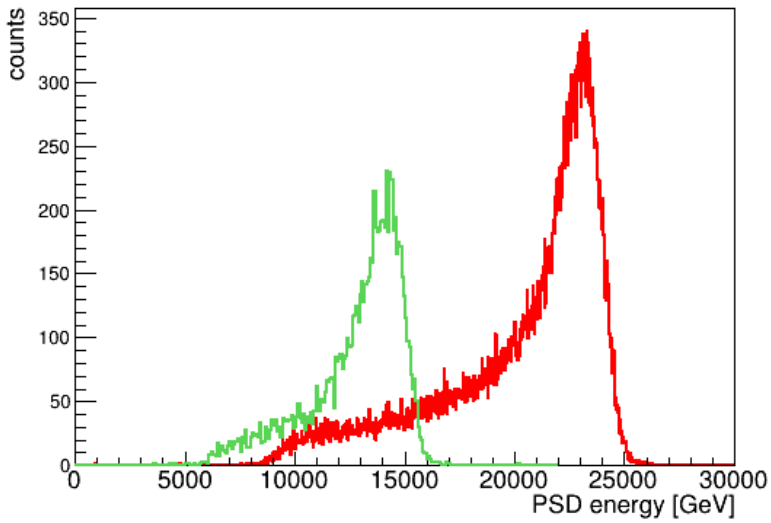

Figure 6.8: The energy deposit in the PSD detector for T4 events. The distribution is plotted for Xe+La at 150A GeV/c collisions (green line) and for Pb+Pb at 150A GeV/c (red line).

PSD

PSD delivers information on the energy deposited by the projectile spectator as well as the hadrons produced in the collision, which reach the calorimeter. During data taking the integrated ADC signal from the calorimeter roughly estimating the collision centrality was included in the trigger logic. However, for more precise centrality determination of the collision an additional off-line analysis was performed.

The actual centrality determination required a dedicated analysis based on minimum bias data (T1 trigger events) as well as the simulation study of such events to verify quantities and also choose the set of the PSD modules to be used for centrality determination (the energy deposit in some of the modules can be dominated not by the collision spec-

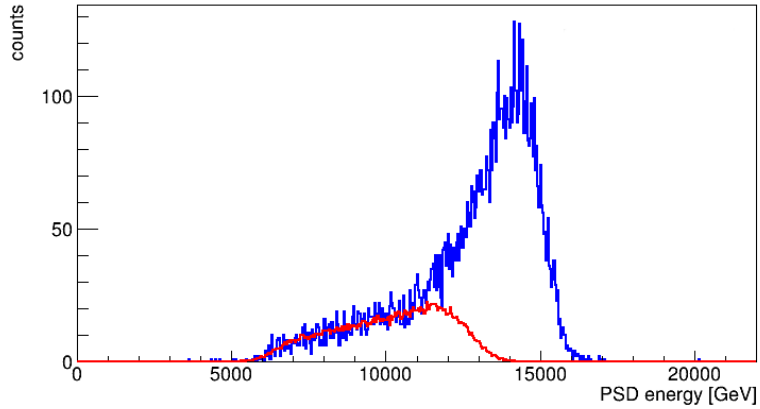

Figure 6.9: The energy deposit in the PSD detector for normalised T4 and T2 events. The blue line is for T4 events and red line for T2 events. The distribution is plotted for Xe+La at 150A GeV/c data.

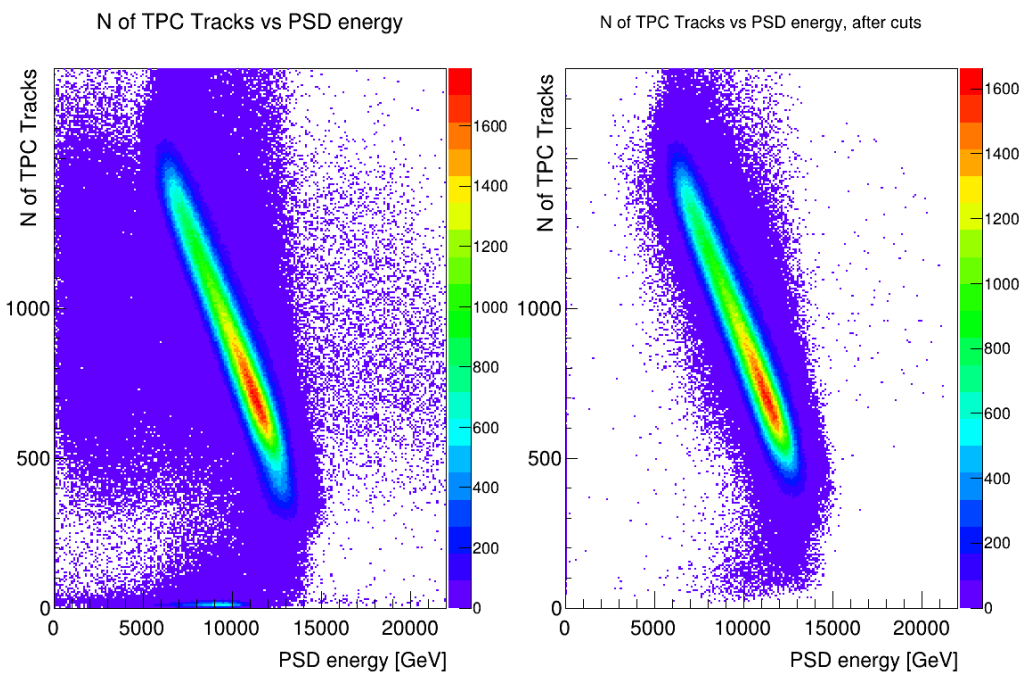

Figure 6.10: The correlation between the energy deposit in PSD and TPC track multiplicity before (left pad) and after (right pad) the PSD cuts. The distribution is plotted for Xe+La at 150A GeV/c data.

tators but by the particles produced in the collision). Unfortunately, the PSD simulation procedure for heavy-ion collisions was not developed by the NA61/SHINE and moreover simulation including PSD of large statistics of minimum bias events would take significant amount of time.

Thus, the following simplified procedure for selection of 0–20% central events was done. Firstly, the PSD modules which were not properly functioning were discarded (so-called PSD status cut) since they might influence the deposited energy calculation. Then for the unbiased T4 (interaction) trigger events the distribution of the deposited energy

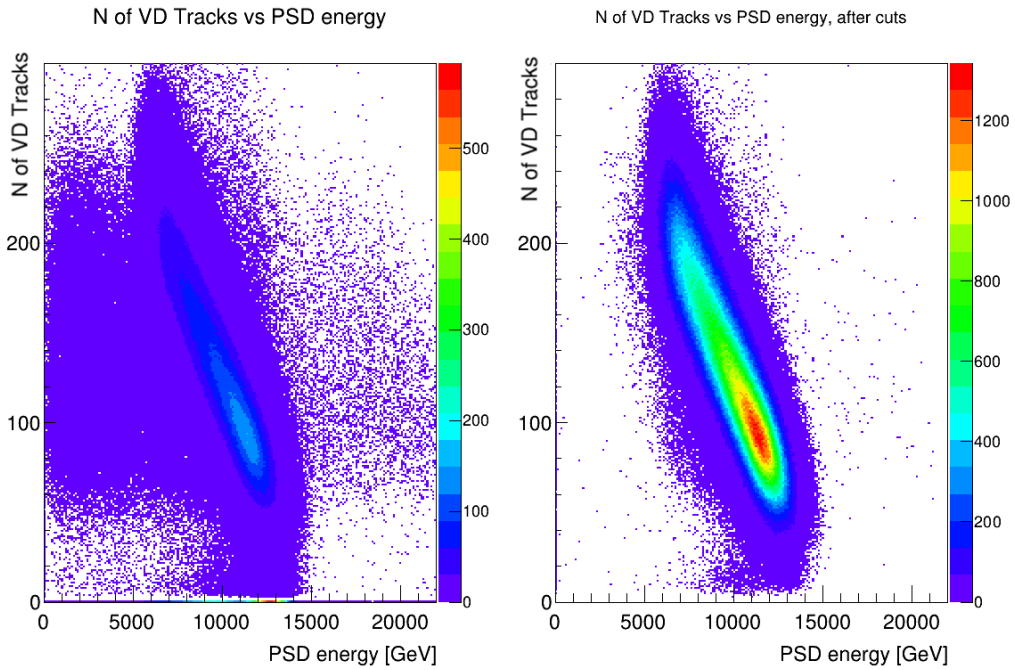

Figure 6.11: The correlation between the energy deposit in PSD and SAVD track multiplicity before (left pad) and after (right pad) the PSD cuts. The distribution is plotted for Xe+La at 150A GeV/c data.

in PSD is plotted in Fig. 6.8. The cut value on the PSD energy was selected as value corresponding to 20% of the integral over PSD energy. For the Xe+La the cut value was found to be 11500 GeV and for Pb+Pb is 17500 GeV. For Xe+La data set (for Pb+Pb data this information can't be recovered) it was found that the T2 trigger actually selects about 0–25% of central events. The PSD energy distribution for T2 and T4 trigger events are shown in Fig. 6.9.

The correlation between the energy deposit measured by the PSD detector and the track multiplicity of the particles registered in TPC (Fig. 6.10) and in SAVD (Fig. 6.11) after applied selection based on PSD is clearly seen which verifies the performed procedure.

6.4 Final statistics of collected events

The numbers of the events selected for the analysis are shown in Table 6.4 for Xe+La at 150A GeV/c data and in Table 6.4 for Pb+Pb at 150A GeV/c data. Tables also present the statistics after consecutive selection criteria described in this chapter.

Cut	% of all events after cut	number of events after cut
no cut	100%	3.79M
T2 trigger	79.2%	3.0M
WFA cut	71.7%	2.72M
BPD-3 charge cut	70.2%	2.66M
BPD position cut	70.2%	2.66M
SAVD vertex cut	66.3%	2.51M
PSD cut	65.0%	2.46M
PSD centrality cut	49.0%	1.86M

Table 6.2: Information about the impact of the applied cuts on collected data for Xe+La at $150A$ GeV/c.

Cut	% of all events after cut	number of events after cut
no cut	100%	2.99M
WFA cut	92.2%	2.75M
BPD-3 charge cut	76.7%	2.29M
BPD position cut	76.7%	2.29M
SAVD vertex cut	55.6%	1.66M
PSD cut	53.1%	1.59M
PSD centrality cut	33.4%	1.00M

Table 6.3: Information about the impact of the applied cuts on collected data for Pb+Pb at $150A$ GeV/c.

Chapter 7

Results

The goal of the analysis is to obtain the direct signal of $D^0 + \overline{D^0}$ mesons and estimate their yield in 20% of the most central Xe+La and Pb+Pb collisions at the top SPS energy measured in the NA61/SHINE experiment. The multiplicity, also called the yield, is the average number of particles of interest created in a single inelastic collision.

The analysis is based on study of the two-body decay channels of D^0 and$\overline{D^0}$ mesons:

$$D^0 \to \pi^+ + K^-,$$
$$\overline{D^0} \to \pi^- + K^+,$$

for which the branching ratio is 3.87%.

Due to very low yield of D^0 mesons the analysis was performed for combined signal of $D^0 + \overline{D^0}$. The analysis methodology for obtaining $D^0 + \overline{D^0}$ meson spectra consists of the following steps:

- Selection of the events (details are described in Chapter 6);
- Obtaining the invariant mass histogram for unlike sign charge track pairs (no PID was applied);
- Applying the background suppression cuts to improve the signal to noise ratio (SNR);
- Fitting the signal and the background components of the invariant mass spectra;
- Extraction of $D^0 + \overline{D^0}$ signal and the estimation of the yield.

7.1 Invariant mass method

As was already mentioned earlier D mesons decay very close to the iteration point, mostly still within the target volume. This makes it impossible to observe D^0 and $\overline{D^0}$ mesons directly in the experiment. Thus, an indirect measurement called invariant mass method which based on direct measurements of the D mesons decay products is used.

Due to energy and momentum conservation laws, the four-momentum of a parent particle P_{parent} is equal to the sum of four-momentum of decay products. Thus, in case of D^0 decay in the channel $\pi^+ + K^-$

$$P_{D^0} = P_{\pi^+} + P_{K^-}.$$

Since in the experiment only momenta and sign of charge of particles are measured and without particle identification, in order to calculate the four-momentum one has to make an assumption about mass of a particle. In D^0 case daughter particles are assumed to be either π^+ or K^-, thus the four-momenta will be

$$P_{K^-} = \left(\sqrt{p_{K^-}^2 + m_K^2}, \overrightarrow{p}_{K^-}\right)$$
$$P_{\pi^+} = \left(\sqrt{p_{\pi^+}^2 + m_\pi^2}, \overrightarrow{p_{\pi^+}}\right),$$

where p stands for momentum and m for mass. Thus the invariant mass can be calculated as

$$m_{inv} = \sqrt{\left(\sqrt{p_{K^-}^2 + m_K^2} + \sqrt{p_{\pi^+}^2 + m_\pi^2}\right)^2 - (\overrightarrow{p_{K^-}} + \overrightarrow{p_{\pi^+}})^2}.$$

Since it is not known which tracks originating from D^0 or $\overline{D^0}$ and which are primary tracks or coming from other sources, all combinations of two oppositely charged tracks within an event are considered. For each such pair the invariant mass m_{inv} is calculated twice: assuming first particle to be pion and second one to be kaon and opposite.

The mean mass of D^0 (and $\overline{D^0}$) mesons is equal 1.86 GeV/c^2 and its natural width is much smaller as compare to the uncertainty in the invariant mass generated by the experimental effects.

To estimate the yield of the $D^0 + \overline{D^0}$ mesons the number of pairs in the spectrum contributing to resonant shape around mass of D^0 meson over the background distribution should be calculated. However the signal $D^0 + \overline{D^0}$ is not visible in the invariant mass spectrum due to the large combinatorial background which should be reduced by applying cuts as will be discussed below.

7.2 Background suppression cuts

As it is seen in Fig. 7.1 (which was made for simulated events, see details in Chapter 8) the combinatorial background is several orders of magnitude higher than the $D^0 + \overline{D^0}$ signal due to the low yield of charm particles. In order to reduce the large background five cuts are applied. The cut values were chosen according to simulations to maximise the signal to noise ratio (SNR) of the reconstructed $D^0 + \overline{D^0}$ peak. These cuts are:

- A cut on the track transverse momentum, p_T;
- A cut on the track impact parameter, d;
- A cut on the distance of the closest approach of daughter tracks, DCA;
- A cut on the longitudinal distance between the D^0 candidate decay vertex and the primary interaction point, V_z;
- A cut on the parent impact parameter: the back-extrapolated D^0 candidate trajectory based on its momentum vector and decay vertex, D.

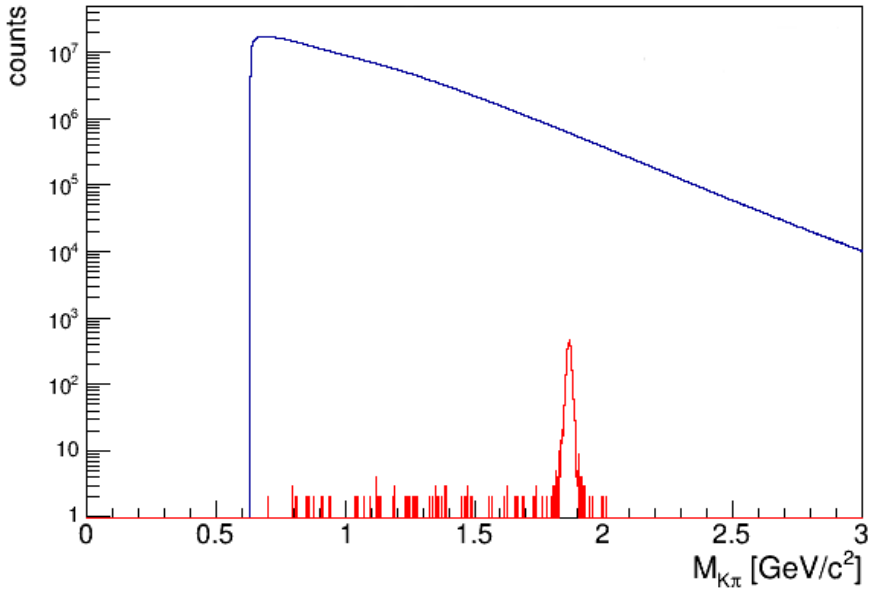

Figure 7.1: The invariant mass distribution for all pion-kaon pairs (blue line) and for $D^0+\overline{D^0}$ signal pairs (red line). The plot was made for Xe+La at $150A$ GeV/c simulations ($D^0+\overline{D^0}$ yield was assumed according to the SMES predictions, see details in Chapter 8).

The first two cuts are single-track cuts, while the last three are two-particle cuts. Note, that the last four cuts based on information delivered by SAVD, which provides precise position resolution of tracks near the interaction point. The graphical definitions of the last three cut variables are illustrated in Fig. 7.2. Fig. 7.3 presents the distributions of these variables for all combinatorial combinations, these plots can be compared to the distributions obtained for all pairs and signal pairs obtained for simulated data (Fig. 7.4 (see more details in Chapter 8).

The cut on the track transverse momentum p_T was introduced to reject the background since the signal spectrum is shifted to higher values of p_T compared to the background (see Fig. 7.4). Thus, rejection of tracks with low p_T significantly reduce the background while reduction of the signal is not significant.

The track impact parameter d is the distance of the closest approach between the extrapolated track and the primary vertex. The primary tracks have impact parameters close to zero, while secondary tracks are displaced from the primary vertex. The spread of the primary tracks about zero impact parameter is related to fine but limited spatial resolution and multiple scattering in the target and detector materials. Rejection of the tracks with small vales of d should remove the background and not influence much on the signal pairs.

The distance of closes approach DCA between paired tracks verifies, that the tracks originate from the same decay point: if the distance between tracks is large it rather corresponds to false secondary vertex candidate.

The distribution of V_z has a peak at zero as it is seen in Fig. 7.4, which corresponds to primary track pairs. Also V_z has only positive values, which can be explained by the kinematics. Thus, rejection of pairs with low and negative V_z should improve the signal to noise ratio.

The parent impact parameter D is the distance of the closest approach between the

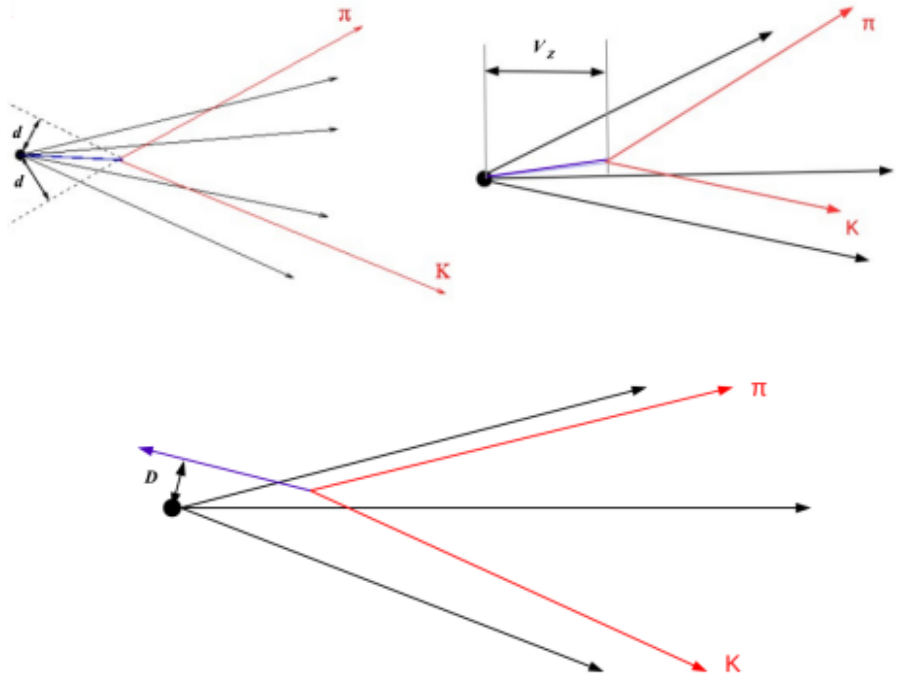

Figure 7.2: The sketch illustrating the decay topology and the applied cuts: upper left pad - for the track impact parameter d, upper right - for the longitudinal distance between the D^0 candidate decay vertex and the interaction point, V_z, bottom pad - for the parent impact parameter, D.

primary vertex and and the reconstructed trajectory of the D^0 meson. Since D^0 mesons originate from the primary interaction point, the signal pairs should have low values of D. The long tail at the higher values of the D distribution is associated with the pairs formed by primary track and track originating from a decay vertex. Such background pairs can be removed by rejecting pairs with high D values.

Table 7.2 shows selected cut values used in D^0 analysis for Xe+La and Pb+Pb at 150A GeV/c data.

Also, in the simulations (see Chapter 8) it was observed, that the opening angle of the D^0 decay is such, that it is more probable, that the daughter particles will be detected in different arms of SAVD (scheme is shown in Fig. 7.5). Thus, to improve the SNR the pairs which are registered within the same arm were selected for the analysis.

Moreover, it is more probable, that at least one of D^0 daughters avoid the first station

Cut	Xe+La at 150A GeV/c	Pb+Pb at 150A GeV/c
p_T	0.32 GeV/c	0.35 GeV/c
d	37 μm	37 μm
DCA	36 μm	36 μm
V_z	1050 μm	850 μm
D	18 μm	20 μm

Table 7.1: Applied cut values used to reduce combinatorial background in the invariant aroud the D^0 mass region for Xe+La and Pb+Pb at 150A GeV/c data.

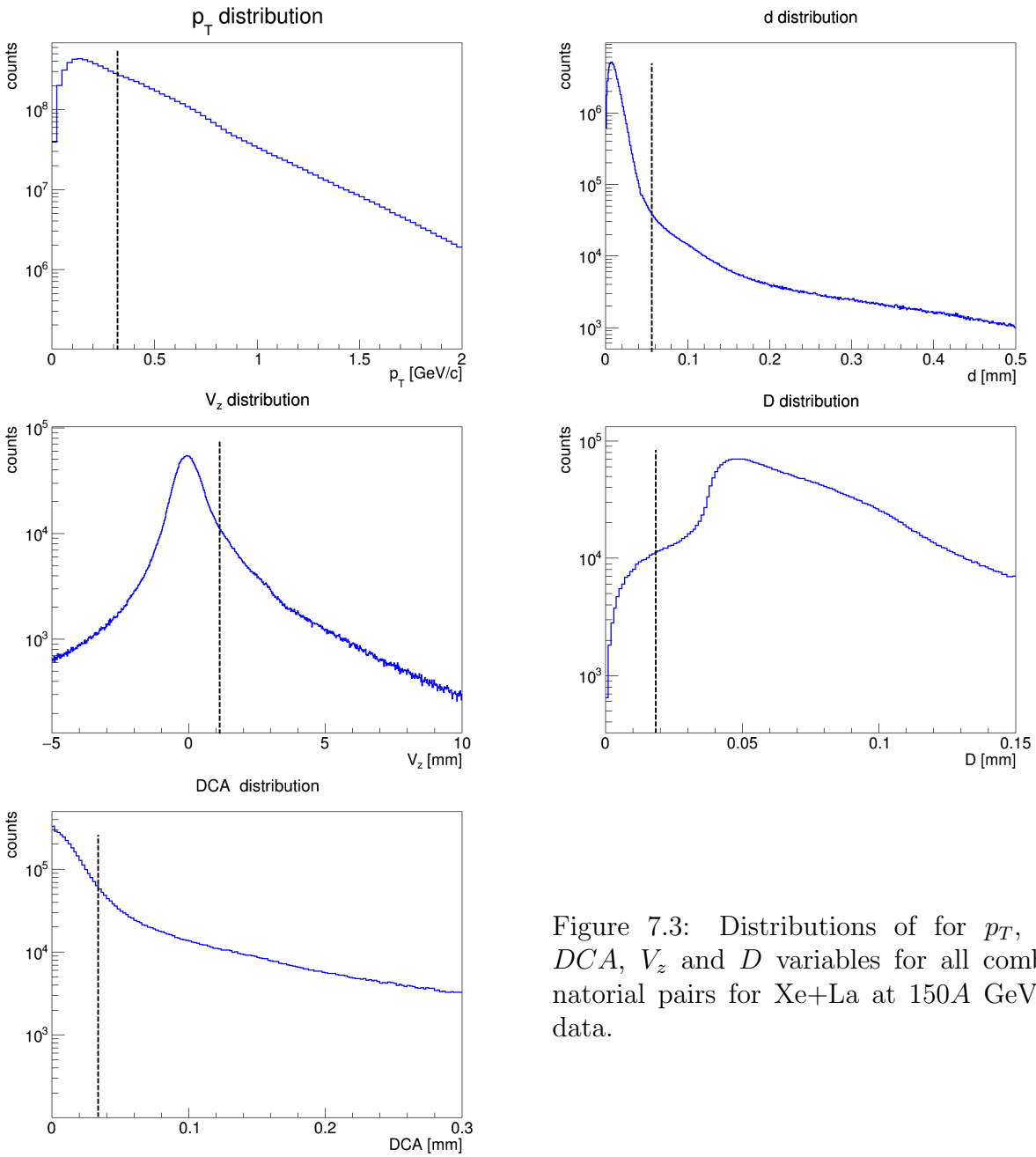

Figure 7.3: Distributions of for p_T, d, DCA, V_z and D variables for all combinatorial pairs for Xe+La at 150A GeV/c data.

of SAVD. Thus, only track pairs in which one or both tracks have the first hit on the second station of SAVD were considered for analysis.

7.3 Invariant mass distribution of $D^0 + \overline{D^0}$

Fig. 7.6 and Fig. 7.7 show the invariant mass distributions of unlike charge daughter candidates and the background reduction with the subsequent application of the discussed above cuts. The application of all cuts allows to suppress the background by a factor of 10^5 while the signal is suppressed by factor of 5 (these results were obtained in the performed simulation study, see Chapter 8).

Fig. 7.3 and Fig. 7.3 show the invariant mass distribution after all cuts applied. The simulated data suggests that the signal can be described by the Gaussian distribution

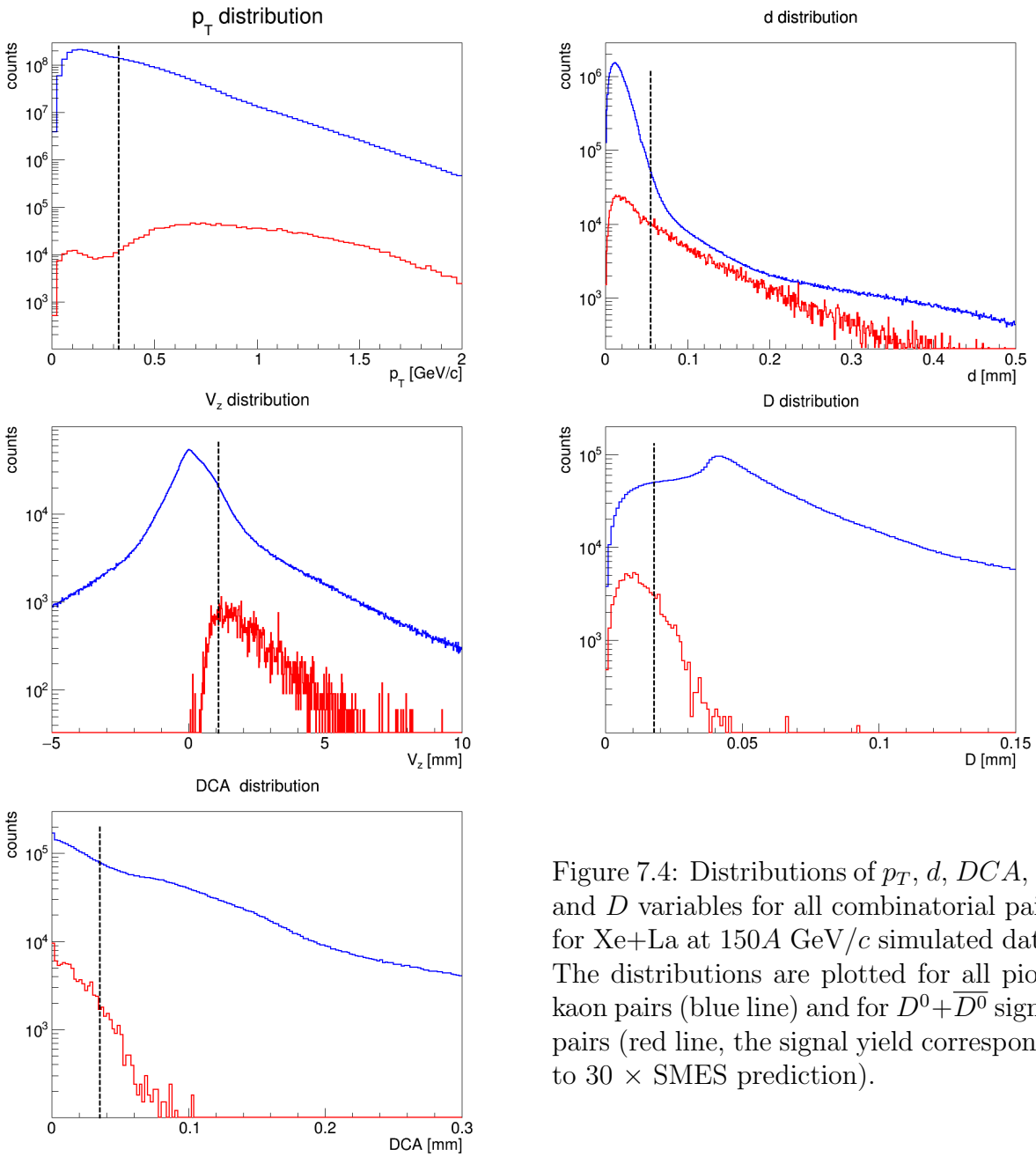

Figure 7.4: Distributions of p_T, d, DCA, V_z and D variables for all combinatorial pairs for Xe+La at 150A GeV/c simulated data. The distributions are plotted for all pion-kaon pairs (blue line) and for D^0+$\overline{D^0}$ signal pairs (red line, the signal yield corresponds to 30 $\times$ SMES prediction).

(see Fig. 7.3):

$$\frac{dn}{dm} = \frac{1}{\sigma\sqrt{2\pi}} exp[-\frac{(N-\mu)^2}{2\sigma^2}],$$

where N is the total yield per event, m_0 is the D^0 mass and σ is the width of the distribution (which depends on the detector resolution). The background is described by the exponent in the region of the expected signal. Thus, the invariant mass distributions in Fig. 7.3 and Fig. 7.3 were fitted with a sum of an exponential function and a Gaussian (red line on plots).

For Xe+La at 150A GeV/c data one finds from the fit the width of the peak to be 0.012 MeV (which is consistent with the value obtained in simulations assuming the instrumental effects – see Fig. 7.3) and the total yield to amount to 80 $\pm$ 28 with the SNR of 3.4 (integrated over $\pm 3\sigma$). This can be recalculated to total $D^0 + \overline{D^0}$ yield per event

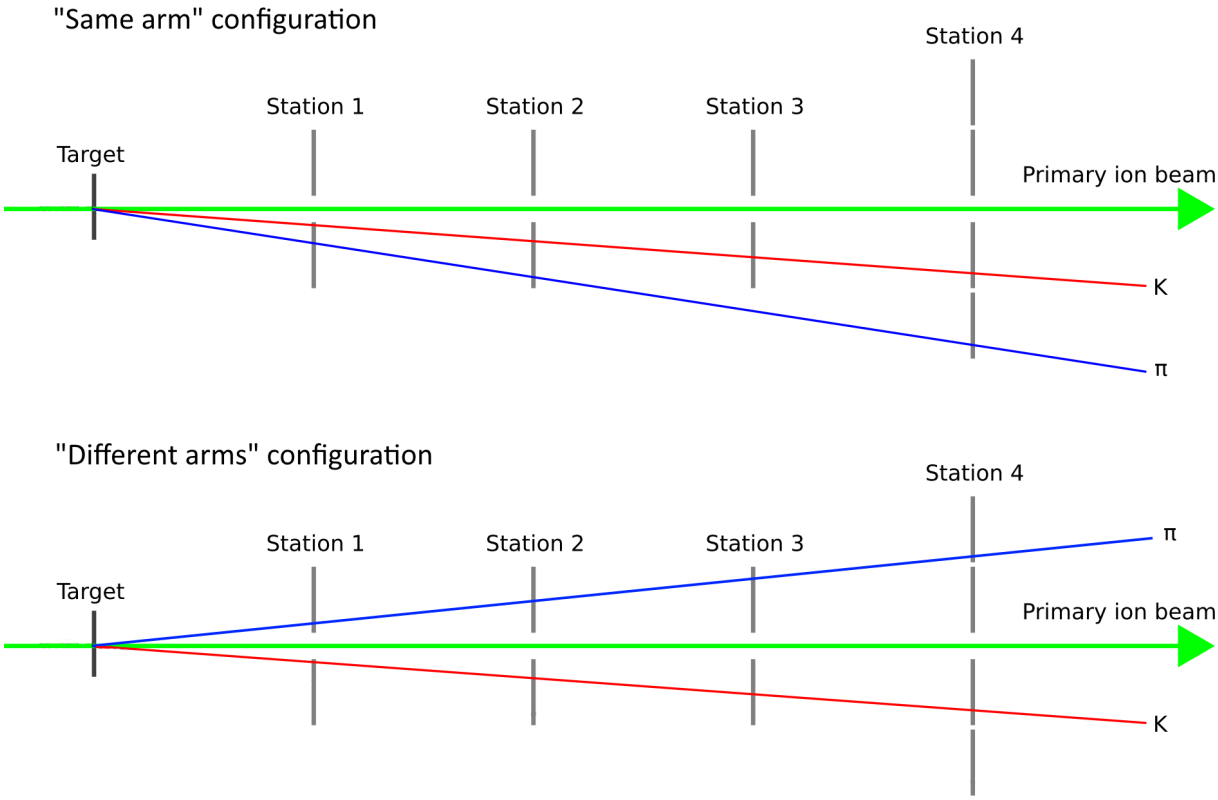

Figure 7.5: Visualization of D^0s decay into charged pion and kaon ($D^0 \rightarrow \pi^+ + K^-$): daughter tracks are registered in the same arm (upper pad) and the different arms (bottom pad) of SAVD.

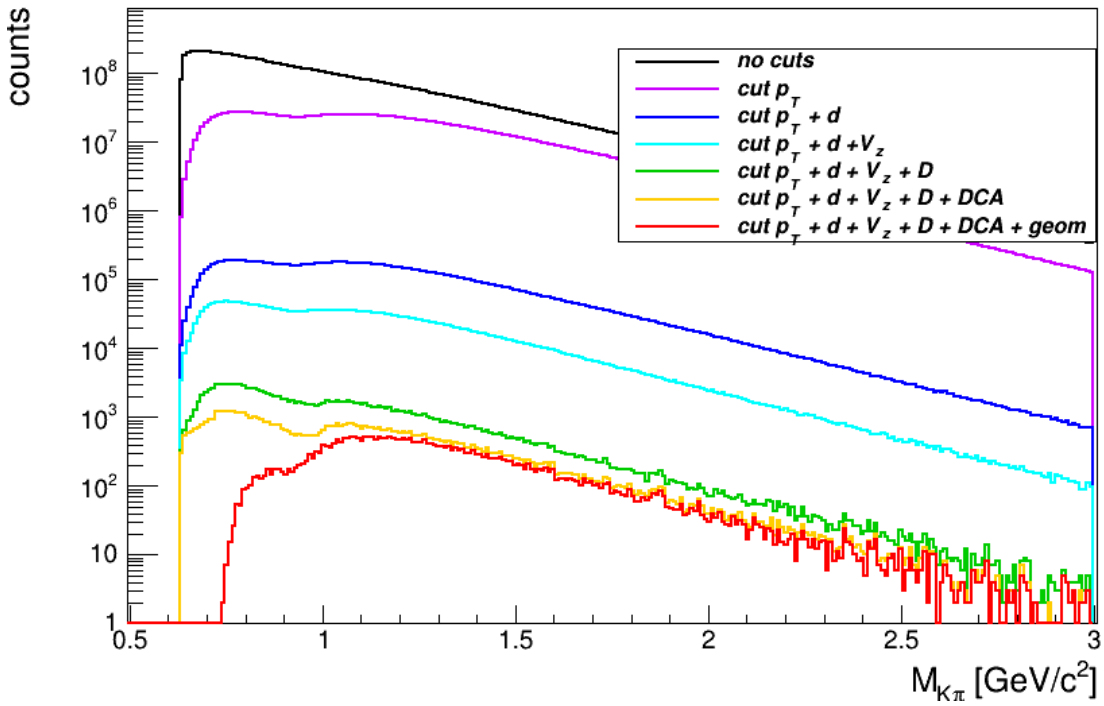

Figure 7.6: Invariant mass distribution of unlike charge sign π, K decay track candidates for Xe+La collisions at 150A GeV/c. Different colours correspond to different cuts applied (indicated on plot).

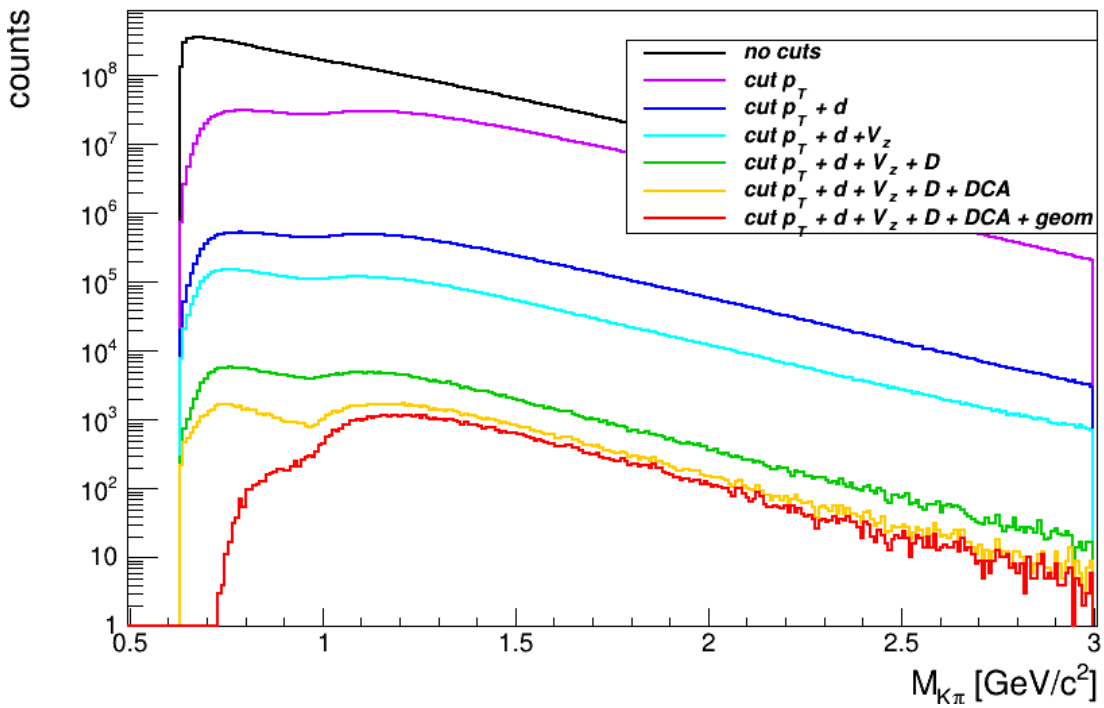

Figure 7.7: Invariant mass distribution of unlike charge sign π, K decay track candidates for Pb+Pb collisions at 150A GeV/c. Different colours correspond to different cuts applied (indicated on plot).

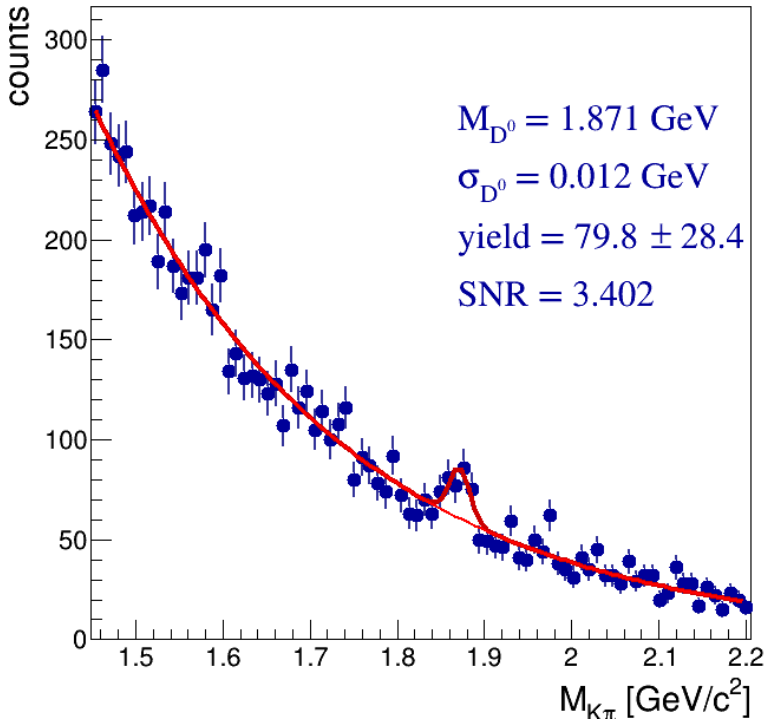

Figure 7.8: Invariant mass distribution of unlike charge sign π, K decay track candidates for Xe+La collisions at 150A GeV/c. The indicated errors are statistical only. The red line represents the fit described in the text, the obtained fit parameters are indicated on plot.

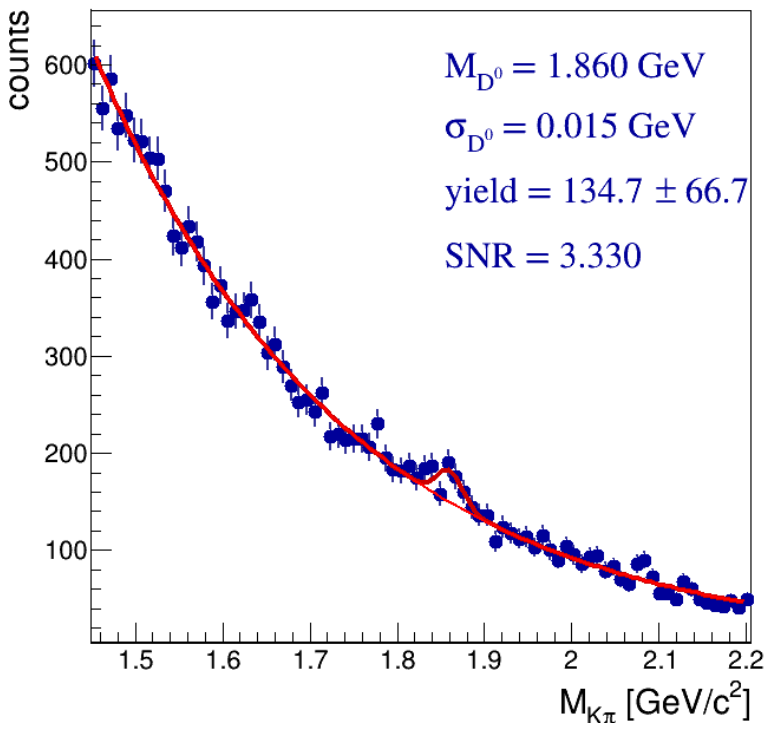

Figure 7.9: Invariant mass distribution of unlike charge sign π, K decay track candidates for Pb+Pb collisions at 150A GeV/c. The indicated errors are statistical only. The red line represents the fit described in the text, the obtained fit parameters are indicated on plot.

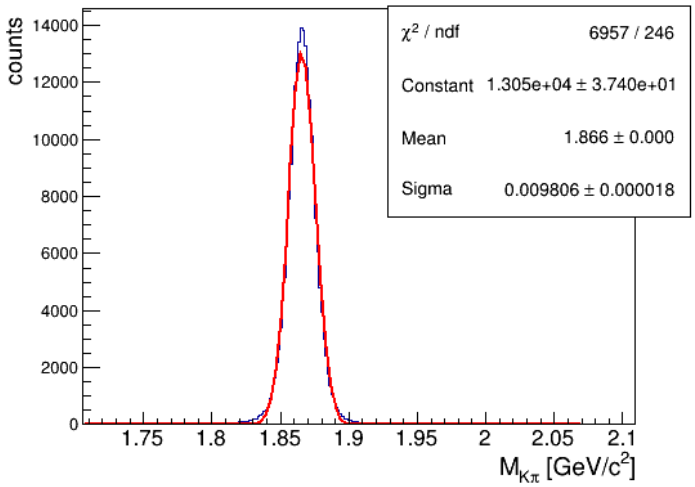

Figure 7.10: Invariant mass distribution of reconstructed simulated $D^0 + \overline{D^0}$ decays for Xe+La collisions at 150A GeV/c. The red line represents the Gaussian fit described in the text, the parameters of the fit are indicated on plot.

taking into account the branching ratio (3.89%) and the correction factor for efficiency, acceptance and suppression of cuts (1.07% (AMPT) and 0.74% (PHSD), see Chapter 8). Thus, it gives the total yield per event

$$N(D^0 + \overline{D^0})_{Xe+La,AMPT} = 0.10 \pm 0.03,$$
$$N(D^0 + \overline{D^0})_{Xe+La,PHSD} = 0.15 \pm 0.05.$$

For Pb+Pb at 150A GeV/c data from the fit one finds the width of the peak to be 0.015 MeV and the total yield to amount to 130 ± 70 with a $\pm 3\sigma$ integrated SNR of 3.3. Taking into account the branching ratio and the correction factor ((1.03% (AMPT) and 0.87% (PHSD)) gives the total yield per event

$$N(D^0 + \overline{D^0})_{Pb+Pb,AMPT} = 0.33 \pm 0.18,$$
$$N(D^0 + \overline{D^0})_{Pb+Pb,PHSD} = 0.39 \pm 0.21.$$

7.4 Upper limit estimation of $D^0 + \overline{D^0}$ yield

An upper limit for the number of $D^0 + \overline{D^0}$ per event can be estimated using Bayesian approach [71]. The likelihood $P(data|N)$ (i.e. the conditional probability density distribution of the data when number of $D^0 + \overline{D^0}$ per event is N) is parametrized as a Gaussian:

$$P(data|N) = \frac{1}{\sigma\sqrt{2\pi}} exp[-\frac{(N-\mu)^2}{2\sigma^2}] \equiv g(N;\mu,\sigma),$$

with the mean $\mu = 80$ ($N(D^0+\overline{D^0})$) and the width $\sigma = 28$ (statistical error of $N(D^0+\overline{D^0})$) for Xe+La data and $\mu = 130$ and $\sigma = 70$ for Pb+Pb data as was obtained from the fit to the invariant mass spectra. Using the Bayes' theorem the posterior distribution $P(data|N)$ is calculated by multiplying the likelihood with an assumed prior probability distribution of N which is taken to be zero for $N < 0$ and uniform for $N \geq 0$. This prior distribution forces N to be positive as it should be. The confidence level CL can be calculated by integration of the posterior distribution:

$$CL \equiv \int_0^M P(data|N) = \frac{\int_0^M g(N;\mu,\sigma)dN}{\int_0^\infty g(N;\mu,\sigma)dN},$$

where M is the upper limit of the number of $D^0 + \overline{D^0}$ per event N corresponding to the confidence level CL. Using the fitted values of μ and σ, the upper limit of the total yield of $D^0 + \overline{D^0}$ at 98% CL is found to be for Xe+La event

$$\begin{aligned} M(D^0 + \overline{D^0})_{AMPT,Xe+La} &= 0.17, \\ M(D^0 + \overline{D^0})_{PHSD,Xe+La} &= 0.25. \end{aligned} \tag{7.1}$$

and for Pb+Pb event

$$\begin{aligned} M(D^0 + \overline{D^0})_{AMPT,Pb+Pb} &= 0.70, \\ M(D^0 + \overline{D^0})_{PHSD,Pb+Pb} &= 0.82. \end{aligned} \tag{7.2}$$

7.5 Invariant mass distribution of Λ and K_s^0

To test the detector capabilities and validate the D^0 peak extraction procedure, it was also attempted to reconstruct Λ and K_s^0 signals (into $p + \pi$ and $\pi + \pi^-$ two body decay channels respectively), which are much more abundantly produced. However, one can reconstruct only a small fraction of all K_s^0 and even smaller of all Λ with SAVD since the detector design and the tracking algorithm were optimized for decays which have much shorter decay length (decay length $c\tau$ of Λ is 7.89 cm and of K_s^0 is 2.68 cm). Also for this test the background suppression cuts were not optimised and the same values were used as for $D^0 + \overline{D^0}$ analysis.

A clear peak corresponding to K_s^0 decays (in the left pad of Fig. 7.5 was observed with a SNR over 70. Also, for Λ and $\overline{\Lambda}$ clear peaks (in the right pads of Fig. 7.5) are found with a SNR 29 and 10, correspondingly. From the obtained yield, it is seen, that number of Λ barions is about factor of 10 higher then number of $\overline{\Lambda}$. This result corresponds to the results obtained by the NA49 Collaboration $\overline{\Lambda}/\overline{\Lambda}$ equal to 0.1 at mid rapidity for the most central collisions (N_{part}=352) [72].

Note, that after the applied background suppression cuts, in case of Λ, the background is almost negligible around the signal invariant mass. This allows for testing quality of reconstructed data such as estimation of the secondary vertex resolution (described in Chapter 4). Also, one can check the distribution of the DCA values of the $p + \pi$ pairs, that are contributing to the peak of Λ candidates in the invariant mass spectra. Example of such distribution is shown in Fig. 7.5): the red line corresponds to the pairs, that contribute to the peak while blue line corresponds to all pairs. It is seen, that almost all pairs contributing to the Λ peak have the DCA values below 0.05 μm.

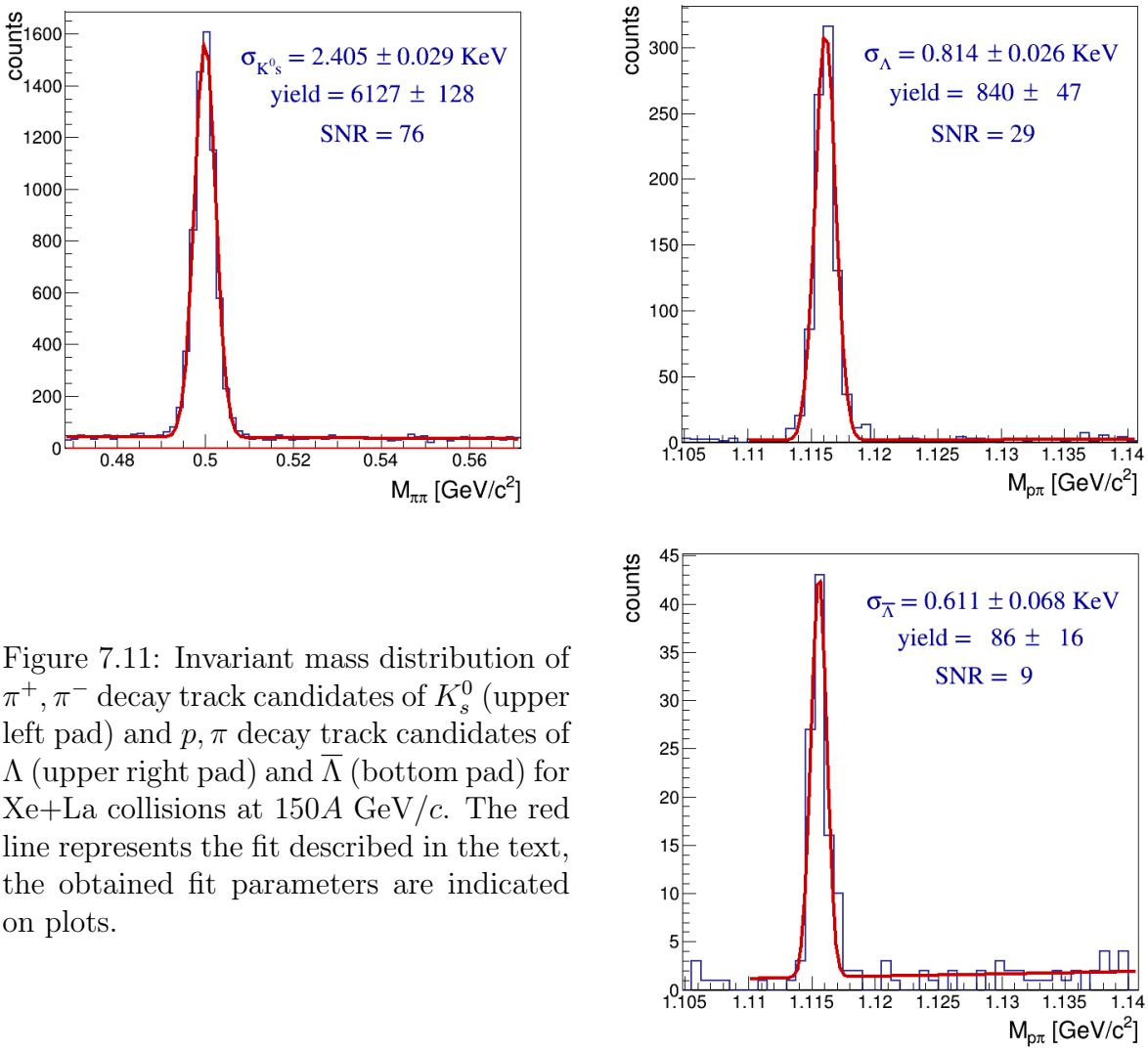

Figure 7.11: Invariant mass distribution of π^+, π^- decay track candidates of K_s^0 (upper left pad) and p, π decay track candidates of Λ (upper right pad) and $\overline{\Lambda}$ (bottom pad) for Xe+La collisions at 150A GeV/c. The red line represents the fit described in the text, the obtained fit parameters are indicated on plots.

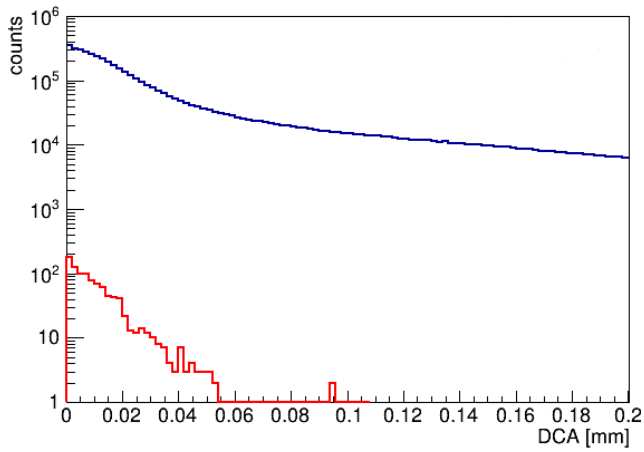

Figure 7.12: The DCA distribution of Λ candidates (red line) and all combinations (blue line). The distributions are plotted for Xe+La at 150A GeV/c data.

Chapter 8

Simulations

Dedicated software based on Monte Carlo (MC) techniques was used for simulation of iterations of the beam particle on target, propagation of the produced particles in the collision through the detector system, and simulation of processes related to the detection of the detector signal.

In the analysis presented in this thesis the MC simulation was used:

- to study the detector response and obtain the resolution;
- to estimate the reconstruction efficiency;
- to obtain the correction for the final result.

The effects which are not included in the performed simulation are:

- Energy loss of the produced particles in the TPCs;
- Response of the PSD calorimeter;
- Propagation of the beam particle through the beam upstream from the target and deviations of the beam direction from the z axis;
- Primary interactions outside the target;
- Other beam particles arriving during the TPC readout.

Skipping these effects in the simulation chain significantly reduces the processing time and in principle should not lead to inconsistency between simulated events and events collected during data taking with the applied event cuts (see Chapter 6).

8.1 Simulation chain

Firstly, the event generator simulates the initial nucleus-nucleus interaction and provides list of primary produced particles and information about their momenta. Particles with very short lifetime also decay at the event generator level and the decay products are considered primary (this does not concern D mesons).

Further, the particles are propagated through the detector volume and the detector response is simulated using GEANT4 10.4.3 package [73]. This includes interaction with detector materials, propagation through magnetic field and other physical processes such

as decays. The detailed detector model of the detector contains information about all materials and geometrical properties of the construction elements of the detector. The primary interaction points are randomly placed in the target volume, according to the beam distribution in transverse plane sampled from the real data. In the longitudinal direction the beam is distributed according to the exponential function taking into account iterations on the target material. In the last step, the signals generated by the particles propagating through the detector sensitive volumes are recorded and digitized.

The output is saved in the real data format and later reconstructed using the reconstruction chain described in Chapter 4.

As mentioned earlier, the simulations made for this study do not include PSD detector due to long computing time required for simulation of calorimeter response for heavy-ion systems.

The following naming convention is used in this chapter:

- The event generated by event generator, which contains information on primary particles positions and momenta is called *generated event*;
- The event in which the detector response for the produced particles was simulated is called *MC event*;
- The event which was reconstructed from the *MC event* is called *reconstructed* or *RecMC event*.
- The event collected during the data taking and afterwards reconstructed is called *real data* and labelled *Rec event*.

8.1.1 SAVD in simulations

The SAVD model in GEANT4 was setup to describe all significant features of the real device. It consists of 16 sensors at positions and rotations corresponding to the real geometry. Each sensor consists of a layer of silicon (pixel, epitaxial and substrate layers) with total thickness of 50 μm, 50 μm of epoxy glue layer and carbon layer of 300 μm which represents the supporting ladders. The SAVD stations are enclosed in a He vessel equipped with front and back Mylar windows.

When the particle crosses the sensitive volume of the sensor a hit is created. To reproduce the sensor response a simple digitizer was introduced. The digitizer converts GEANT4 hits to cluster with applied smearing of the hit position according to obtained cluster position resolution for real data (see Fig. 4.2).

As it was discussed in Chapter 4, during data taking the sensors were not fully efficient, moreover the electronic noise was present on the typical level for MIMOSA-26AHR of 10^{-4} hits per pixel per frame. To reproduce these results the generated clusters were randomly rejected according to the efficiency estimated for real data, while other pixels were randomly fired with the given probability related to the noise level.

Information about the fired pixels is saved in the real data format and the reconstruction undergoes the same procedure as was described in Chapter 4.

8.2 Event generators

A Multi-Phase Transport model (AMPT) [74, 75, 76] was chosen to describe background pions and kaons. The most recent version v1.26t9b-v2.26t9b was used.

The AMPT model was developed to describe non-equilibrium many-body dynamics, it includes both initial partonic and final hadronic interactions and the transition between these two phases of matter [74]. AMPT simulates nuclear collisions for energies from $\sqrt{s_{\mathrm{NN}}} = 5$ GeV up to 5500 GeV. For the initial conditions, which include spatial and momentum distributions of minijet partons and soft string excitations, the AMPT model uses the Heavy Ion Jet Interaction Generator (HIJING) model [77]. Further, the Zhang's parton cascade (ZPC) [78] is used to describe parton interactions, which is followed by a hadronization process based on the Lund string fragmentation model [79, 80]. Finally, the scattering among the produced hadrons are described by A Relativistic Transport (ART) model [81].

Fig. 8.1 shows the rapidity and transverse mass distributions predicted by AMPT and data points obtained in the NA49 experiment for 5% of the most central Pb+Pb collisions [82]. It is seen, that AMPT provides a good description of charged pions and kaons, which are major contribution to the background of open charm particles.

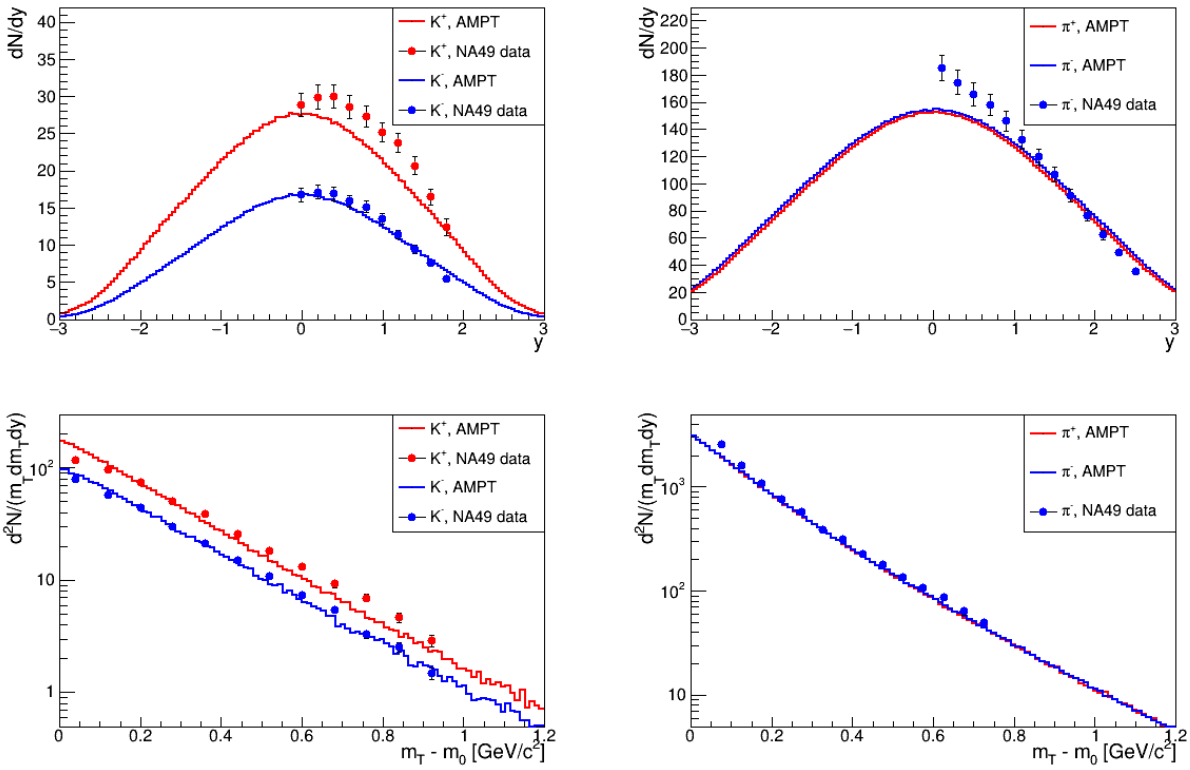

Figure 8.1: Upper pads: Rapidity distribution of charged kaons (left pad) and pions (right pad). Bottom pads: Transverse mass distribution of charged kaons in the rapidity interval $-0.1 < y < 0.1$ (left pad) and pions in the rapidity interval $0 < y < 0.2$ (right pad). The solid lines show results form the AMPT model obtained for 0-5% central (impact parameter $b \leq 3$ fm) Pb+Pb collisions at $\sqrt{s_{NN}} = 17.3$ GeV. Circles represent data collected by the NA49 experiment at same conditions taken from [82].

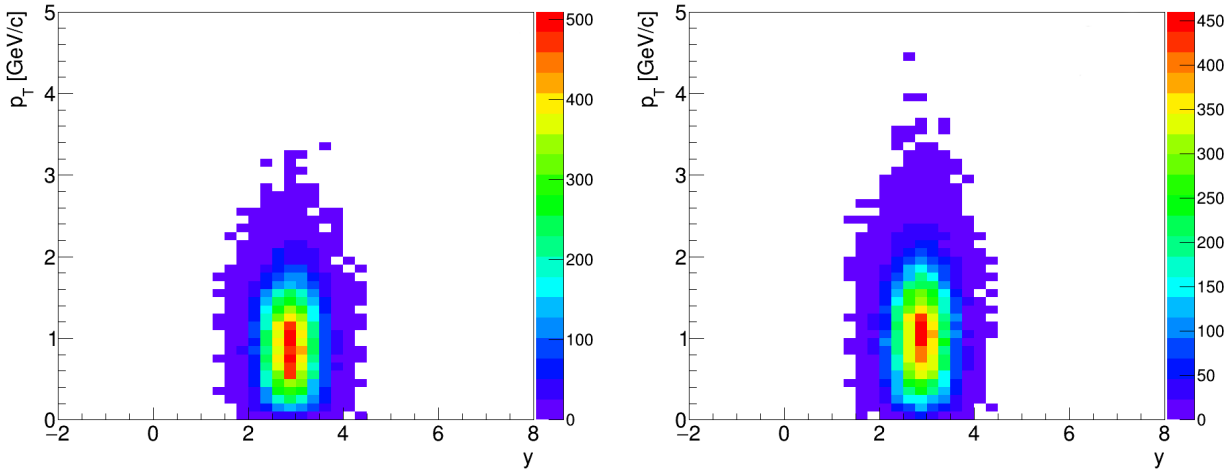

Figure 8.2: Rapidity – transverse momentum spectra of $D^0 + \overline{D^0}$ mesons for 20% of the most central Xe+La (left pad) and Pb+Pb (right pad) collisions at 150A GeV/c according to the AMPT predictions.

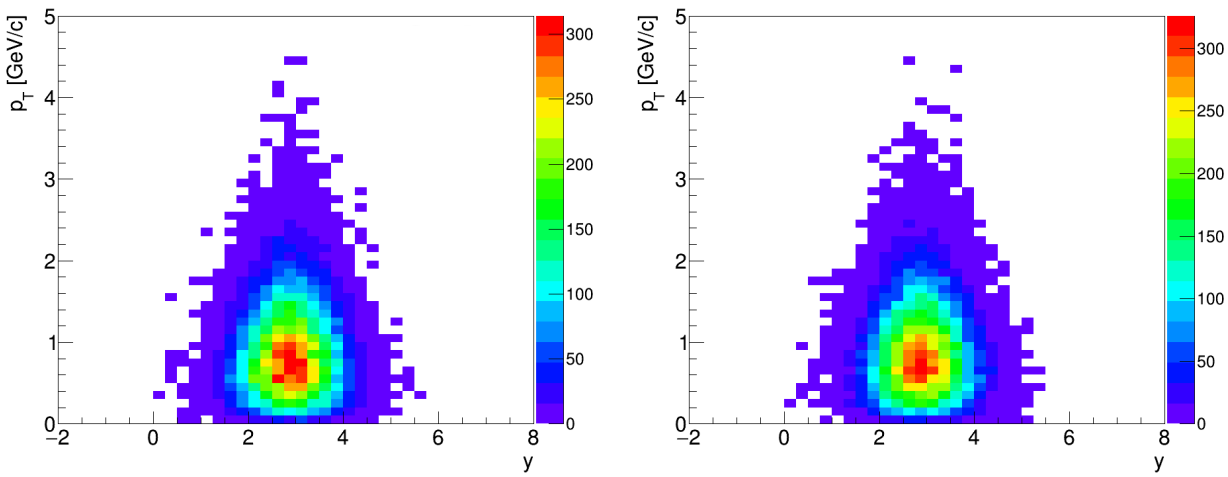

Figure 8.3: Rapidity – transverse momentum spectra of $D^0 + \overline{D^0}$ mesons for 20% of the most central Xe+La (left pad) and Pb+Pb (right pad) collisions at 150A GeV/c according to the PHSD predictions.

However, the AMPT model was not aimed to describe well charm mesons: thus, the AMPT model predicts the average multiplicity of 0.01 for $D^0 + \overline{D^0}$ in central Pb+Pb events which seems to be underprediction according to models discussed in Chapter 2. However, the predicted in the AMPT model phase space distribution looks reasonable (see the rapidity – transverse momentum spectra of $D^0 + \overline{D^0}$ for 20% of the most central Xe+La (left pad) and Pb+Pb (right pad) at 150A GeV/c in Fig. 8.2), though there no data so far for comparison. Additionally to events with $D^0 + \overline{D^0}$ distributed according to the AMPT phase space, events with $D^0 + \overline{D^0}$ distributed the PHSD phase space [21] were used.

The PHSD model is a microscopic off-shell transport approach. Within this model the full evolution of a heavy-ion collision is described as following: starting from the initial hard scatterings and string formation, through the dynamical deconfinement phase transi-

tion to the quark-gluon plasma followed by hadronization and the subsequent interactions in the hadronic phase [21]. In Fig. 8.3 the rapidity – transverse momentum spectra of D^0 + $\overline{D^0}$ according to PHSD predictions are shown for 20% of the most central Xe+La (left pad) and Pb+Pb (right pad) at 150A GeV/c.

These spectra (Fig. 8.2 and Fig. 8.3) were parametrized and the mixed event was created: the AMPT generated event was enriched with 5 D^0 or $\overline{D^0}$ mesons distributed according to the AMPT or PHSD phase space distribution. Thus, these mixed events contain both proper description of the background (AMPT) and D meson signal for two models (AMPT and PHSD).

8.3 Simulation results

8.3.1 Simulation performance

Monte Carlo simulations were validated in several tests. The simulated distributions of selected parameters were compared with those collected during data taking. It is expected, that if the simulation was accurate, these distributions should be similar.

In this Section the comparison between distributions obtained for real and simulated data is presented for Xe+La at 150A GeV/c data, for Pb+Pb at 150A GeV/c the distributions look similar.

The events from the simulation study don't require the event cuts discussed in Chapter 6 since by construction they already have one beam-target interaction per event, defined beam particles (Xe or Pb), selected centrality, etc.

TPC distributions

Similarly as it was done for real data (Fig. 5.3), the distributions of differences Δy between the vertical coordinate of the extrapolated track from given TPC and the measured by other TPC calculated for each track are presented in Fig. 8.4. In case of simulation these plots have strictly horizontal structure which corresponds to perfect drift velocity v_{drift} calibration used during reconstruction (during simulation and reconstruction the same values of v_{drift} were used), which is not the case for collected data when v_{drift} was calibrated to be close to the actual v_{drift}.

The residual plots for x and y coordinates are presented in Fig. 8.5. The green colour of the distribution corresponds to mean value of the residuals equal to zero. These plots are consistent with the same plots (see Fig. 5.4) obtained for real data.

In Fig. 8.6 distributions of clusters allocated to the track for real and simulated reconstructed events are shown. Maxima visible in the distributions correspond to tracks measured in few sectors of VTPC-1 (region with low number of clusters), in the whole volume of VTPC-1 (72 clusters), VTPC-2 and one of MTPC (162 clusters); the distribution reaches 234 clusters, which corresponds to track measured by both VTPCs and one of MTPC. The distributions for the real data are slightly shifted towards lower values is respect to simulated data. This effect is related to instrumental effects not properly described in simulations like clusters detection inefficiency of the particular sectors in TPCs.

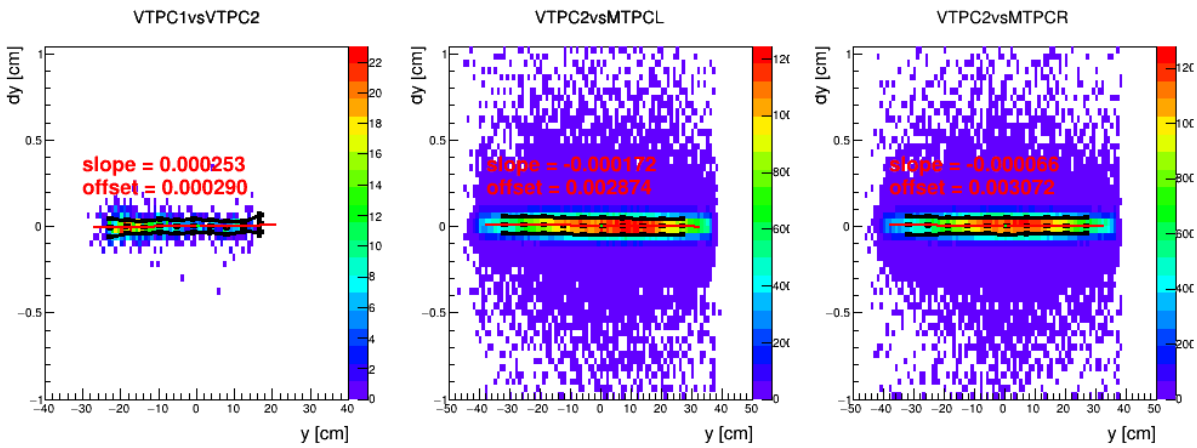

Figure 8.4: The example Δy vs y plot for simulated Xe+La at 150A GeV/c data. Drift velocity is calculated using the described above calibration procedure. The distribution was fitted with Gaussian in each y slice and the mean values are marked as black dots. The black lines are $\pm$ 3σ around the mean values. The black dots were fitted with straight line (red line on plots) and the parameters are indicated on plots.

Fig. 8.7 shows the TPC track multiplicity distributions for reconstructed real and simulated events for Xe+La and Pb+Pb at 150A GeV/c. The obtained distributions have similar shape, though for the simulated data it is slightly shifted towards higher multiplicity. A bit worse performance might be an effect of not perfect TPC calibration or not enough strict event selection.

In Fig. 8.8 the distributions of the z coordinate of the reconstructed TPC primary vertex (reconstructed not using BPD information as described in Chapter 4) is shown for real data and simulations. The distributions are fitted with Gaussian. The distributions have similar width though the performance in the simulation is slightly better.

SAVD distributions

Similar as for the TPC vertex the distributions of the z coordinate of the reconstructed SAVD primary vertices are shown for data and simulations in Fig. 8.9. The segmented target profile is clearly visible in real data. However, as it was mentioned earlier, in simulations the La target volume was not segmented which is reflected in uniform distribution seen in Fig. 8.9 (left pad).

The distributions of differences between x, y and z coordinates of the primary vertices reconstructed using tracks from two sub-samples as was described in Chapter 4 are shown in Fig. 8.10. These distributions are similar as Fig. 4.2.2 obtained for real data. The sigma of these distributions can be converted to the spatial resolution of the primary vertex $\sigma_x \approx 4.1$ μm, $\sigma_y \approx 2.3$ μm and $\sigma_z \approx 34.9$ μm.

Fig. 8.11 shows the SAVD-TPC track multiplicity distributions for reconstructed real and simulated events for Xe+La and Pb+Pb at 150A GeV/c. It is seen, that the distributions have similar shape, though for the simulated data of Xe+La it is slightly shifted towards higher multiplicity.

The matched SAVD track multiplicity versus SAVD track multiplicity is shown in Fig. 8.12. The distributions for real and simulated data look similar. In both cases about

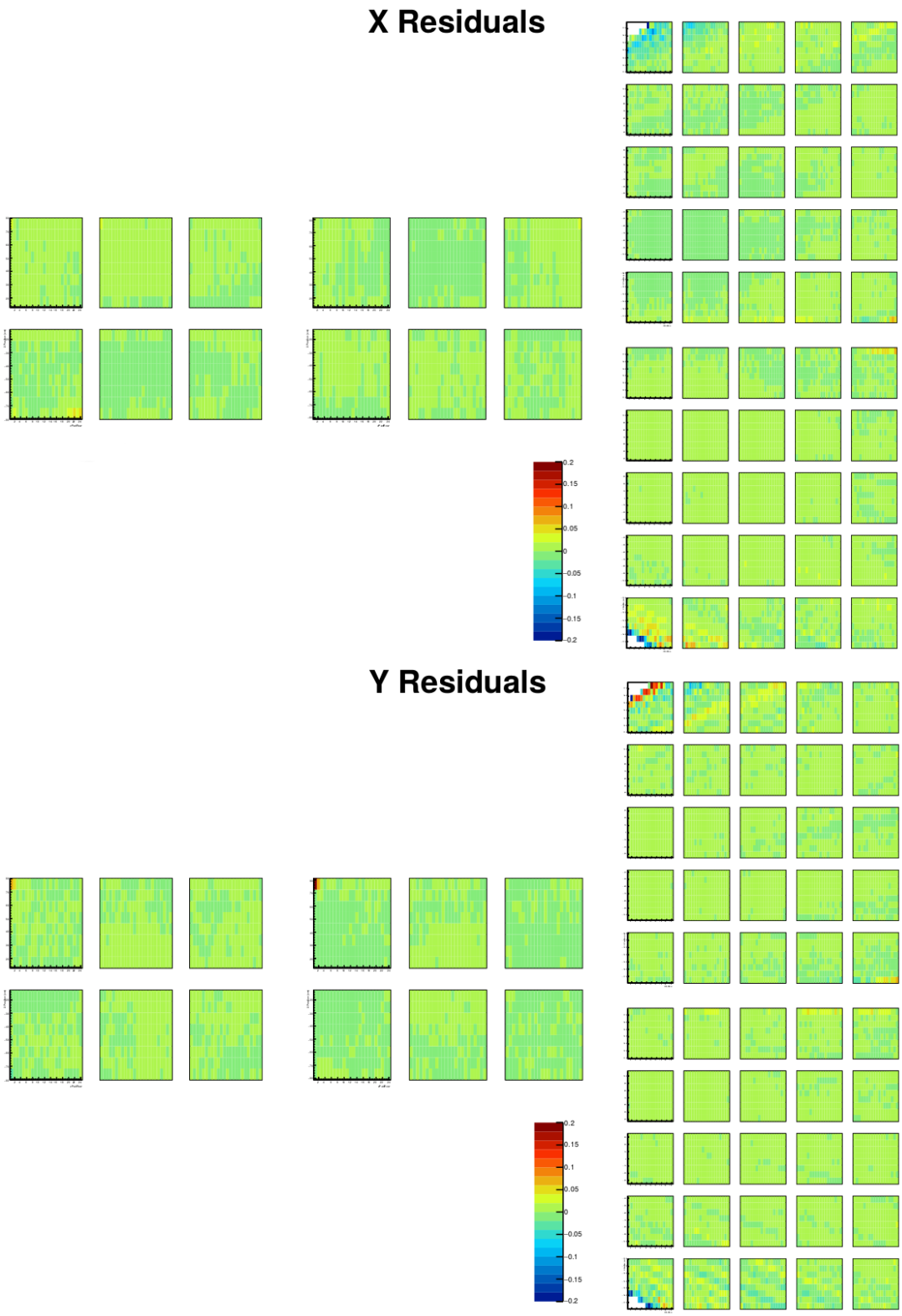

Figure 8.5: The residuals plots for x (top pad) and y (bottom pad) for simulated Xe+La at $150A$ GeV/c data. The binning used on the plots corresponds to the size of the TPC pads.

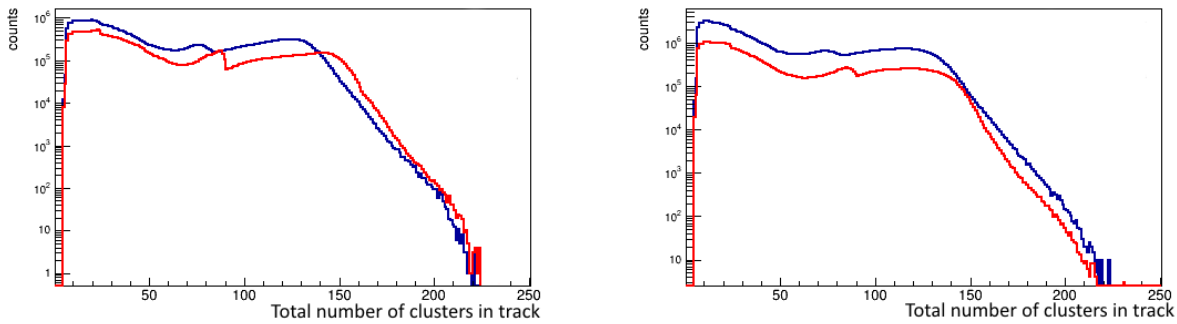

Figure 8.6: The distribution of clusters assigned to a track for reconstructed real (blue line) and simulated (red line) Xe+La (left pad) and Pb+Pb (right pad) at 150A GeV/c events.

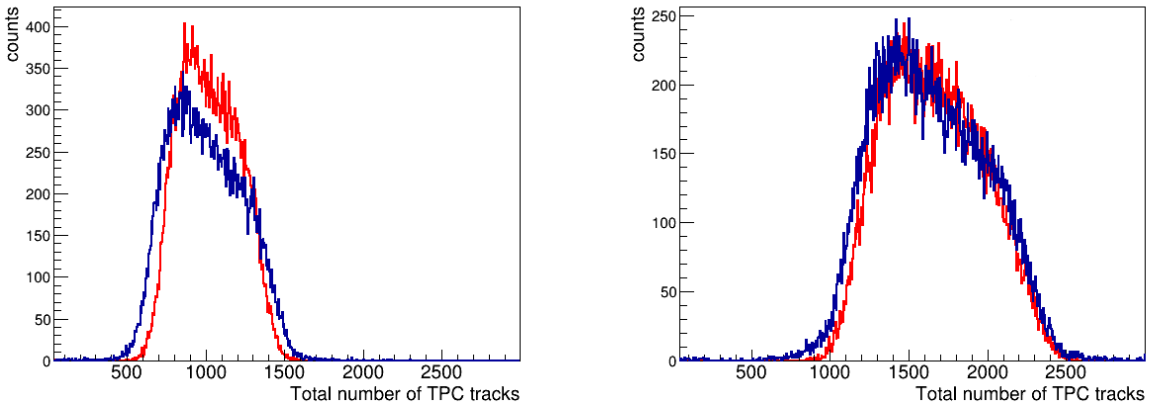

Figure 8.7: The distribution of number of TPC reconstructed tracks for reconstructed real (blue line) and simulated (red line) Xe+La (left pad) and Pb+Pb (right pad) at 150A GeV/c events.

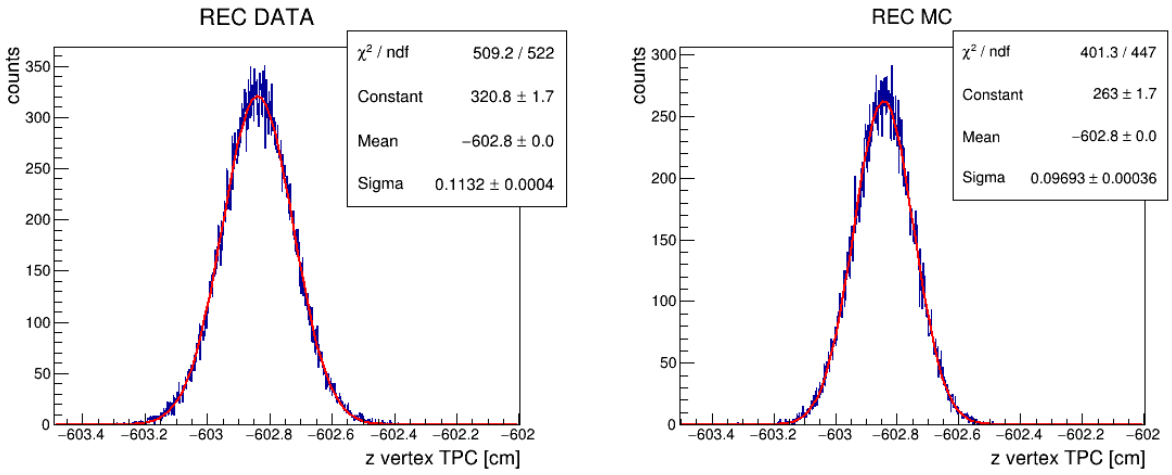

Figure 8.8: The distributions of the reconstructed TPC primary vertex for reconstructed real (left pad) and simulated (right pad) events for Xe+La at 150A GeV/c. The distributions are fitted with Gaussian (red line). The parameters resulted from fits are shown on plots.

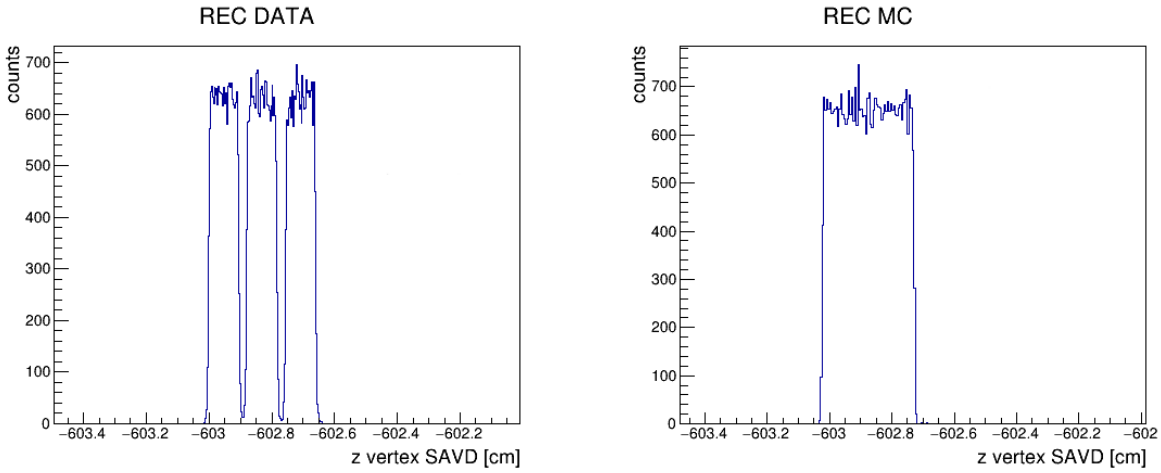

Figure 8.9: The distributions of the reconstructed TPC primary vertex for reconstructed real (left pad) and simulated (right pad) Xe+La at 150A GeV/c.

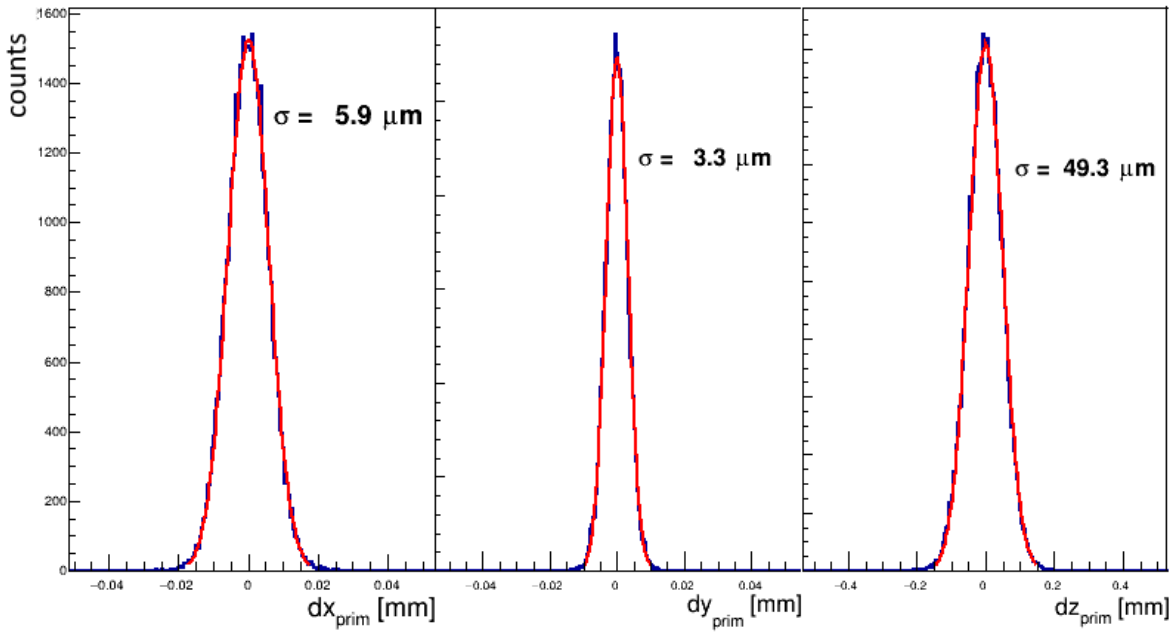

Figure 8.10: Distributions of differences between x, y and z coordinates of the primary vertex reconstructed using tracks from two sub-samples (see Chapter 4 details) for simulated Xe+La at 150A GeV/c data. Red lines correspond to Gaussian fits to the distributions, the sigma values are indicated on plots.

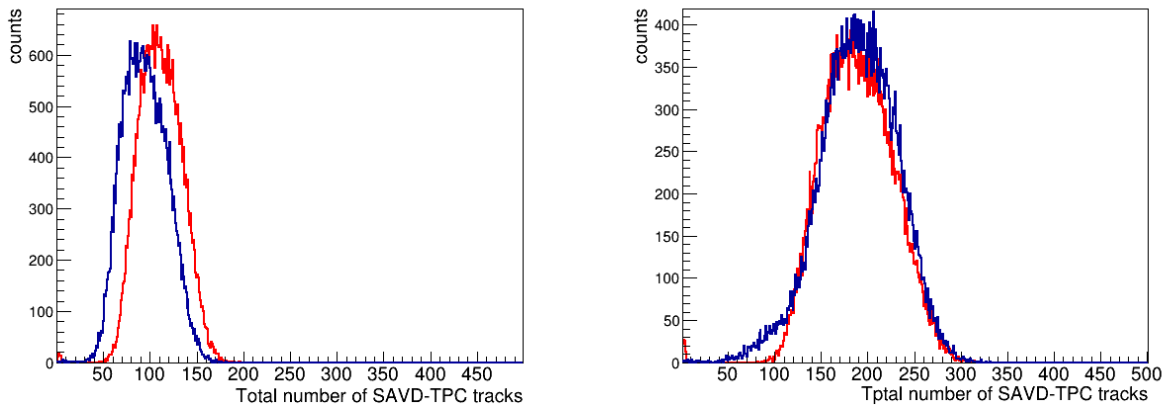

Figure 8.11: The distribution of number of reconstructed SAVD-TPC tracks for reconstructed real (blue line) and simulated (red line) Xe+La (left pad) and Pb+Pb (right pad) at 150A GeV/c events.

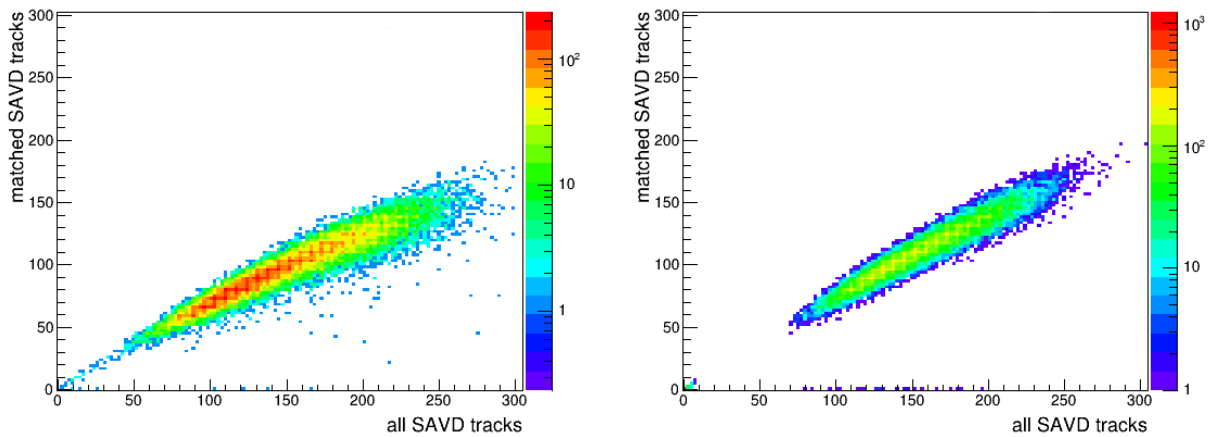

Figure 8.12: Matched SAVD track multiplicity versus SAVD track multiplicity. Plot was done for reconstructed real (left pad) and simulated (right pad) Xe+La at 150A GeV/c data. For real data event selection is applied, thus the difference with Fig 4.14.

about 75 % of SAVD tracks have match to TPC tracks forming SAVD-TPC tracks. (see Chapter 4). The fact, that plot for real data has region of low track multiplicity (contrary to simulated events) might signify, that the event selection used in real data is not able to select 20% central events, but also accepts lower centrality.

Similarly to real data, the SAVD-TPC track matching the Δy versus y distributions were obtained according to the procedure described in Chapter 4. The example of such distribution obtained for simulated data is shown in Fig. 8.13. Left pad of Fig. 8.13 shows the Δy distribution in a selected y slice. The distribution was fitted with Gaussian, and its width was found to be smaller then analogous for real data (Fig. 4.12) due to perfect drift velocity v_{drift}, which is not the case for real data data.

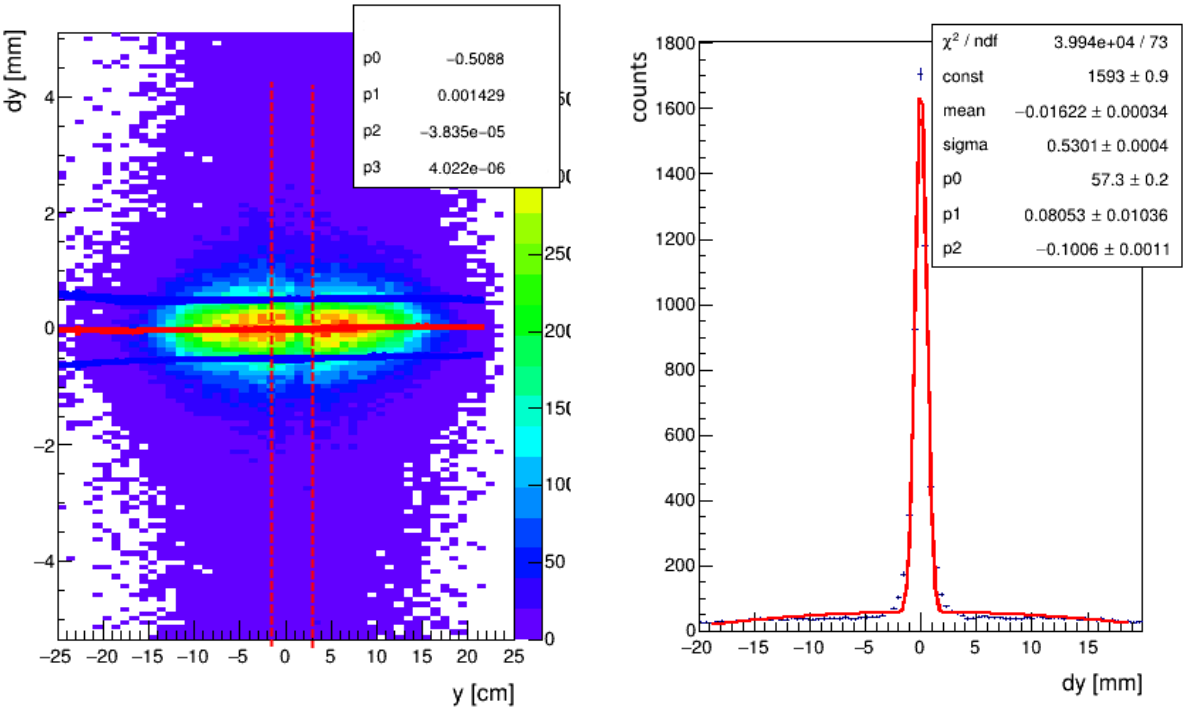

Figure 8.13: Left pad : Difference in y coordinate of SAVD and TPC tracks (Δy) versus y at the matching plane for *Jura* - *Jura* track combination. The histogram is fitted with Gaussian in each y slice and the mean values are marked as red dots. The Δy versus y dependency were fitted with third order polynomial (red line on plots). The blue lines indicate range of $\pm$ 3σ around the mean values. The parameters of the fit are indicated on plots. Right pad: example of the projection of distribution of Δy versus y onto the Δy coordinate for -1.5cm $< y <$ 3.2 cm interval, indicated by dotted lines on the right pad. See the text for details.

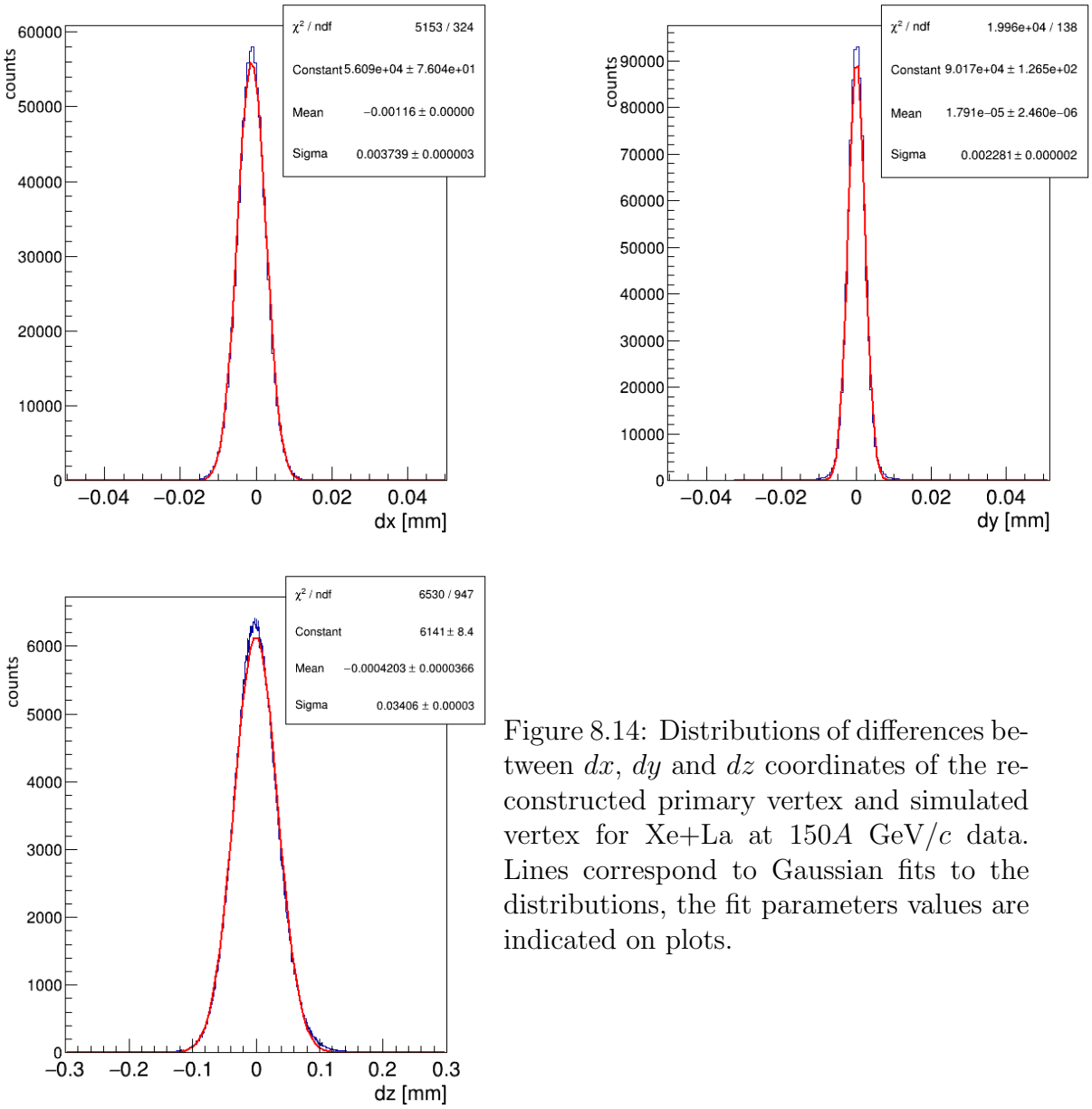

Figure 8.14: Distributions of differences between dx, dy and dz coordinates of the reconstructed primary vertex and simulated vertex for Xe+La at $150A$ GeV/c data. Lines correspond to Gaussian fits to the distributions, the fit parameters values are indicated on plots.

Primary and secondary vertex resolution

For simulated data it is possible to obtain reconstructed primary vertex resolution by comparing the simulated and reconstructed positions of vertices. The obtained distributions are shown in Fig. 8.3.1 (the differences between coordinates of the reconstructed primary vertex and simulated vertex are noted as dx, dy and dz). The sigmas of these distributions correspond to the primary vertex resolution and are equal to 3.7 μm, 2.3 μm, 34 μm for x, y and z coordinates, respectively, which is similar to the resolution obtained from real data using the two sub-samples (see Fig. 8.10).

Similarly one can obtain the spatial resolution for D^0 and $\overline{D^0}$ secondary vertices by plotting the difference dx, dy, dz of the coordinates of the reconstructed secondary vertex position and the one defined in GEANT4 simulations. The obtained distributions are shown in Fig. 8.3.1. The sigma of these distributions determine the primary vertex resolution to be 20 μm, 11 μm, 170 μm for x, y and z coordinates, respectively.

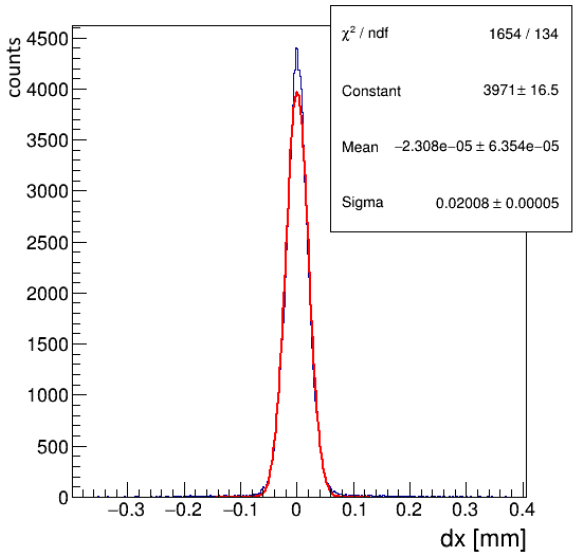

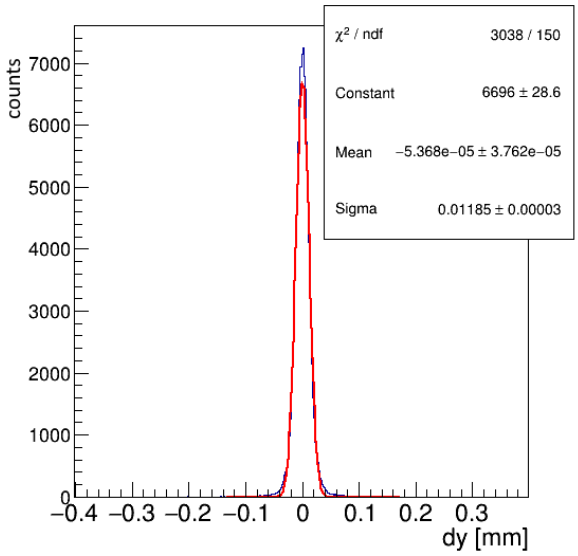

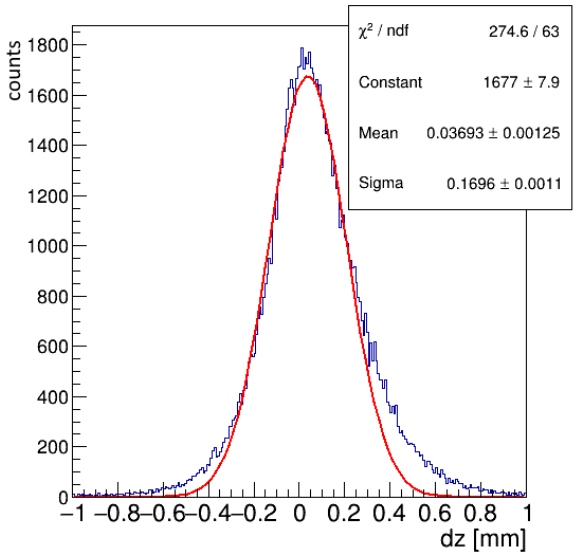

Figure 8.15: Distributions of differences between dx, dy and dz coordinates of the reconstructed secondary vertices and simulated vertices for Xe+La at $150A$ GeV/c data. Lines correspond to Gaussian fits to the distributions, the fit parameters are indicated on plots.

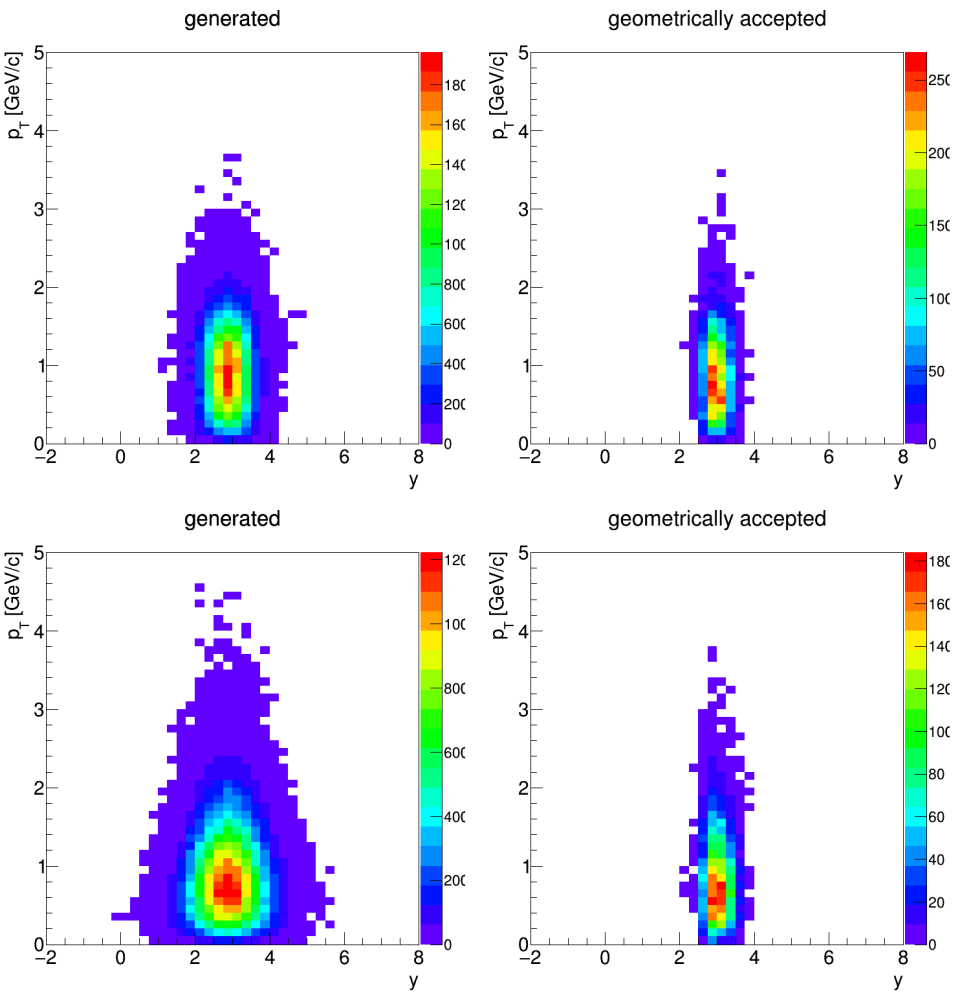

Figure 8.16: Rapidity – transverse momentum spectra of D^0 + $\overline{D^0}$ mesons for 20% of the most central Xe+La collisions at 150A GeV/c according to AMPT (upper pads) and PHSD (bottom pads) predictions. Left pads show the generated phase space and right pads show geometrically accepted phase space. The plots are done for 1M generated D^0 + $\overline{D^0}$ in π and K decay channel.

In summary of this Section, it was shown that reasonable agreement between the real data and the simulations was reached in order to perform open charm analysis study.

8.3.2 Geometrical acceptance

In order to obtain the correction factor for the geometrical acceptance of the detector system the dedicated simulation study was performed. Only generated D^0 and $\overline{D^0}$ according to the phase space from AMPT and PHSD event generator were used as the input for GEANT4 simulation chain. In this study no corrections for sensor efficiency was applied. Fig. 8.16 and Fig. 8.17 present the phase space distribution in transverse momentum – rapidity coordinates for generated D^0 and $\overline{D^0}$ and and for those D^0 and $\overline{D^0}$, that passed into the detector acceptance (i.e. leave at least three hits in SAVD and at least 10 hits in TPC, which means, that such track is reconstructable and can be used for further analysis).

The simulation study for Xe+La collisions shows, about 7.8% and 5.9% acceptance of

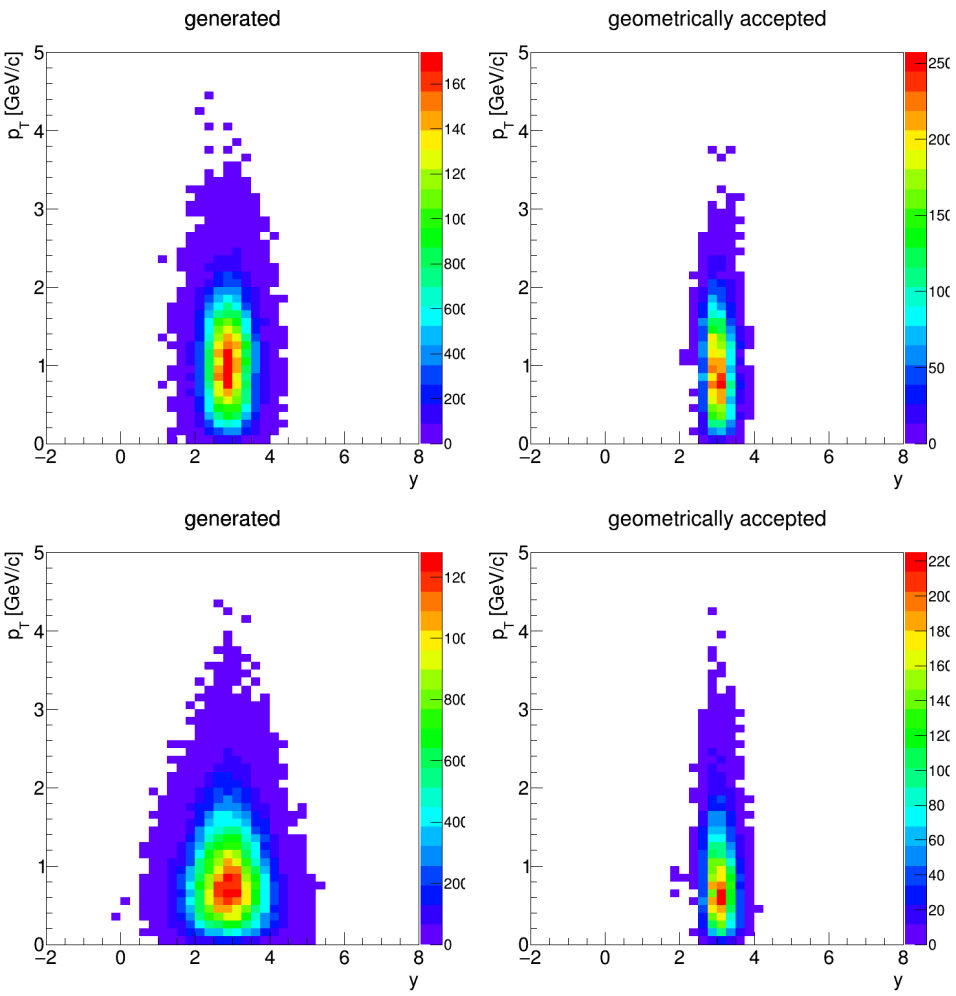

Figure 8.17: Rapidity – transverse momentum spectra of D^0 + $\overline{D^0}$ mesons for 20% of the most central Pb+Pb collisions at 150A GeV/c according to AMPT (upper pads) and PHSD (bottom pads) predictions. Left pads show the generated phase space and right pads show geometrically accepted phase space. The plots are done for 1M generated D^0 + $\overline{D^0}$ in π and K decay channel.

$D^0 + \overline{D^0}$ in π and K decay channel for AMPT and PHSD phase space, receptively.

Analogues study for Pb+Pb collisions show that, about 8.4% (AMPT) and 6.8% (PHSD) of all generated $D^0+\overline{D^0}$ in the π and K decay channel are geometrically accepted by the detector.

8.3.3 Efficiency of detector system

Matching of simulated and reconstructed tracks

After the simulated event is reconstructed the matching between simulated and reconstructed tracks is performed. Since there it is not possible to directly obtain one to one correspondence between simulated and reconstructed tracks (due to the effects that hits from different particles can be merged to one cluster, two close to each other simulated tracks can be reconstructed as one track, etc.) the dedicated procedure was developed.

As the first step of this procedure GEANT hits are matched to reconstructed clusters. For each cluster the algorithm is searching for the nearest hit on the given SAVD station,

or on the z plane for TPCs. The TPC cluster matching procedure was not developed within this thesis and was available from the NA61/SHINE software toolkit. The cluster matching efficiency, determined by number of clusters matched to hits versus total number of clusters, was found to be 94% (Xe+La) and 92% (Pb+Pb) for TPC and $> 99.9\%$ for SAVD. The slightly worse cluster matching efficiency for Pb+Pb data is due to higher track multiplicity as compare to the Xe+La case.

As the second step of the matching procedure the best matches is searched between simulated and reconstructed tracks depending on number of common hit-cluster combinations. Same as for clusters, the algorithm is looking for given reconstructed track at all clusters and checking for hits, that are associated with them. Then, the algorithm is checking all simulated tracks that, are associated with these clusters. Since the analysed events are having high track multiplicities, often several simulated tracks show common points with given reconstructed track. Thus, from these matching candidates for the given reconstructed track the best one is selected based on the highest number of the common hit-cluster points.

Since the procedure was mostly develop for open charm analysis, it is the most crucial to match tracks which have SAVD clusters. Thus, the algorithm searches for the best match for reconstructed track (which has SAVD and TPC clusters) depending on:

- If the simulated track also has SAVD hits (since position resolution of SAVD is significantly better then of TPC);
- If the simulated track has more common points with reconstructed track then other simulated tracks.

Within this procedure some of the reconstructed tracks do not have matched simulated tracks when number of common points with any of simulated tracks is too low, this is might happen for very short tracks which don't have enough associated clusters due to inefficiency of the cluster reconstruction or matching procedure or due to fake tracks. Also, in a few % of the cases a single simulated track is assigned to two or more reconstructed tracks. This usually happens for high track density region.

For the same reason the incorrect matches are possible which might slightly affect the open charm signal results (however wrong matches will not influence the invariant mass spectra in the vicinity of the signal peak).

The matching information could be also used for identification of the reconstructed particles since the dE/dx information is not available. Thus, matching allows to identify the reconstructed tracks by assigning them PID information from the matched simulated tracks. This allows to look for the open charm decay tracks separately from the other track in the event and study features related to the open charm signal only.

Reconstruction efficiency

The simulation allows for testing of the reconstruction performance. To test the reconstruction efficiency of SAVD the dedicated study was performed in which detection efficiencies of the sensors were set to 100% (to exclude the effect of the sensor inefficiency). The efficiency was determined as the ratio between number of the reconstructed tracks and number of the simulated tracks in the SAVD acceptance (that have 3 or more SAVD hits).

Fig. 8.3.3 shows the dependence of the efficiency versus track momenta. It is seen, that the efficiency is close to 100% for higher track multiplicity, however it starts to drop for tracks with momentum <1 GeV/c. The study of such tracks showed, that such low momentum tracks have large curvature in the SAVD region (the magnetic field there is low, but not zero). Thus such tracks can't be reconstructed within the strait line model of the combinatorial stage of the reconstruction as well as during the Hough Transform stage they end up in the different bins of the Hough space.

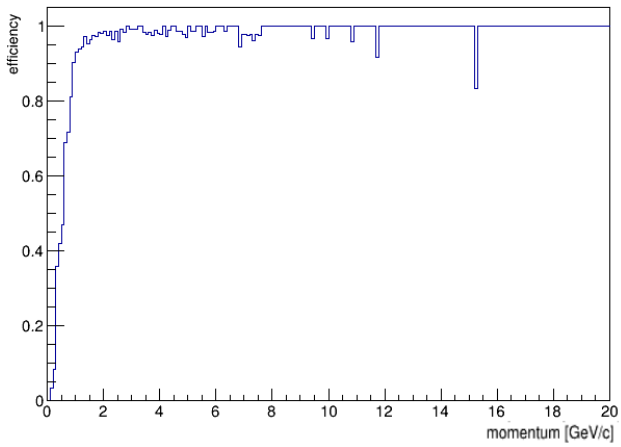

Figure 8.18: The SAVD reconstruction efficiency versus track momenta assuming fully efficient sensors for Xe+La at 150A GeV/c.

The overall reconstruction efficiency for the whole detector was determined as the ratio between number of the reconstructed SAVD-TPC tracks and number of the simulated tracks in the SAVD and TPC acceptance (that have 3 or more SAVD hits and 10 or more TPC hits). Fig. 8.3.3 shows the distribution of number of common points for reconstructed and simulated tracks, for SAVD only (left pad) and for SAVD+TPC combined tracks (bottom pad).

It is seen, that most of the SAVD tracks have 3 or 4 common points. The distribution for total number of common points (SAVD+TPC points) slightly resembles the distribution of the number of the TPC clusters (Fig. 8.6). The peak at low number of common points corresponds to fake matches (it is seen that it is reduced when selecting the best match – magenta line) and very short tracks – when applying requirements on having both SAVD and TPC points this region disappears (green line).

Fig. 8.3.3 shows the total reconstruction efficiency (also taking into account realistic efficiency of the SAVD sensors) for Xe+La and Pb+Pb data. The average efficiency (for momenta >1 GeV/c) is $\approx$ 86% for Xe+La data and $\approx$ 85% for Pb+Pb data. The 2D distributions of the efficiency in $y_\pi - p_T$ coordinates (assuming pion mass when calculating rapidity) are shown in Fig. 8.21.

8.4 Simulation results

8.4.1 Optimisation of background suppression cuts

As was discussed in Chapter 7, in order to suppress the background on the invariant mass spectra several cuts were applied: p_T; the track impact parameter d; DCA; the longitudinal distance between the D^0 decay candidates and the interaction point V_z; the

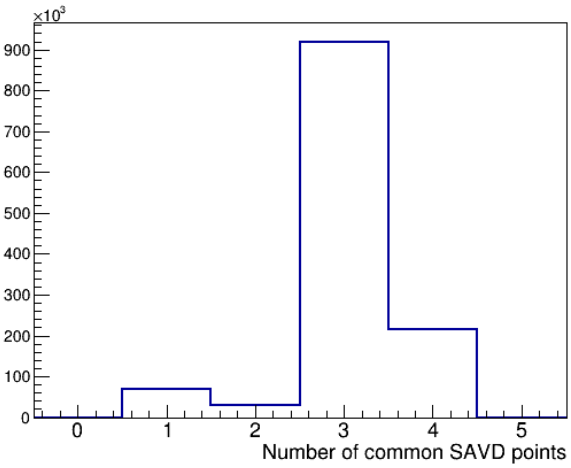

Figure 8.19: The distribution of the number of common points for reconstructed and simulated tracks. Left pad: only SAVD common points, bottom pad: all common points (SAVD+TPC), the black line shows distribution for all possible matching candidates, magenta – for the beast matching candidate and green – for accepted candidates (that fulfil requirement of also having SAVD points). The distributions are plotted for Xe+La at 150A GeV/c.

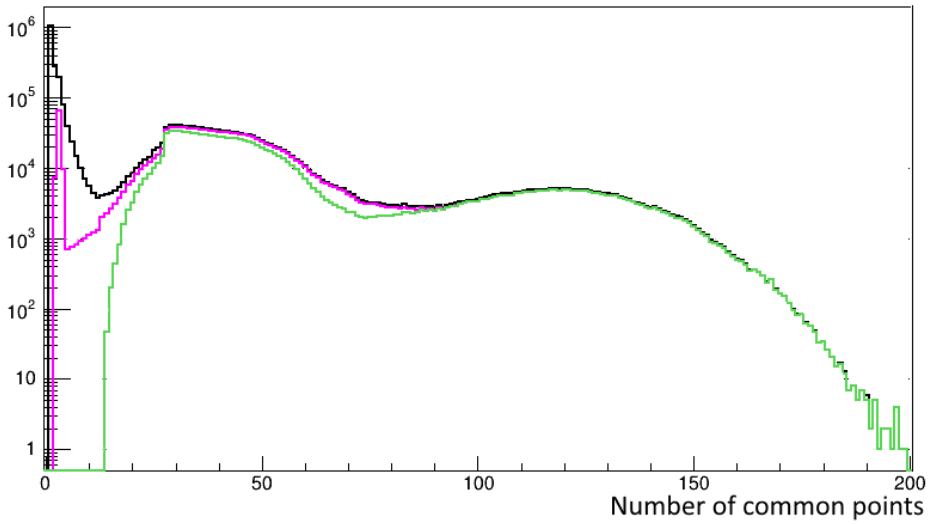

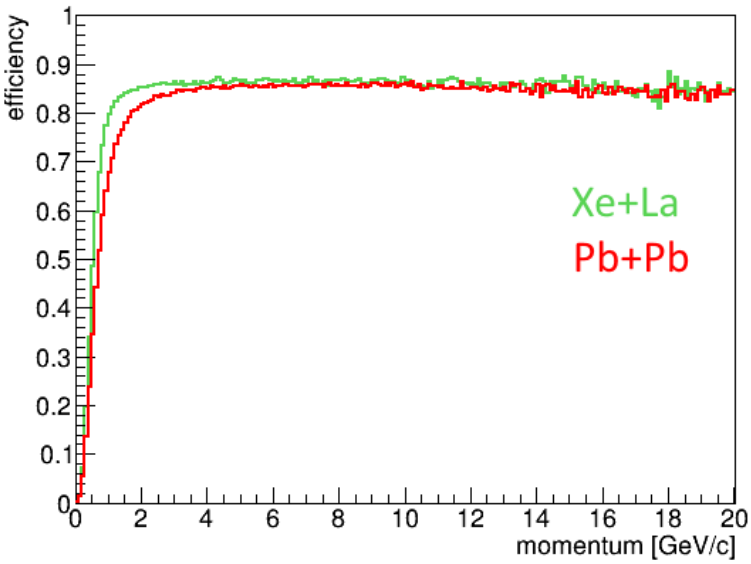

Figure 8.20: The reconstruction efficiency versus track momenta for Xe+La at 150A GeV/c (green line) and Pb+Pb at 150A GeV/c (red line).

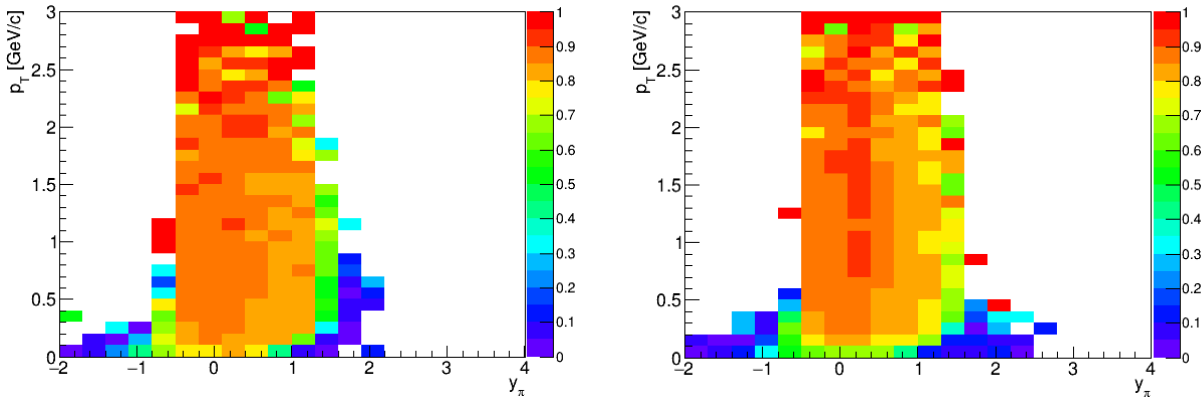

Figure 8.21: The reconstruction efficiency in $y_\pi - p_T$ coordinates for Xe+La (left pad) and for Pb+Pb (right pad) at 150A GeV/c.

parent impact parameter D. In order to choose cut values that maximise the signal to noise ratio (SNR) of the $D^0 + \overline{D^0}$ peak, the dedicated simulation study was performed.

As it was mentioned the MC simulations were performed for events enriched with 5 $D^0 + \overline{D^0}$ per events, and also the branching ratio for the $\pi + K$ decay channel in GEANT4 was adjusted to be 100% for this decay channel. Note, that it was checked, that the registered yield in case of several D mesons in event proportional to initial yield of D mesons, as well as the other decay channels don't contribute in the signal in the invariant mass distribution. Thus, initial yield per MC event corresponds to ≈ 130 $D^0 + \overline{D^0}$ per real event. However, in the performed simulation studies the yield was adjusted to correspond to more realistic case: this was done by randomly removing D mesons from the MC event according to selected probability.

For selection of the values for background suppression cuts the yield was adjusted to be according to the SMES predictions (see below): thus, the signal on the invariant mass spectra was clear and could be fitted the Gaussian. The scan over the cut values was performed in order to obtain the largest value of SNR. The obtained values were used for real data analysis and are listed in Table 7.2 for Xe+La and Pb+Pb at 150A GeV/c data. The distributions of the cut variables for all pairs and for signal pairs are shown in Fig. 7.4. Also, the ratio of the signal and the background versus the cut variables are shown in Fig. 8.22, on the same plots the shape distribution for the signal component is indicated (red line, not to scale).

Fig. 8.23 shows the distribution of $D^0 + \overline{D^0}$ mesons depending on the distance between the primary vertex and the secondary vertex V for different applied cuts. It is seen that the p_T, DCA and D cuts contribute in similar way to the suppression over the studied range of V. However, the d cut is noticeably reducing the registered $D^0 + \overline{D^0}$ yield for $V < 800$ μm. Nevertheless, the cut on d is also significantly reducing the background by removing the primary tracks.

8.4.2 Geometrical cuts

It was observed that due to the opening angle of the D^0 decay it is more probable, that the daughter tracks will will often hit different arms of SAVD (scheme is shown in Fig. 7.5). The comparison is shown in Fig. 8.24). It is seen that the SNR is much higher in case of "different arms" then in "same arm" configuration. Thus, to improve the SNR the pairs

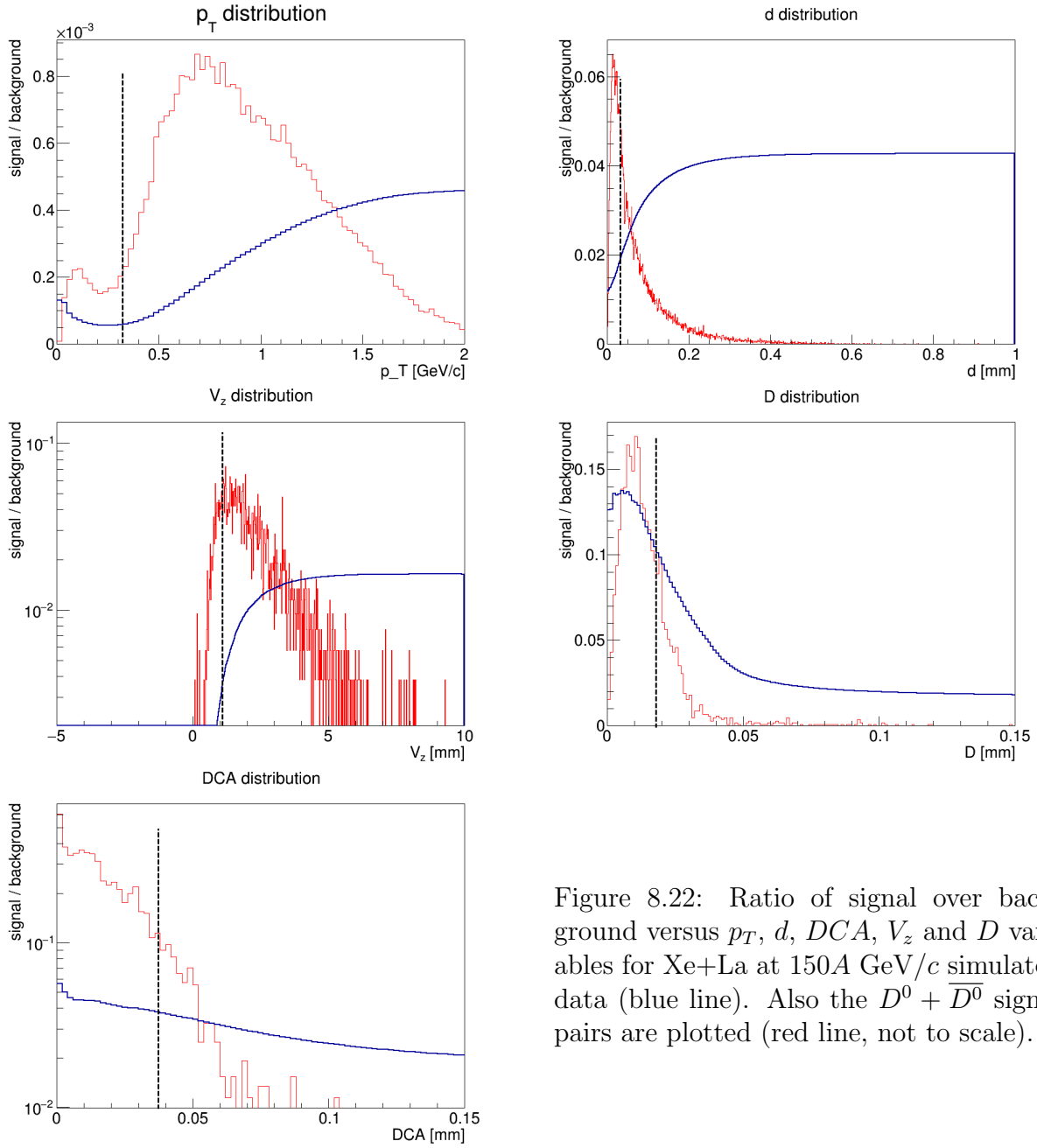

Figure 8.22: Ratio of signal over background versus p_T, d, DCA, V_z and D variables for Xe+La at $150A$ GeV/c simulated data (blue line). Also the $D^0 + \overline{D^0}$ signal pairs are plotted (red line, not to scale).

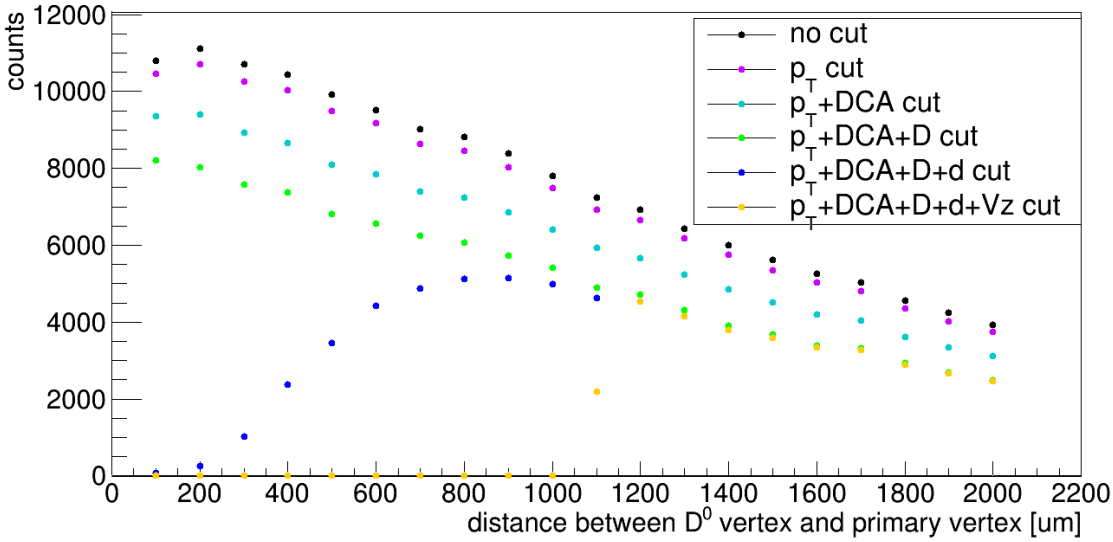

Figure 8.23: Distribution of $D^0 + \overline{D^0}$ mesons depending on the distance between the primary vertex and the secondary vertex V_z for simulated Xe+La collisions at $150A$ GeV/c. Different colours correspond to different applied cuts (indicated on plot).

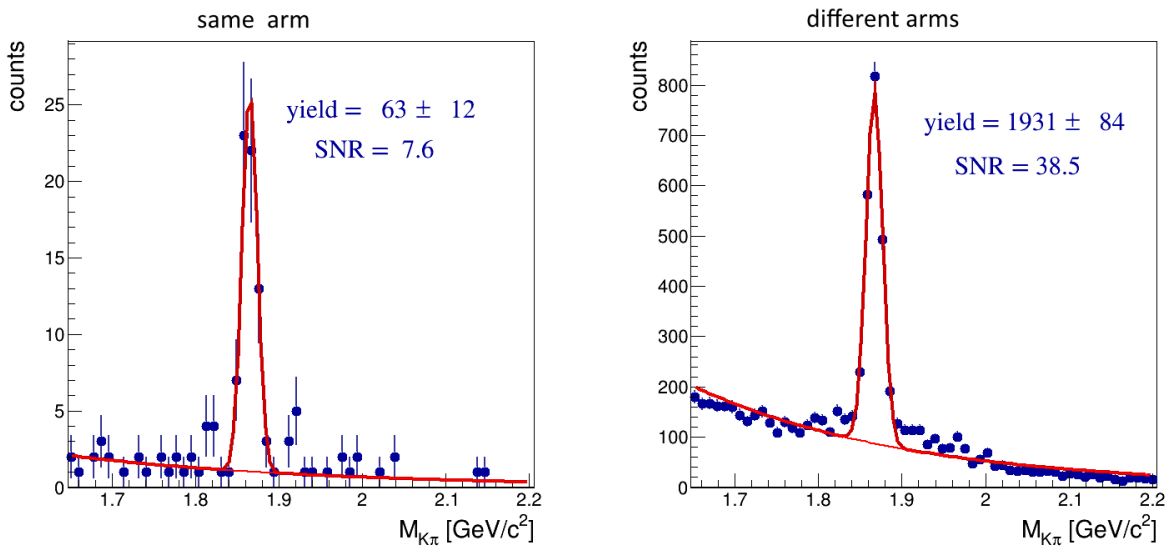

Figure 8.24: Invariant mass distribution of unlike charge sign π, K decay track candidates for Xe+La at $150A$ GeV/c simulated data for "same arm" (left pad) and "different arms" (right pad) configurations.

which are registered within the same arm are rejected. Note, that the broad structure around the peak seen in the invariant mass spectrum in the left pad of Fig. 8.24 is due to wrong mass association for the true D0 daughters.

Furthermore, there is a noticeable probability, that at least one of D^0 daughters will miss the fist station of SAVD. Fig. 8.4.2) shows the invariant mass distributions for three different cases:

- When both daughter tracks hit the first SAVD station;
- When one of the tracks missed the first station and leave its first hit on the second

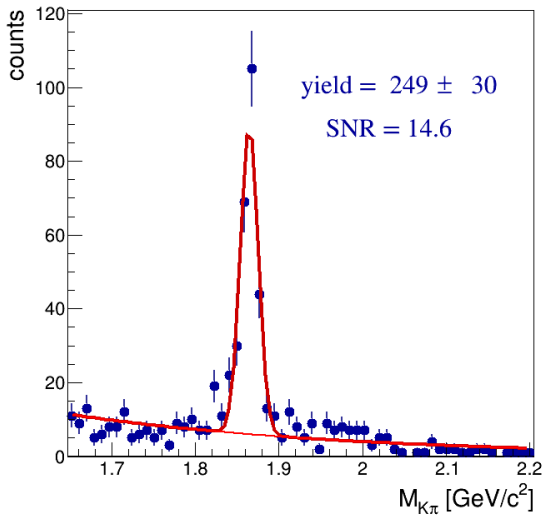

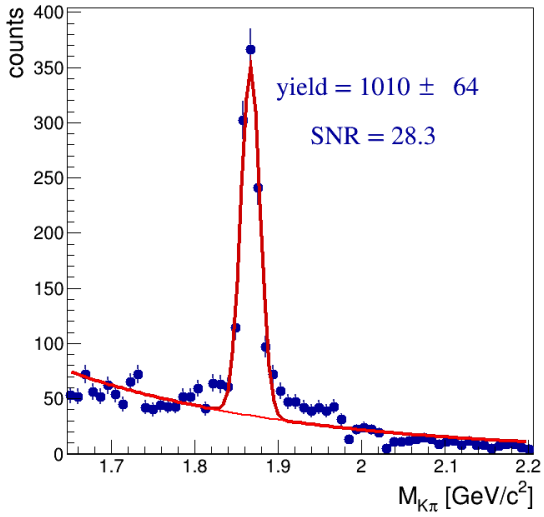

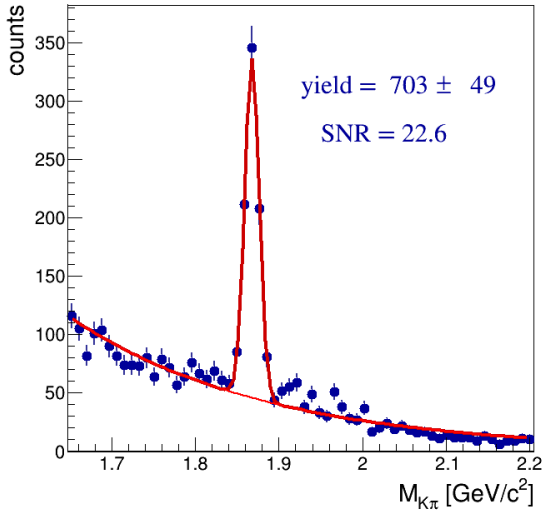

Figure 8.25: Invariant mass distribution of unlike charge sign π, K decay track candidates for "different arms" configuration for Xe+La at 150A GeV/c simulated data. The the distributions are plotted for cases when both daughter tracks have hit on the first SAVD station (upper left pad), when one of the tracks miss the first station (upper right pad) and when both of the tracks miss the first station (bottom pad).

station;

- When both of the tracks miss the first station.

It is seen, that the SNR for the last two cases is higher then for the first case. Thus, for the analysis only the track pairs in which one or both tracks have the first hit on the second station of SAVD were considered.

Fig. 8.26 and Fig. 8.27 show the invariant mass distributions of unlike sign charge daughter candidates and the background reduction with the subsequent application of the discussed above cuts. After application of all background suppression cuts with the optimised cut values the background in became suppressed by a factor of 10^5 while the signal is suppressed by a factor of 5 for both AMPT and PHSD phase space distribution of $D^0 + \overline{D^0}$.

8.4.3 Correction of $D^0 + \overline{D^0}$ yield

Though the acceptance and the efficiency of the detector were studies separately, the final correction values for $D^0 + \overline{D^0}$ were calculated together taking into account all described

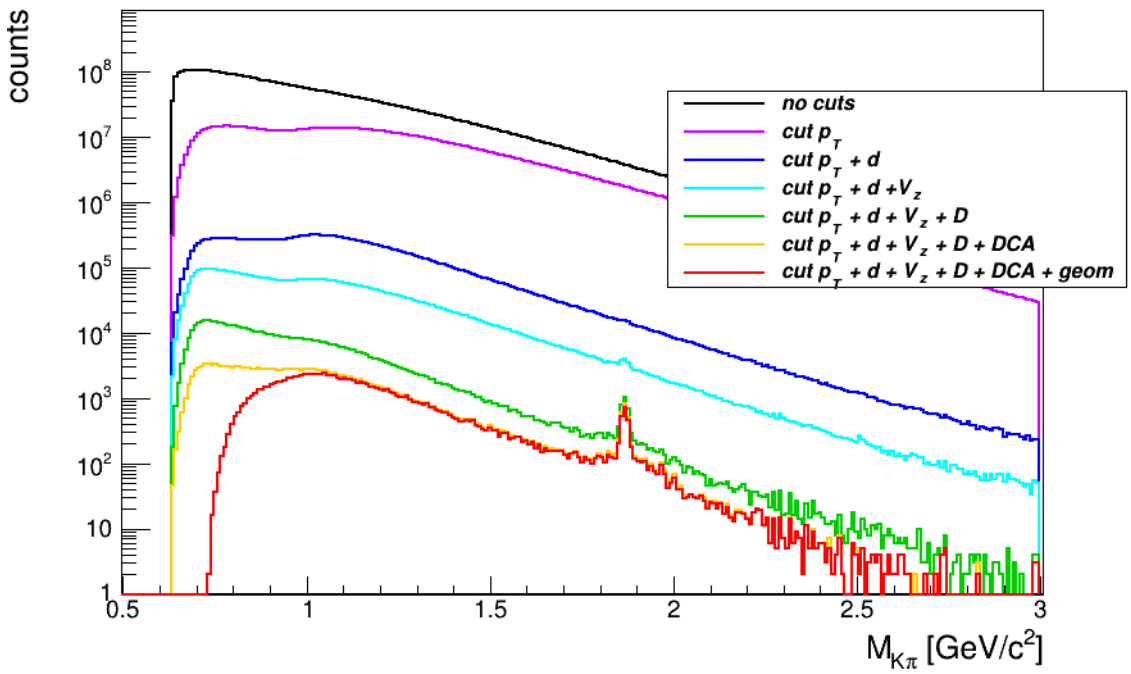

Figure 8.26: Invariant mass distribution of unlike charge sign π, K decay track candidates for simulated Xe+La collisions at 150A GeV/c (assuming the AMPT phase space and the SMES yield for $D^0 + \overline{D^0}$). Different colours correspond to different cuts applied (indicated on plot).

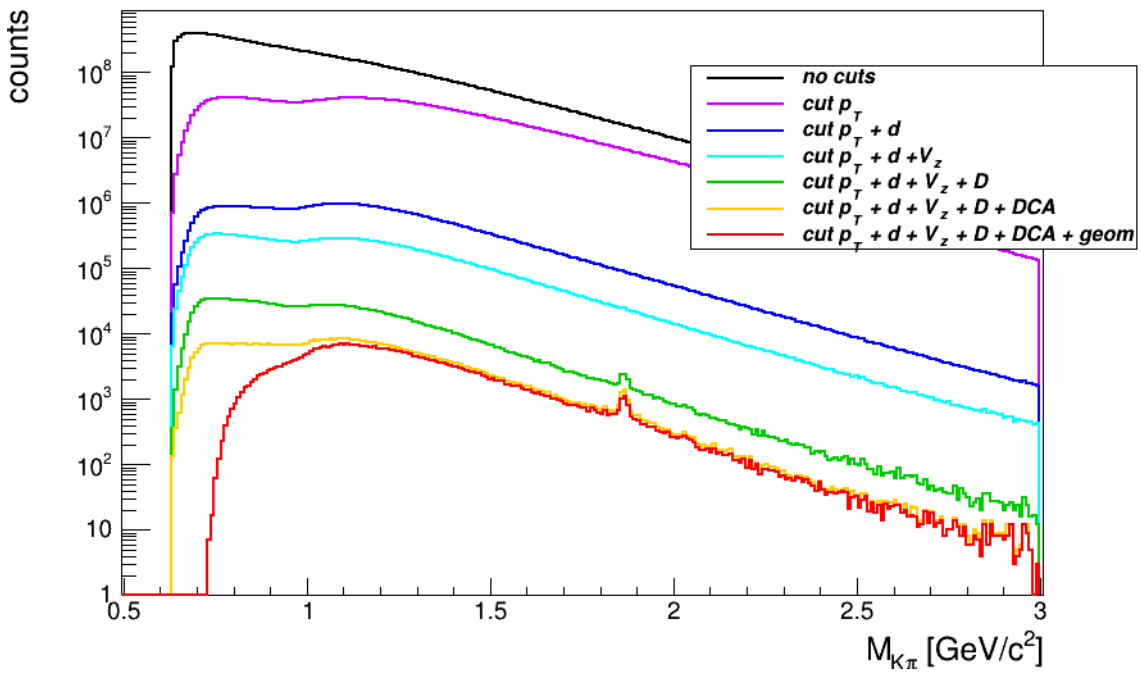

Figure 8.27: Invariant mass distribution of unlike charge sign π, K decay track candidates for simulated Pb+Pb collisions at 150A GeV/c (assuming the AMPT phase space and the SMES yield for $D^0 + \overline{D^0}$). Different colours correspond to different cuts applied (indicated on plot).

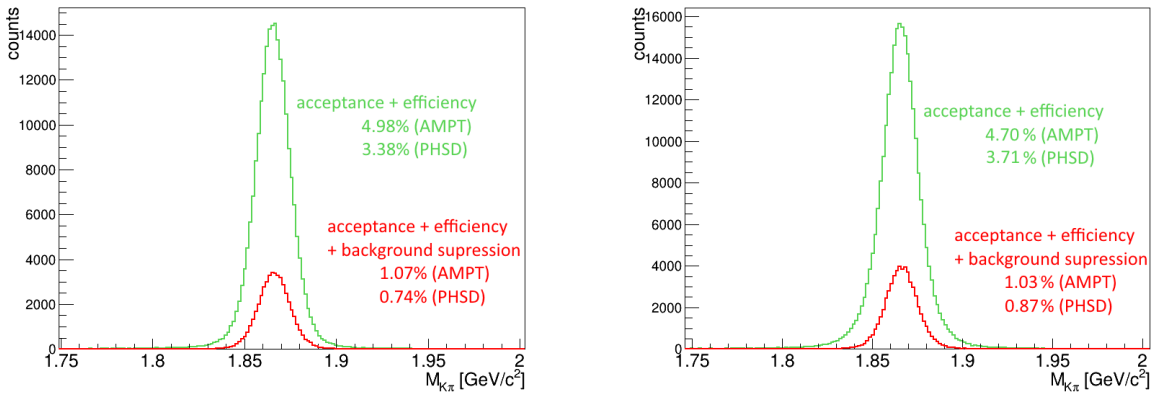

Figure 8.28: Invariant mass distribution of $D^0 + \overline{D^0}$ (assuming AMPT phase space) for simulated Xe+La (left pad) and Pb+Pb (right pad) collisions at 150A GeV/c. Green line represents the distribution for all reconstructed $D^0 + \overline{D^0}$, red line represents $D^0 + \overline{D^0}$ after applying the background suppression cuts.

	Correction factor for Xe+La at 150A GeV/c AMPT / PHSD	Correction factor for Pb+Pb at 150A GeV/c AMPT / PHSD
acceptance + efficiency	4.98% / 3.38%	4.70% / 3.71%
+ background suppression cuts	1.07% / 0.74%	1.03% / 0.87%

Table 8.1: Information about the corrections for the $D^0 + \overline{D^0}$ signal for Xe+La and Pb+Pb at 150A GeV/c data.

above effects. This was done by obtaining the registered D meson yield and comparing it to amount set initially in the generated events. Fig. 8.28 shows invariant mass distributions of only signal pair combinations, that were registered in the detector (left pads) and that passes background suppression and geometrical cuts (right pads).

Table 8.4.3 presents the correction values for Xe+La and Pb+Pb at 150A GeV/c data assuming signal distribution according to the AMPT and the PHSD models. The indicated corrections were used for calculation of the total yield of $D^0 + \overline{D^0}$.

8.4.4 Expected signal according to different models

Obtained from real data the invariant mass distribution for $D^0 + \overline{D^0}$ candidates were compared to the distributions obtained in the simulation study with the yield according three different model expectations: PHSD, the NA50/NA60 predictions and SMES.

As it was mentioned earlier, as the input for the GEANT4 simulations the mixed events were created: each generated AMPT event (background) was enriched with 5 D^0 or $\overline{D^0}$ mesons distributed according to the AMPT or PHSD phase space distribution. For both cases, about 1M events were simulated and reconstructed. To obtain the results for different yield predictions in the reconstructed events D^0 or $\overline{D^0}$ were randomly discarded according to the predictions. Also, in order to obtain plots for similar statistics as for real data the background on the invariant mass spectra was parametrised with the exponential function (see Chapter 7). This parametrization was then used for random generation of the background with the desired statistics. Thus, the plots shown in Fig. 8.29 and Fig. 8.30

could be directly compared to those obtained for real data (Fig. 7.3 and Fig. 7.3).

Fig. 8.29 and Fig. 8.30 present the invariant mass distribution of the reconstructed simulated $D^0 + \overline{D^0}$ distributed according to the AMPT phase space. The distributions are plotted for the $D^0 + \overline{D^0}$ yield predicted by PHSD (left pads), the NA50/NA60 (middle pads) and SMES (right pads). The values of the yields are discussed below. It is seen, that in case of PHSD the signal is not visible, while in case of SMES the $D^0 + \overline{D^0}$ is well pronounced and the SNR is high. In case of the predictions by the NA50/NA60 one obtains the weak indication of the signal, which corresponds to the result obtained for the real data. The detailed discussion of the result are presented in Chapter 9.

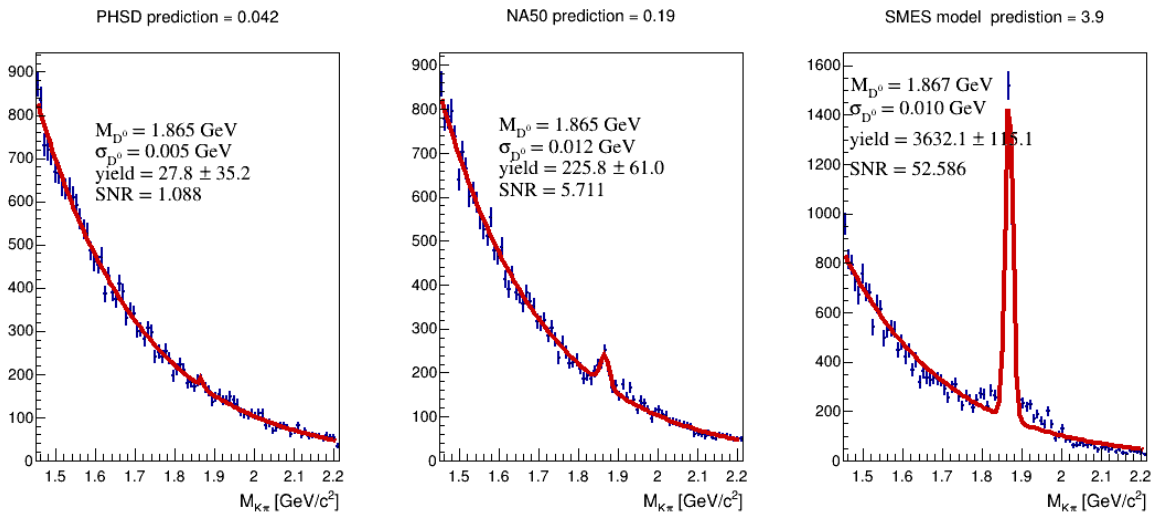

Figure 8.29: Invariant mass distribution of reconstructed simulated $D^0 + \overline{D^0}$ distributed according to the AMPT phase space. The total $D^0 + \overline{D^0}$ yield is predicted by PHSD (left pad), the NA50/NA60 (middle pad) and SMES (right pad). The red line represents the Gaussian fit. The distributions are plotted for Xe+La at 150A GeV/c data.

Expected signal according to the PHSD predictions

According to the results based on PHSD event generator, the $D^0 + \overline{D^0}$ yields for 20% central Xe+La and Pb+Pb collisions are predicted to be

$$N(D^0 + \overline{D^0})_{Xe+La} \approx 0.042,$$
$$N(D^0 + \overline{D^0})_{Pb+Pb} \approx 0.079.$$

Expected signal according to the NA50/NA60 predictions

As it was discussed in Chapter 2 the NA50/NA60 Collaboration found, that the pQCD based model cannot describe the dimuon invariant mass spectrum between ϕ and J/ψ peaks in central Pb+Pb collisions (Fig. 2.5). However, the spectrum can be reproduced when the contribution from open charm Dalitz decays is scaled up by a factor of about 3. Thus, based on the pQCD inspired HSD model (Fig. 2.7), the $D^0 + \overline{D^0}$ yield is predicted to be $N(D^0 + \overline{D^0})_{Pb+Pb} \approx 0.6$.

The predictions for the yield for 20% of the central Pb+Pb and Xe+La collisions can be obtained by re-scaling the result for central Pb+Pb by number of binary collisions $\langle N_{coll} \rangle$ (as predicted in dynamical approach) or by number of participants $\langle N_{part} \rangle$ (as

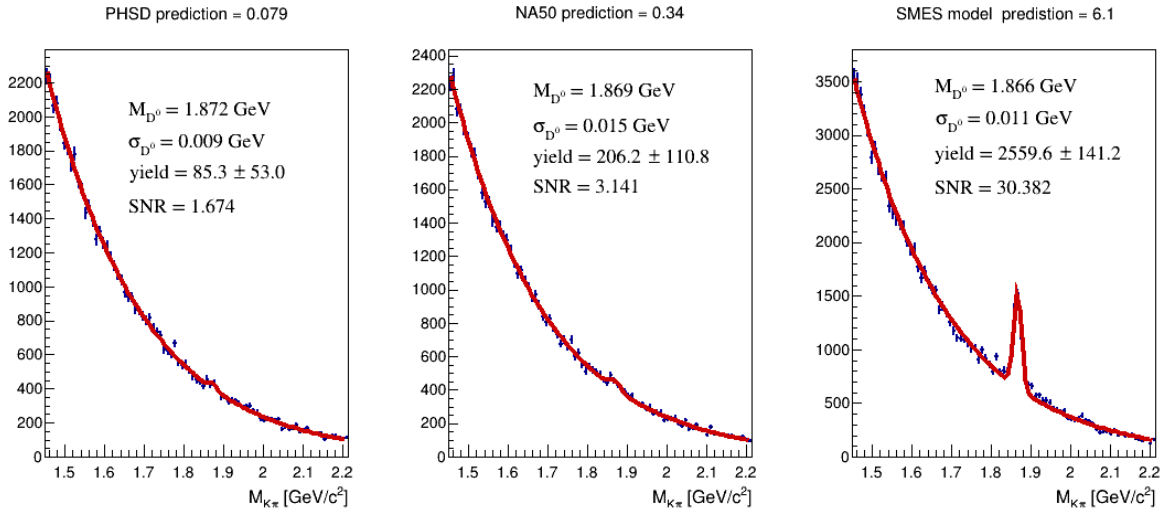

Figure 8.30: Invariant mass distribution of reconstructed simulated $D^0 + \overline{D^0}$ distributed according to the AMPT phase space. The total $D^0 + \overline{D^0}$ yield is predicted by PHSD (left pad), the NA50/NA60 (middle pad) and SMES (right pad). The red line represents the Gaussian fit. The distributions are plotted for Pb+Pb at 150A GeV/c data.

predicted in statistical approach). Thus, assuming scaling of the open charm yields with N_{coll} and taking into account that: $\langle N_{coll} \rangle = 331.1$ for 20% of the most central Xe+La collisions, $\langle N_{coll} \rangle = 598.8$ for 20% of the most central Pb+Pb collisions and $\langle N_{coll} \rangle = 1050$ for central Pb+Pb collisions, the estimated $D^0 + \overline{D^0}$ yields for 0-20% centrality are:

$$N(D^0 + \overline{D^0})_{Xe+La,dynamicalscaling} \approx 0.19,$$
$$N(D^0 + \overline{D^0})_{Pb+Pb,dynamicalscaling} \approx 0.34.$$

On the other hand, assuming assuming scaling with N_{part} and taking into account that $\langle N_{part} \rangle = 173.7$ for 20% of the most central Xe+La collisions, $\langle N_{part} \rangle = 272.5$ for 20% of the most central Pb+Pb collisions and $\langle N_{part} \rangle = 414$ for central Pb+Pb collisions the predicted yields of $D^0 + \overline{D^0}$ for 0-20% centrality are:

$$N(D^0 + \overline{D^0})_{Xe+La,statisticalscaling} \approx 0.25,$$
$$N(D^0 + \overline{D^0})_{Pb+Pb,statisticalscaling} \approx 0.39.$$

Expected signal according to the SMES predictions

The SMES calculations predict for central Pb+Pb collisions at 158A GeV/c $\langle c\bar{c} \rangle$ to be about 17 [20]. After scaling this value from 158A GeV/c to 150A GeV/c according to Fig. 2.3 (left pad) [24] and number of participants one gets $\langle c\bar{c} \rangle \approx 6.3$ for Xe+La and $\langle c\bar{c} \rangle \approx 9.9$.

These prediction of $\langle c\bar{c} \rangle$ can be recalculated to $N(D^0 + \overline{D^0})$ assuming, that 62% of total charm hadronizes to D^0 and $\overline{D^0}$ mesons (according to PHSD, Fig. 2.2). Thus, the $D^0 + \overline{D^0}$ yield is predicted to be

$$N(D^0 + \overline{D^0})_{Xe+La} \approx 3.9,$$
$$N(D^0 + \overline{D^0})_{Pb+Pb} \approx 6.1.$$

Note, that similar estimated calculations of the $D^0 + \overline{D^0}$ yield provided in [9] assumed, that about one third of charm converts to D^0 and $\overline{D^0}$ mesons based on p+p data [83].

Chapter 9

Discussion and outlook

9.1 Discussion of the obtained results

The obtained summed yield of the D^0 and $\overline{D^0}$ mesons can be compared to discussed earlier model predictions, namely: the PHSD model, the NA50/NA60 estimation, and the SMES model. A quantitative comparison of the results to the models is presented in Table 9.1. An error of at least 20% should be assigned to the model estimations, arising from several uncertainties in the calculations.

Prediction	Xe+La at 150A GeV/c	Pb+Pb at 150A GeV/c
PHSD	0.042	0.079
NA50/NA60 (dynamical scaling)	0.19	0.34
NA50/NA60 (statistical scaling)	0.25	0.39
SMES	3.9	6.1
NA49 upper limit (98% CL)		1.5
yield (AMPT phase space)	0.10 ± 0.03	0.33 ± 0.18
yield (PHSD phase space)	0.15 ± 0.05	0.39 ± 0.21
upper limit (98% CL) (AMPT)	0.17	0.70
upper limit (98% CL) (PHSD)	0.25	0.82

Table 9.1: The expected yield of D^0+$\overline{D^0}$ for three predictions: the PHSD model, the NA50/NA60 estimation, the SMES model; the estimated upper limit by the NA49. On the bottom of the table, the obtained experimental results and upper limits are presented for two different phase space distributions of $D^0 + \overline{D^0}$ according to the AMPT and the PHSD models.

The PHSD predictions on $D^0 + \overline{D^0}$ yields are about factor 2-4 smaller as compare to the experimental result obtained in this work. On other hand, the obtained yields for Xe+La and Pb+Pb collisions show good correspondence with the NA50/NA60 estimations, assuming that $D^0 + \overline{D^0}$ yield was scaled up relative to the HSD model: the values overlap within the error bar. These two results might suggest that enhancement of open charm is necessary to describe the data results. Thus would mean that the mechanisms of $c - \bar{c}$ creation included in the model are not sufficient to describe the observed open charm production.

The expected yield of charm quarks in the SMES model is much higher then the observed value. This might either mean that no QGP is formed or that it doesn't exist long enough to reach the equilibrium for the charm content. Thus the result suggests, that the

statistical model is not applicable to describe charm production at these energies. However, it is worth to note, that the interpretation of the experimental results on strangeness shows, that in case of strange quarks the equilibrium can be reached [20].

In the NA49 experiment the upper limit of the yield was estimated to be $M(D^0 + \overline{D^0})$ = 1.5 per event at 98% CL in Pb+Pb collisions at 158A GeV/c. For this analysis the mixture of two data set was used: 3M events with centrality 0–23.5% and 0.8M events with centrality 0–10%. These data can be recalculated to N_{part} = 272 and N_{coll} = 598, which corresponds to ≈0–20% centrality for Pb+Pb collisions. Thus, this result can be compared to the obtained in Chapter 7 result for 20% of the most central Pb+Pb collisions at 150A GeV/c. Both estimations of the upper limit discard the prediction made by SMES model, however the result obtained in this study provides much stronger restriction. This is due to improvement in the reconstruction accuracy provided by SAVD, which was not enough sufficient to observe the open charm signal in NA49. Anyhow, the obtained result shows consistency with the NA49 result.

Comparison of the obtained yields for Pb+Pb and Xe+La collisions open the possibility to estimate which scaling (according to $\langle N_{coll} \rangle$ or according to $\langle N_P \rangle$) shows a better performance.

Thus, assuming dynamical approach for scaling the Xe+La result assuming the AMPT phase space ($\langle N_{coll} \rangle$ = 331.1 for 20% of the most central Xe+La collisions, $\langle N_{coll} \rangle$ = 598.8 for 20% of the most central Pb+Pb collisions) the estimation for the $D^0 + \overline{D^0}$ yield for Pb+Pb would be 0.18. And assuming statistical approach for scaling ($\langle N_{part} \rangle$ = 173.7 for 20% of the most central Xe+La collisions, $\langle N_{part} \rangle$ = 272.5 for 20% of the most central Pb+Pb collisions) the yield for Pb+Pb is estimated to be 0.16. Since the both values are close one cannot conclude which scaling provides a better centrality dependence in description of the charm production. Furthermore, since the scaled Xe+La result is about factor 2 smaller then obtained result for Pb+Pb, it might suggest, that there is an additional enhancement present in the heavier system, though the accuracy obtained in the presented analysis does not allow to draw a strong conclusion.

9.2 Proposed open charm measurements after CERN Long Shutdown 2

Looking forward, the NA61/SHINE experiment will be upgraded during the CERN Long shutdown 2 from 2019–2021 to increase the data taking rate from 80 Hz to 1 kHz [12].

Within this task, the Vertex Detector will be also upgraded to provide a rate capability, which exceeds the one of SAVD by one order of magnitude. The related data rate is found to exceed the possibilities of the MIMOSA-26AHR sensors used so far in SAVD. Also, because of the increase of the expected radiation doses other sensors then the MIMOSA-26AHR had to be considered.

The upgraded VD will be based on the Monolithic Active Pixel sensors called ALICE PIxel DEtector (ALPIDE) developed for ALICE ITS [84, 62]. Using of the ALPIDE sensors will allow to reduce the read-out time to 10 μs, which fulfils the requirements for the NA61/SHINE upgrade.

In 2016 during test Pb+Pb at 150A GeV/c data taking one ITS Inner Barrel stave with 9 ALPIDE chips (the green vertical structure in Fig. 3.4), was installed for testing its

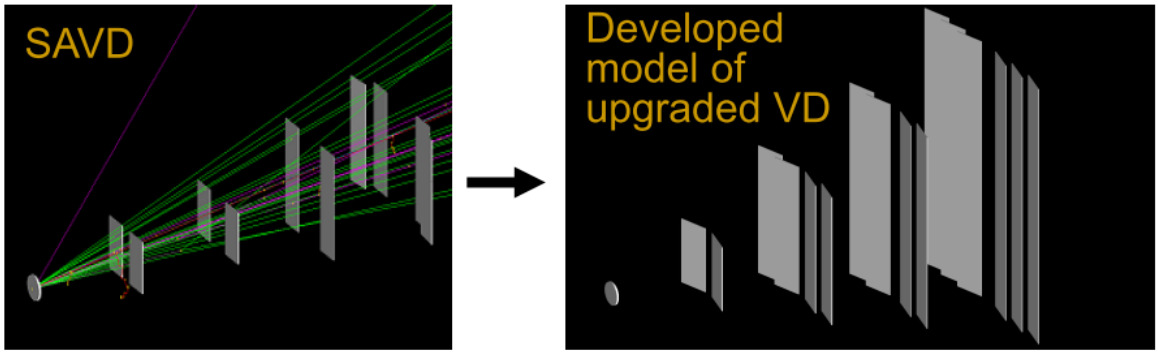

Figure 9.1: GEANT4 visualization of the current SAVD (left pad) and the proposed version of the upgraded Vertex Detector (right pad). Grey rectangles illustrate sensors, grey circles illustrate the target.

Year	Reaction	Events
2021	Pb + Pb 150A GeV/c	250M
2022	Pb + Pb 150A GeV/c	250M
2023	Pb + Pb 40A GeV/c	250M

Table 9.2: The NA61/SHINE data taking plan for the open charm measurements.

performance in the NA61/SHINE radiation environment [85]. Also, during 2018 Pb+Pb at 150A GeV/c ALPIDE sensor was put directly on the beam in SPS H4 beam line (parallel to SPS H2 beam line on which NA61/SHINE is located). These tests showed, that the ALPIDE sensors can successfully operate at the NA61/SHINE track density environment.

Also, as another advantage, the ALPIDE sensors can reach plateau of 100% detection efficiency keeping very low noise level ($\leq 10^{-6}$ versus $\leq 10^{-4}$ for MIMOSA-26AHR).

Furthermore, the upgraded VD will have larger acceptance for each station (see Figure 9.1). It is planned to increase number of sensors from 16 to 46 (also, size of the APLIDE sensor is slightly higher then of MIMOSA-26AHR: 13.8 $\times$ 30 cm^2 versus 10.6 $\times$ 21.2 cm^2).

The upgraded VD will use the most of the mechanics and infrastructure as was used in SAVD. It would be located inside He-filled enclosure. The sensors will be mounted on vertically oriented carbon fibre ladders, which are the same as those that will be used in the Inner Barrel of the new ALICE ITS. The location of stations would be similar as for SAVD: four stations positioned at about 5, 10, 15 and 20 cm from the target.

More details about the upgraded Vertex Detector could be found in [12].

The simulations performed using the AMPT event generator as input show that about 21% (AMPT phase space) or 17% (PHSD phase space) ($\approx$4 times better than for SAVD) of all $D^0 + \overline{D^0}$ in the π,K decay channel can be registered within the acceptance of the upgraded Vertex Detector. Figure 9.2 shows the generated $D^0 + \overline{D^0}$ and accepted by SAVD and by the upgraded VD (for the same generated events). Note, that it is an estimation of the acceptance since the geometry the upgraded VD will be a subject of the future optimization study. The total uncertainty of $\langle D^0 \rangle$ and $\langle \overline{D^0} \rangle$ is expected to be about 10% and is dominated by systematic uncertainty.

The data taking plan related to the open charm measurements in 2021–2023 is shown

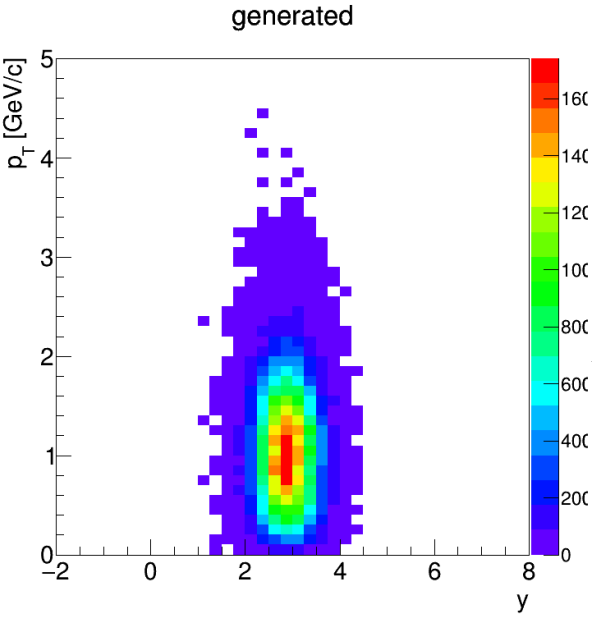

Figure 9.2: AMPT simulation of transverse momentum and rapidity distributions of $D^0 + \overline{D^0}$ mesons produced in central Pb + Pb collisions at $150A$ GeV/c corresponding to 1M events (according to the AMPT phase space). Upper pad: all generated $D^0 + \overline{D^0}$ mesons. Bottom pads: $D^0 + \overline{D^0}$ mesons in the π, K decay channel and both decay products registered by the upgraded VD and the TPCs and passing background suppression and quality cuts for SAVD (left pad) and for the upgraded VD (right pad).

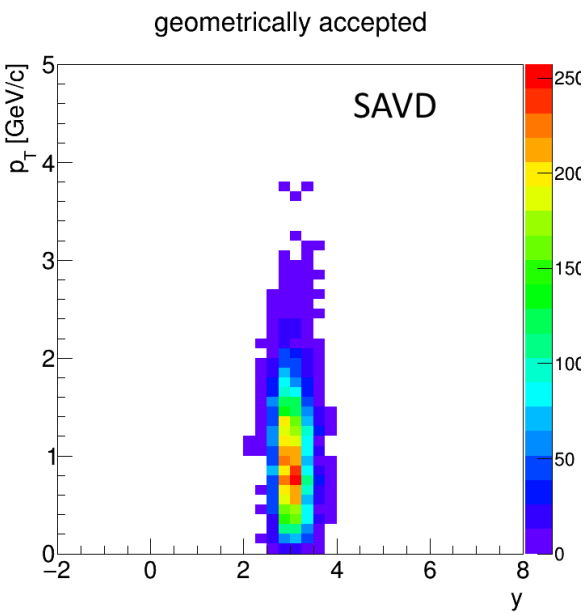

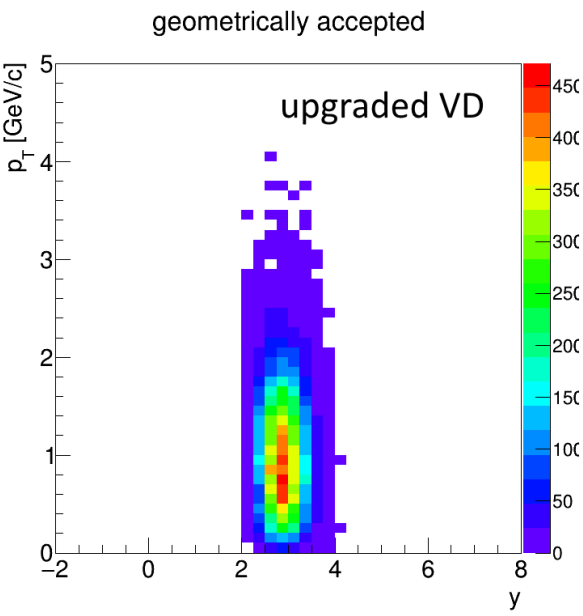

in Table 9.2. In total, 500M minimum bias Pb + Pb events are expected to be collected at the top SPS energy. The proposed program will allow to perform systematic studies of D^0, $\overline{D^0}$, D^+, and D^- production. This study will provide the total $c\bar{c}$ yield in central Pb+Pb collisions needed to investigate the mechanism of charm production. Moreover, the data will allow to establish the centrality dependence of $\langle c\bar{c} \rangle$ in Pb+Pb collisions at $150A$ GeV/c and thus address the question of how the formation of QGP impacts J/ψ production.

Chapter 10

Conclusion

The study of open charm meson production provides an efficient tool for detailed investigations of the properties of hot and dense matter formed in nucleus-nucleus collisions. In particular, charm mesons are of vivid interest in the context of the phase-transition between confined hadronic matter and the quark-gluon plasma as well as for interpretation of data on J/ψ production.

The first estimate of the upper limit of mean multiplicity of D^0 and $\overline{D^0}$ mesons by a direct measurement was done by the NA49 experiment in Pb+Pb collisions at the top SPS energies, i.e. 158A GeV/c corresponding to $\sqrt{s_{NN}}$ = 17.3 GeV for Pb+Pb. The NA38/NA50 and NA60 experiments measured precisely charmonia production at the top SPS energies via measurements of dimuon production. This study also allowed for an indirect estimate of open charm.

Recently, the experimental setup of the NA61/SHINE experiment was supplemented with a small-acceptance version of the Vertex Detector (SAVD) which was motivated by the importance and the possibility of the first direct measurements of open charm mesons in heavy ion collisions at SPS energies.

The main purpose of SAVD is the improvement of track resolution near the interaction point to allow reconstruction of secondary vertices which are located near the primary vertex. The developed track and vertex reconstruction algorithm (Chapter 4) for SAVD shows feasibility of very fine spatial resolution which was not possible before.

The NA61/SHINE physics data taking on open charm production in Xe+La and Pb+Pb collisions at 150A GeV/c was conducted in 2017 and 2018. These data were calibrated (Chapter 5) and 20% of most central events were selected for the analysis (Chapter 6).

The study of $D^0 + \overline{D^0}$ was done via their two-body decay channel $D^0 \to \pi^+ + K^-$ and $\overline{D^0} \to \pi^- + K^+$ (Chapter 7). The analysis showed the indication of $D^0 + \overline{D^0}$ signal, which allowed to estimate the yield for 0–20% central Xe+La collisions at 150A GeV/c:

$$N(D^0 + \overline{D^0})_{Xe+La,AMPT} = 0.10 \pm 0.03,$$
$$N(D^0 + \overline{D^0})_{Xe+La,PHSD} = 0.15 \pm 0.05,$$

and the yield for 0–20% central Pb+Pb collisions at 150A GeV/c:

$$N(D^0 + \overline{D^0})_{Pb+Pb,AMPT} = 0.33 \pm 0.18,$$
$$N(D^0 + \overline{D^0})_{Pb+Pb,PHSD} = 0.39 \pm 0.21.$$

Also, the upper limit of the total yield of $D^0 + \overline{D^0}$ at 98% CL was estimated to be

$$M(D^0 + \overline{D^0})_{AMPT,Xe+La} = 0.17,$$
$$M(D^0 + \overline{D^0})_{PHSD,Xe+La} = 0.25,$$

for 0–20% central Xe+La collisions at 150A GeV/c and

$$M(D^0 + \overline{D^0})_{AMPT,Pb+Pb} = 0.70,$$
$$M(D^0 + \overline{D^0})_{PHSD,Pb+Pb} = 0.82.$$

for 0–20% central Pb+Pb collisions at 150A GeV/c.

For obtaining the corrections and comparison with model predictions the simulation in GEANT4 was performed (Chapter 8): the background was described using the AMPT model and for parametrisation of the signal phase space the AMPT and the PHSD models were used. Note, that measurements of $D^0 + \overline{D^0}$ phase space are needed to remove model dependence of the derived yields.

The obtained results were compared with the yields obtained according to three predictions, namely: for the PHSD model predictions, for the NA50/NA60 estimations and for the SMES predictions. The PHSD predictions on $D^0 + \overline{D^0}$ yields are about factor 2-4 smaller as compare to the experimental result obtained in this work. Furthermore, comparison of the obtained yield with PHSD and NA50/NA60 shows good correspondence with the obtained yields for Xe+La and Pb+Pb collisions: the values overlap within the error bar. These two results might suggest that enhancement of open charm is necessary to describe the data results. Thus would mean that the mechanisms of $c - \bar{c}$ creation included in the model are not sufficient to describe the observed open charm production.

The obtained result on $D^0 + \overline{D^0}$ yield for Xe+La and Pb+Pb is not compatible with the SMES expectations. This could mean either, that no QGP was created or that the temperature and life-time of the QGP are such that the charm quark doesn't reach equilibrium.

The upper limit of the yield estimated by the NA49 $M(D^0 + \overline{D^0}) = 1.5$ per event at 98% CL in Pb+Pb collisions at 158A GeV/c shows consistency with the upper limit obtained within the performed study. Since the ability to background suppression in the NA61/SHINE was significantly improved as compared to the NA49, the obtained within this study result shows better precision.

Also, by comparing the obtained yield for Pb+Pb and Xe+La collisions one can estimate which scaling of the yield from one system to another shows better performance: by number of binary collisions $\langle N_{coll} \rangle$ (as predicted in dynamical approach) or by number of participants $\langle N_{part} \rangle$ (as predicted in statistical approach). However it was obtained, that both scaling provide values that are close, thus one cannot conclude which one provides a better consistency in description of the charm production versus the system size. Also, since the scaled Xe+La result is about factor 2 smaller then the obtained result for Pb+Pb, it might suggest, that there is additional enhancement present in the heavier system, though the accuracy obtained in the presented analysis does not allow to draw strong conclusion.

Furthermore, the NA61/SHINE experiment plans a systematic measurements of open charm production in Pb+Pb collisions in the period 2021-2024 after the major detector upgrade conducted during the Long Shutdown 2. These future data will allow for the more detailed research to establish the collision energy dependence of $\langle c\bar{c} \rangle$ at SPS energies and address the question of how the onset of deconfinement impacts charm production.

Bibliography

[1] S. Weinberg, Eur. Phys. J. C **34** (2004) 5 doi:10.1142/9789812567147_0005, 10.1140/epjc/s2004-01761-1 [hep-ph/0401010]. 13

[2] M. Tanabashi *et al.* [Particle Data Group], Phys. Rev. D **98** (2018) no.3, 030001. doi:10.1103/PhysRevD.98.030001 14

[3] Elementary particle - Wikipedia, *https://en.wikipedia.org/wiki/Elementary_particle* 14

[4] I. K. Yoo, "Bose-Einstein Correlations of Charged Kaons and Pions in Central Pb+Pb Collisions at 158 AGeV," PhD. thesis. 2001 15

[5] M. A. Stephanov, PoS LAT **2006** (2006) 024 doi:10.22323/1.032.0024 [hep-lat/0701002]. 15

[6] M. Stephanov, Acta Phys. Polon. B **35** (2004) 2939. 15

[7] F. Becattini, J. Manninen and M. Gazdzicki, Phys. Rev. C **73** (2006), 044905 doi:10.1103/PhysRevC.73.044905 [arXiv:hep-ph/0511092 [hep-ph]]. 15

[8] M. Gazdzicki, Eur. Phys. J. ST **155** (2008), 37-44 doi:10.1140/epjst/e2008-00587-0 [arXiv:0801.4919 [nucl-ex]]. 16

[9] M. Gazdzicki and C. Markert, Acta Phys. Polon. B **31** (2000) no.4, 965-983 [arXiv:hep-ph/9904441 [hep-ph]]. 18, 20, 108

[10] T. Matsui and H. Satz, Phys. Lett. B **178** (1986), 416-422 doi:10.1016/0370-2693(86)91404-8 18, 20, 22, 24

[11] M. Gazdzicki and M. I. Gorenstein, Phys. Rev. Lett. **83** (1999), 4009-4012 doi:10.1103/PhysRevLett.83.4009 [arXiv:hep-ph/9905515 [hep-ph]]. 18

[12] A. Aduszkiewicz *et al.*[NA61/SHINE Collaboration], Addendum (Proposal) 2018 CERN-SPSC-2018-008. SPSC-P-330-ADD-10. 18, 19, 21, 26, 110, 111

[13] P. Braun-Munzinger and J. Stachel, Phys. Lett. B **490** (2000), 196-202 doi:10.1016/S0370-2693(00)00991-6 [arXiv:nucl-th/0007059 [nucl-th]]. 18

[14] R. Gavai, S. Gupta, P. McGaughey, E. Quack, P. Ruuskanen, R. Vogt and X. Wang, Int. J. Mod. Phys. A **10** (1995), 2999-3042 doi:10.1142/S0217751X95001431 [arXiv:hep-ph/9411438 [hep-ph]]. 18

[15] T. Sjostrand, S. Mrenna and P. Z. Skands, JHEP **0605** (2006) 026 doi:10.1088/1126-

6708/2006/05/026 [hep-ph/0603175]. 18, 23

[16] O. Linnyk, E. Bratkovskaya and W. Cassing, Int. J. Mod. Phys. E **17** (2008), 1367-1439 doi:10.1142/S0218301308010507 [arXiv:0808.1504 [nucl-th]]. 18, 25

[17] P. Levai, T. Biro, P. Csizmadia, T. Csorgo and J. Zimanyi, J. Phys. G **27** (2001), 703-706 doi:10.1088/0954-3899/27/3/357 [arXiv:nucl-th/0011023 [nucl-th]]. 19

[18] M. Abreu *et al.* [NA50], Phys. Lett. B **477** (2000), 28-36 doi:10.1016/S0370-2693(00)00237-9 19

[19] A. Kostyuk, M. I. Gorenstein, H. Stoecker and W. Greiner, Phys. Lett. B **531** (2002), 195-202 doi:10.1016/S0370-2693(02)01488-0 [arXiv:hep-ph/0110269 [hep-ph]]. 19, 21

[20] M. Gazdzicki and M. I. Gorenstein, Acta Phys. Polon. B **30** (1999), 2705 [arXiv:hep-ph/9803462 [hep-ph]]. 19, 21, 108, 110

[21] W. Cassing and E. L. Bratkovskaya, Nucl. Phys. A **831** (2009) 215 doi:10.1016/j.nuclphysa.2009.09.007 [arXiv:0907.5331 [nucl-th]]. 20, 86, 87

[22] H. Satz, Adv. High Energy Phys. **2013** (2013) 242918 doi:10.1155/2013/242918 [arXiv:1303.3493 [hep-ph]]. 20, 22, 24, 25, 26

[23] B. Müller, Phys. Scripta T **158** (2013) 014004 doi:10.1088/0031-8949/2013/T158/014004 [arXiv:1309.7616 [nucl-th]]. 20

[24] R. V. Poberezhnyuk, M. Gazdzicki and M. I. Gorenstein, Acta Phys. Polon. B **48** (2017) 1461 doi:10.5506/APhysPolB.48.1461 [arXiv:1708.04491 [nucl-th]]. 21, 108

[25] C. Alt *et al.* [NA49 Collaboration], Phys. Rev. C **73** (2006) 034910 doi:10.1103/PhysRevC.73.034910 [nucl-ex/0507031]. 22

[26] M. Masera *et al.* [NA50 Collaboration], J. Phys. G **27** (2001) 677. doi:10.1088/0954-3899/27/3/353 22

[27] M. C. Abreu *et al.* [NA38 and NA50 Collaborations], Eur. Phys. J. C **14** (2000) 443. doi:10.1007/s100520000373 22

[28] R. Arnaldi *et al.* [NA60 Collaboration], Phys. Rev. Lett. **99** (2007) 132302. doi:10.1103/PhysRevLett.99.132302 22

[29] E. Scomparin *et al.* [NA50 Collaboration], J. Phys. G **25** (1999) 235. doi:10.1088/0954-3899/25/2/011 23

[30] R. Arnaldi *et al.* [NA60 Collaboration], Eur. Phys. J. C **59** (2009) 607 doi:10.1140/epjc/s10052-008-0857-2 [arXiv:0810.3204 [nucl-ex]]. 23

[31] U. W. Heinz and M. Jacob, nucl-th/0002042. 24

[32] A. N. Petridis, Phys. Rev. C **54** (1996) 848. doi:10.1103/PhysRevC.54.848 24

[33] E. Scomparin [NA60 Collaboration], Nucl. Phys. A **830** (2009) 239C doi:10.1016/j.nuclphysa.2009.10.020 [arXiv:0907.3682 [nucl-ex]]. 24

[34] L. Adamczyk *et al.* [STAR Collaboration], Phys. Rev. Lett. **113** (2014) no.14, 142301 Erratum: [Phys. Rev. Lett. **121** (2018) no.22, 229901] doi:10.1103/PhysRevLett.121.229901, 10.1103/PhysRevLett.113.142301 [arXiv:1404.6185 [nucl-ex], arXiv:1809.08737 [nucl-ex]]. 24, 25

[35] B. Abelev *et al.* [ALICE Collaboration], JHEP **1209** (2012) 112 doi:10.1007/JHEP09(2012)112 [arXiv:1203.2160 [nucl-ex]]. 24, 25, 26

[36] S. Chatrchyan *et al.* [CMS Collaboration], JHEP **1205** (2012) 063 doi:10.1007/JHEP05(2012)063 [arXiv:1201.5069 [nucl-ex]]. 24, 25, 26

[37] A. Adare *et al.* [PHENIX Collaboration], Phys. Rev. C **84** (2011) 044905 doi:10.1103/PhysRevC.84.044905 [arXiv:1005.1627 [nucl-ex]]. 24, 25

[38] B. Abelev *et al.* [ALICE Collaboration], Phys. Rev. Lett. **109** (2012) 072301 doi:10.1103/PhysRevLett.109.072301 [arXiv:1202.1383 [hep-ex]]. 25

[39] E. Meninno [ALICE Collaboration], EPJ Web Conf. **137** (2017) 06018. doi:10.1051/epjconf/201713706018 26

[40] G. W. S. Hou [ATLAS and CMS Collaborations], PoS CHARM **2016** (2016) 088. doi:10.22323/1.289.0088 26

[41] M. Simko [STAR Collaboration], J. Phys. Conf. Ser. **832** (2017) no.1, 012028. doi:10.1088/1742-6596/832/1/012028 26

[42] K. Nagashima [PHENIX Collaboration], Nucl. Phys. A **967** (2017) 644 doi:10.1016/j.nuclphysa.2017.06.038 [arXiv:1704.04731 [nucl-ex]]. 26

[43] G. Odyniec, J. Phys. Conf. Ser. **455** (2013) 012037. doi:10.1088/1742-6596/455/1/012037 26

[44] C. Yang [STAR Collaboration], Nucl. Phys. A **967** (2017) 800. doi:10.1016/j.nuclphysa.2017.05.042 26

[45] K. C. Meehan [STAR Collaboration], Nucl. Phys. A **956** (2016) 878. doi:10.1016/j.nuclphysa.2016.04.016 26

[46] S. Aoki *et al.* [DsTau Collaboration], JHEP **2001** (2020) 033 doi:10.1007/JHEP01(2020)033 [arXiv:1906.03487 [hep-ex]]. 26

[47] V. Kekelidze, A. Kovalenko, R. Lednicky, V. Matveev, I. Meshkov, A. Sorin and G. Trubnikov, Nucl. Phys. A **967** (2017) 884. doi:10.1016/j.nuclphysa.2017.06.031 26

[48] H. Sako *et al.* [J-PARC Heavy-Ion Collaboration], Nucl. Phys. A **956** (2016) 850. doi:10.1016/j.nuclphysa.2016.03.030 26

[49] B. Friman, C. Hohne, J. Knoll, S. Leupold, J. Randrup, R. Rapp and P. Senger, Lect. Notes Phys. **814** (2011) pp.1. doi:10.1007/978-3-642-13293-3 27

[50] M. Gazdzicki and P. Seyboth, Acta Phys. Polon. B **47** (2016) 1201 doi:10.5506/APhysPolB.47.1201 [arXiv:1506.08141 [nucl-ex]]. 27

[51] NA61/SHINE web-page, *http://shine.web.cern.ch/* 28

[52] N. Abgrall *et al.* [NA61], JINST **9** (2014), P06005 doi:10.1088/1748-0221/9/06/P06005 [arXiv:1401.4699 [physics.ins-det]]. 28, 29, 30

[53] Z. Fodor and S. Katz, JHEP **04** (2004), 050 doi:10.1088/1126-6708/2004/04/050 [arXiv:hep-lat/0402006 [hep-lat]]. 28

[54] N. Abgrall [NA61 and T2K], [arXiv:1005.3692 [hep-ex]]. 28

[55] S. Johnson, Technical Report 2014 CERN-SPSC-2014-032. SPSC-P-330-ADD-7. 28

[56] N. Antoniou *et al.* [NA49-future], CERN-SPSC-2006-034. 29

[57] A. Aduszkiewicz *et al.*[NA61/SHINE Collaboration], Addendum (Proposal) 2015 CERN-SPSC-2015-038. SPSC-P-330-ADD-8. 33

[58] Y. Ali, P. Staszel, A. Marcinek, J. Brzychczyk and R. Planeta, Acta Phys. Polon. B **44** (2013) no.10, 2019. doi:10.5506/APhysPolB.44.2019 33

[59] Y. Ali *et al.* [NA61/SHINE Collaboration], J. Phys. Conf. Ser. **509** (2014) 012083. doi:10.1088/1742-6596/509/1/012083 33

[60] M. Deveaux *et al.*, JINST **6** (2011) C02004. doi:10.1088/1748-0221/6/02/C02004 33

[61] M. Koziel, S. Amar-Youcef, N. Bialas, M. Deveaux, I. Fröhlich, Q. Li, J. Michel, B. Milanović, C. Müntz and B. Neumann, *et al.* Nucl. Instrum. Meth. A **732** (2013), 515-518 doi:10.1016/j.nima.2013.07.041. 33

[62] B. Abelev *et al.* [ALICE Collaboration], J. Phys. G **41** (2014) 087002. doi:10.1088/0954-3899/41/8/087002 33, 110

[63] P. Klaus *et al.*, JINST **11** (2016) no.03, C03046. doi:10.1088/1748-0221/11/03/C03046 34

[64] A. Neiser, J. Adamczewski-Musch, M. Hoek, W. Koenig, G. Korcyl, S. Linev, L. Maier, J. Michel, M. Palka, M. Penschuck, M. Traxler, C. Uğur and A. Zink, JINST **8** (2013), C12043 doi:10.1088/1748-0221/8/12/C12043 34

[65] S. Afanasiev *et al.* [NA49], Nucl. Instrum. Meth. A **430** (1999), 210-244 doi:10.1016/S0168-9002(99)00239-9 37, 38

[66] P. V. C. Hough, Conf. Proc. C **590914** (1959), 554-558 45

[67] P. Kövesárki, A. László [NA61/SHINE Collaboration], "Calibration Chain with Shine Offline Framework," https://twiki.cern.ch/twiki/pub/NA61/TpcDvCalibrationInstructions/20149424_Calibration_cl 53, 54

[68] A. Aduszkiewicz *et al.*[NA61/SHINE Collaboration], Status Report 2017 CERN-SPSC-2017-038. SPSC-SR-221. 57

[69] W. Brylinski, Master Thesis, CERN-THESIS-2018-110, 2018 57

[70] F. James and M. Winkler, "MINUIT User's Guide' 57

[71] D. S. Sivia, "Data Analysis – a Bayesian Tutorial", Oxford University Press, Oxford, (1997) 80

[72] T. Anticic *et al.* [NA49], Phys. Rev. C **80** (2009), 034906 doi:10.1103/PhysRevC.80.034906 [arXiv:0906.0469 [nucl-ex]]. 81

[73] R. Brun, F. Bruyant, F. Carminati, S. Giani, M. Maire, A. McPherson, G. Patrick and L. Urban, doi:10.17181/CERN.MUHF.DMJ1 83

[74] Z. W. Lin, C. M. Ko, B. A. Li, B. Zhang and S. Pal, Phys. Rev. C **72** (2005), 064901 doi:10.1103/PhysRevC.72.064901 [arXiv:nucl-th/0411110 [nucl-th]]. 85

[75] Z. W. Lin, Phys. Rev. C **90** (2014) no.1, 014904 doi:10.1103/PhysRevC.90.014904 85

[76] B. Zhang, C. Ko, B. A. Li and Z. W. Lin, Phys. Rev. C **61** (2000), 067901 doi:10.1103/PhysRevC.61.067901 [arXiv:nucl-th/9907017 [nucl-th]]. 85

[77] X. N. Wang and M. Gyulassy, Phys. Rev. D **44** (1991), 3501-3516 doi:10.1103/PhysRevD.44.3501 85

[78] B. Zhang, Comput. Phys. Commun. **109** (1998), 193-206 doi:10.1016/S0010-4655(98)00010-1 [arXiv:nucl-th/9709009 [nucl-th]]. 85

[79] B. Andersson, G. Gustafson, G. Ingelman and T. Sjostrand, Phys. Rept. **97** (1983), 31-145 doi:10.1016/0370-1573(83)90080-7 85

[80] B. Andersson, G. Gustafson and B. Soderberg, Z. Phys. C **20** (1983), 317 doi:10.1007/BF01407824 85

[81] B. Li, A. Sustich, B. Zhang and C. Ko, Int. J. Mod. Phys. E **10** (2001), 267-352 doi:10.1142/S0218301301000575 85

[82] S. Afanasiev *et al.* [NA49], Phys. Rev. C **66** (2002), 054902 doi:10.1103/PhysRevC.66.054902 [arXiv:nucl-ex/0205002 [nucl-ex]]. 85

[83] M. Aguilar-Benitez *et al.* [LEBC-EHS], Z. Phys. C **40** (1988), 321 doi:10.1007/BF01548848 108

[84] G. Aglieri, C. Cavicchioli, P. L. Chalmet, N. Chanlek, A. Collu, P. Giubilato, H. Hillemanns, A. Junique, M. Keil and D. Kim, *et al.* JINST **8** (2013), C12041 doi:10.1088/1748-0221/8/12/C12041 110

[85] M. Suljic, PhD Thesis, CERN-THESIS-2017-304, 2017 111